



FAKULTÄT FÜR MASCHINENWESEN  
LEHRSTUHL FÜR FLUIDMECHANIK

NUMERICAL SIMULATION, DESIGN AND OPTIMIZATION OF A RADIAL-  
INFLOW TURBINE FOR ENERGY RECOVERY USAGE OF AUTOMOBILES

Usama Merry Salih Aljanaby

Vollständiger Abdruck der von der Fakultät für Maschinenwesen der Technischen  
Universität München zur Erlangung des akademischen Grades eines

Doktor-Ingenieurs

genehmigten Dissertation.

Vorsitzender: Univ.-Prof. Dr.-Ing. M. Hajek.

Prüfer der Dissertation:

1. Univ.-Prof. Dr.-Ing. Dr.-Ing. habil. Dr. h.c. R. Schilling (i.R.)
2. Univ.-Prof. Dr.-Ing. Th. Sattelmayer

Die Dissertation wurde am 07.07.2015 bei der Technischen Universität München  
eingereicht und durch die Fakultät für Maschinenwesen am 03.11.2015 angenommen

# Acknowledgement

The introduced work is a result of my research during the four years as a scholarship holder at the institute of Fluid Mechanics (FLM) at the Technische Universität München (TUM), under the supervision of Prof. Dr. -Ing. R. Schilling. Therefore, I would like to express my gratefulness to the Deutscher Akademischer Austausch Dienst (DAAD) and the Iraqi MoHESR who granted me the scholarship in 2010.

I would like to sincerely thank Prof. Dr. -Ing. R. Schilling who gave me the opportunity to conduct my research at the institute of Fluid Mechanics at the TUM. His highly scientific competence, technical expertise, the remarkable ideas and his continuous support in my ups and downs, have helped me the most in achieving this work and giving it more valuable records. The pleasant atmosphere he provided the institute with, and the friendly discussions we have had throughout this period are unique and that was the key of the success in the institute on both the personal and the academic levels. I would like also to express my gratitude to my colleague and former office-mate Dr.-Ing. Susanne Thum for her constructive support.

Sincerely thanks and appreciations to the examiners, Prof. Dr.-Ing. Manfred Hajek who conducted the examination, as wells Prof. Dr.-Ing. Thomas Sattelmayer who took part in the evaluation of my thesis with a valuable remarks. My thanks also to the technical and the administrative staff at the TUM, who were always there to support.

To my colleagues in the group and in the institute with whom I was always sharing the scientific and the academic ideas, especially for Dr.-Ing. Andreas Gantner, Dipl. -Ing. Josef Kiermeir and Dipl. -Ing. Andreas Rosenberger, they all were always ready for support.

To the soul of my father, who gave me an overwhelming encouragement and an invaluable support until he passed away. To my mom, who devoted her whole life to support me throughout the long years, to my brothers and sister, the deepest sense of gratitude and thanks.

To my wife Zahraa with love, who was my companion and partner in everything worthwhile, to my little angel Lana who joined us lately, I dedicate this work.

Printed by DAAD.

# Table of Contents

<b>Table of Contents .....</b>	<b>I</b>
<b>Table of Figures.....</b>	<b>V</b>
<b>List of Tables.....</b>	<b>IX</b>
<b>Abbreviations.....</b>	<b>IX</b>
<b>Abstract .....</b>	<b>XVI</b>
<b>1 Introduction.....</b>	<b>1</b>
1.1 The Resources of the Waste Heat Energy in Automobiles.....	3
1.2 Design approach .....	7
1.3 Thesis Structure .....	8
<b>2 Theory of Fluid Dynamics.....</b>	<b>11</b>
2.1 Turbulent Flow Modelling.....	14
2.2 Eddy Viscosity models .....	20
2.3 Two-Equation models.....	21
2.3.1 The $K$ - $\omega$ Model.....	23
2.3.2 The $K$ - $\epsilon$ Model.....	21
2.4 The SST $K$ - $\omega$ Model .....	25
2.5 Wall Treatments.....	27
2.6 Effects of Compressibility .....	29
2.7 Favre Averaging .....	30
2.8 Favre Average Equations.....	32
2.9 $K$ - $\omega$ Model for Compressible Flows.....	37
2.10 Compressible boundary layers.....	38
2.10.1 Shock-Induced Boundary-Layer Separation .....	40
2.10.2 The Use of Wall Function for Shock-Separated Flow .....	41
<b>3 Finite Volume Method (FVM) for CFD.....</b>	<b>43</b>
3.1 Introduction.....	43

3.2	FVM for diffusion problem .....	44
3.3	FVM for Convection Problem .....	46
3.4	Properties of discretization schemes.....	48
3.4.1	Conservativeness .....	48
3.4.2	Boundedness.....	48
3.4.3	Transportiveness.....	49
3.5	The upwind differencing scheme.....	50
3.6	The Hybrid differencing .....	51
3.7	Discretization of Instationary Term .....	51
3.8	Boundary Conditions .....	52
3.8.1	Inlet and Outlet Boundary Conditions.....	53
3.8.2	Block Interface .....	54
3.8.3	Wall Boundary Conditions .....	55
3.8.4	Free Slip .....	57
3.8.5	Periodic Interface .....	57
3.9	The Pressure-Velocity Coupling.....	57
3.10	Solver.....	58
3.10.1	The Segregated Solver and the Implicit Pressure Correction.....	58
3.10.2	Coupled Solver .....	59
3.10.3	Linear Solver .....	59
<b>4</b>	<b>Turbines Concepts and Configuration .....</b>	<b>62</b>
4.1	Introduction.....	62
4.2	Aerodynamic design strategy .....	63
4.2.1	The flow and load coefficients .....	67
4.2.2	Aerodynamic Considerations of the Rotor Exit .....	68
4.2.3	The Optimum Incidence Angle and the Blade Number .....	71
4.3	Turbine Geometry.....	73
4.3.1	Radial-Inflow Turbine Rotor Sizing.....	73
4.3.2	Radial-Inflow Turbine Design Specifications .....	74

4.3.3	Rotor Design Evaluating .....	78
4.3.4	Rotor End-Wall Contours.....	79
4.3.5	Straight Line Element Rotor Blade Camberline.....	81
4.3.6	Radial Element Rotor Blade Camberline .....	83
4.3.7	The Equation of State of Real Gases .....	84
4.4	Inviscid Solution Method .....	86
4.5	Viscous Solution Method .....	87
4.6	Coupled Viscous-Inviscid Methods.....	87
4.7	Nozzle Row Analysis and Sizing .....	88
4.8	Operating Points Estimation .....	91
<b>5</b>	<b>Simulation of Radial Inflow turbine .....</b>	<b>93</b>
5.1	Turbine preliminary design.....	94
5.2	Mesh Independence Analysis .....	96
5.3	Validation of the results.....	102
5.4	The Turbulence Models Effect .....	103
5.5	Inlet boundary and off-design conditions effect.....	105
5.6	Blade Number Effect .....	113
5.6.1	Rotor Inlet Width Estimation .....	115
5.6.2	The Vane Solidity in the Radial Inflow Turbine Stator .....	119
5.7	Estimating the Interspace Distance.....	122
<b>6</b>	<b>Optimization a Radial Inflow Turbine .....</b>	<b>125</b>
6.1	Design of Experiments DOE method .....	126
6.1.1	Response Surface .....	128
6.1.2	The Artificial Neural Network .....	132
6.1.3	Parameter Local and Global Sensitivity .....	133
6.2	Genetic algorithm optimization .....	135
6.3	Optimization methods results .....	135
<b>7</b>	<b>Conclusions .....</b>	<b>138</b>
7.1	Outlook .....	139

<b>8</b>	<b>Appendix A</b> .....	<b>141</b>
	8.1 Minimum inlet Mach number .....	141
<b>9</b>	<b>Bibliography</b> .....	<b>146</b>

# Table of Figures

Figure 1.1 Production of vehicles from 2005 to 2010 for selected countries, [87].	2
Figure 1.2: Recent achievements in peak indicated thermal efficiency in diesel engines, [28].	4
Figure 1.3 The heat recovery cycle, [98].	5
Figure 1.4 A schematic of radial inflow components.	7
Figure 2.1 Typical point velocity measurement in a turbulent flow, velocity versus time, [65].	15
Figure 2.2: Typical velocity profile $u^+(y^+)$ at the turbulent boundary layer, [106].	28
Figure 2.3: Computed and measured Pitot-pressure profile for Mach 3 shock-wave/ boundary- layer interaction, [106].	40
Figure 3.1 Three dimensional cell and neighboring nodes.	45
Figure 3.2 Distribution of $\phi$ in the vicinity of two sources at different Peclet numbers, [65].	49
Figure 4.1: The station notations of the stage.	63
Figure 4.2: Balje Diagram for radial inflow turbines, [32].	64
Figure 4.3: Balje diagram for a radial inflow turbines, [32].	65
Figure 4.4: Distribution of losses along envelope of total to static efficiency, [85].	66
Figure 4.5: Correlation of measured efficiency of a range of turbine designs with stage loading and flow coefficients, [11].	68
Figure 4.6: Relative Mach number $M_{5R}$ as a function of Mach number $M_5$ , with $\Phi_f$ as a parameter. The pressure ratio is $p_{o1}/p_5 = 2$ , with $\eta_{ts} = 0.85$ and $\gamma = 1.4$ , [57]	70
Figure 4.7: Blade width-to-radius ratio as a function of the relative velocity ratio $W_{5s}/W_4$ for relative flow angles corresponding to minimum Mach number at the inlet and at axial exit. The pressure ratio is $p_{o5}/p_5 = 2$ , with $\eta_{ts} = 0.85$ , $\gamma = 1.4$ , and the static enthalpy loss coefficient of the stator is $\zeta_s = 0.15$ . The exit hub to shroud radius ratio is $k = 0.2$ , [57].	72
Figure 4.8: A typical hub contour as Aungier suggested.	79
Figure 4.9: Typical Rotor Geometry Distributions, $Aria/Aria_{max.}$ , Rotor inlet width $b/$ Rotor inlet width $b_{max.}$ and the Rotor inlet width $b/$ Chord radius, [15].	80



Figure 4.10: Straight-Line Elements Blade Angles, [15].	83
Figure 4.11: Radial-Elements Blade Angle Distribution, [15].	84
Figure 4.12: Ethanol T-S diagram.	91
Figure 5.1: Stage loading coefficients for radial turbines with radial section blades versus flow coefficient and the data points show the total to static efficiency, [12]	94
Figure 5.2: Balje diagram for the radial inflow turbine, [32].	95
Figure 5.3: Mesh of the nozzle passage.	96
Figure 5.4: The mesh of the rotor blades at the hub.	97
Figure 5.5: Control volume with one nozzle passage.	97
Figure 5.6: The mesh of the rotor blade.	98
Figure 5.7: Mesh independence analysis.	98
Figure 5.8: Total pressure at monitoring point 4.	99
Figure 5.9: Mach number at monitoring point 4.	100
Figure 5.10: Total enthalpy at monitoring point 4.	100
Figure 5.11: Total temperature at monitoring point 4.	101
Figure 5.12: The effect of using k- $\epsilon$ and SST k- $\omega$ turbulence models on the pressure prediction.	104
Figure 5.13: The effect of the total inlet temperature on the total to static efficiency $\eta_{t-s}$ at different rotational speeds N.	105
Figure 5.14: The effect of the total inlet temperature on the shaft power $P_{sh}$ at different rotational speeds N.	105
Figure 5.15: The effect of the total inlet temperature on the isentropic enthalpy drop at different rotational speeds N.	106
Figure 5.16: The effect of the total inlet temperature on the total to reaction at different rotational speeds N.	107
Figure 5.17: The effect of the total inlet temperature on the specific speed $N_s$ at different rotational speed N.	107
Figure 5.18: The effect of the total inlet temperature on the specific diameter $D_s$ at different rotational speed N.	108
Figure 5.19: The effect of the total inlet temperature on the load coefficient at different rotational speed N.	108

Figure 5.20: The effect of the total inlet temperature on the flow coefficient $\psi$ at different rotational speed $N$ .....	109
Figure 5.21: The effect of the total inlet temperature on rotor exit flow angle $\alpha_5$ at different rotational speed $N$ .....	110
Figure 5.22: The effect of the total inlet temperature on rotor exit relative flow angle $\beta_5$ at different rotational speeds $N$ . ....	111
Figure 5.23: The effect of the total inlet temperature on rotor inlet relative flow angle $\beta_4$ at different rotational speed $N$ .....	111
Figure 5.24: The effect of the total inlet temperature on the velocity ratio $v$ at different rotational speeds $N$ . ....	112
Figure 5.25: The blade loading, Static pressure $P$ for different numbers of rotor blade at 50% span. ....	113
Figure 5.26: The blade loading, Static pressure $P$ for different numbers of rotor blade at 75% span. ....	114
Figure 5.27: The blade loading, Static pressure $P$ for different numbers of rotor blade at 25% span. ....	114
Figure 5.28: Relative Mach number $M_{rel}$ . at the rotor trailing edge vs. normalized span length.....	115
Figure 5.29: Relative Mach number $M_{rel}$ . at the rotor leading edge vs. normalized span length.....	115
Figure 5.30: Absolute Mach number $M_{rel}$ . at the rotor trailing edge vs. normalized span length.....	116
Figure 5.31: Relative flow angle at the rotor trailing edge vs. normalized span length. ....	116
Figure 5.32: Effect of the relative inlet width on the relative total to static efficiency. ....	117
Figure 5.33: Absolute flow angle at the rotor trailing edge vs the normalized blade span length.....	117
Figure 5.34: Static pressure $P$ versus normalized meridional length for different span positions with relative blade width $d/D_4$ as parameter.....	118
Figure 5.35: The effect of the number of nozzle blades on the nozzle loss coefficient, $\lambda_N$ .....	119
Figure 5.36: Iso-colour plots of the pressure distribution at 50% span for different number of nozzle blades.....	120

Figure 5.37: Relative Mach number $M_{rel}$ at the rotor leading edge (LE) for different numbers of nozzle blades. ....	121
Figure 5.38: Relative Mach number $M_{rel}$ at the rotor trailing edge (TE) for a different numbers of nozzle lades. ....	121
Figure 5.39: Absolute Mach number $M_{abs}$ at the rotor leading edge LE for a different numbers of nozzle blades. ....	122
Figure 5.40: Normalized total pressure losses $\Delta P_t/P_{t3}$ versus the radius ratio of the nozzle trailing edge radius $r_3$ and the ratio inlet radius $r_4$ . ....	123
Figure 5.41: Ratio of the absolute Mach number of the nozzle outlet $M_{abs 3}$ and the absolute Mach number at the rotor inlet $M_{abs 4}$ versus the radius ration $r_3/r_4$ . ....	124
Figure 6.1: Parameters parallel chart. ....	127
Figure 6.2: Goodness of Fit predicted from the Response Surface versus the goodness observed from the design points. ....	128
Figure 6.3: 3D response chart for the $\eta_{t-s}$ vs. the total inlet pressure and temperature and $\omega$ . Also $\eta_{t-s}$ vs. total inlet pressure and temperature. ....	129
Figure 6.4: 2D response surface of the $\eta_{t-s}$ vs. $\omega$ . ....	130
Figure 6.5: 2D response surface of the $\eta_{t-s}$ vs $P_{t in}$ , with the DOE points. ....	130
Figure 6.6: The Response Surface of the total-to-static efficiency $\eta_{t-s}$ versus the $P_{t in}$ for different algorithm types. ....	131
Figure 6.7: Response Surface of the $\eta_{t-s}$ to the $P_{t in}$ by different algorithm types (The –ve sign refers to the direction of the rotation). ....	131
Figure 6.8: A schematic graph of the ANN. ....	132
Figure 6.9: Local sensitivity of Parameters. ....	133
Figure 6.10: Global sensitivity depending on output parameters ....	134
Figure 6.11: Cadidate design points ....	134
Figure 6.12: Relative Mach number $M_{5re}$ at the rotor trailing edge TE versus the normalized span width for the optimization candidate points. ....	136
Figure 6.13: Absolute Mach number $M_{5re}$ at the rotor trailing edge TE versus the normalized span width for the optimization candidate points. ....	136

# List of Tables

Table 1.1: Terminal energy consumption structure by region and sector. ....	3
Table 4.1: The Recommended Range of the Optimum Design Parameters. ....	78
Table 5.1: Summery of the mesh-independence work-through.....	101
Table 5.2: Comparison of the mean-line analysis and the 3D-CFD simulation. ....	103
Table 6.1: sample of the design Points in the Design of Experiments .....	126
Table 6.2: The keys of the parameters used in the DX optimization.....	127
Table 6.3: Percentage of the recovered energy .....	135

# Abbreviations

BCGSTAB	Bi-conjugate gradient stabilized method
BSL	Baseline
BMEP	Break Mean Effective Pressure
CAD	Computer aided design
CDS	Central difference scheme
CFD	Computational Fluid dynamics
DES	Detached eddy simulation
DNS	Direct numerical simulation
FEA	Finite element analysis
FEM	Finite element method
FLM	Lehrstuhl für Fluidmechanik (Institute of Fluid Mechanics)
FVM	Finite volume method
HOS	Higher order scheme
IMEP	Indicated Mean Effective Pressure
LE	Leading edge
LES	Large eddy simulation
LTC	Low Temperature Combustion

PCCI	Partially Premixed Compression Ignition
d-f PCCI	Dual-fuel Partially Premixed Compression Ignition
PS	Pressure side
QUICK	Quadratic upwind interpolation
RANS	Reynolds-averaged Navier-Stokes equations
RSM	Reynolds stress model
SIMPLE	Semi implicit method for pressure linked equations
SS	Suction side
SST	Shear stress transport
SSF	Specific Fuel Consumption
TE	Trailing edge
TUM	Technische Universität München
UDS	Upwind difference scheme
URANS	Unsteady Reynolds-Averaged Navier-Stokes equations
WF	Wall function
WR	The exit to the inlet relative flow velocity ration

### **Software**

ANSYS	Ansys Inc., ANSYS-Workbench Release 14.5
CATIA	Dassault Syst_emes, CATIA V5
CFX	Ansys Inc., ANSYS-CFX Release 14.5
DX	Ansys Inc., Design Exploration Release 14.5
ICEM	Ansys Inc., ICEM-CFD Release 14.5
Matlab	Mathworks Inc., Release Matlab R2014a

### **Dimensionless Numbers**

CFL	Courant number
M	Mach Number
Pe	Peclet Number
Re	Reynolds number
Pr	Prandtl number

**Latin Letters**

A	Area; Turbulence model constant; Coefficient matrix
B	Fluid bulk modulus
BF	Blend function multiplier
C	Wall law constant; Turbulence model constant; Constraint;
$C_p$	Heat capacity at constant pressure; Pressure coefficient
$C_v$	Heat capacity at constant volume
D	Diameter
$D_1$	Turbine inlet diameter
$D_2$	Nozzle inlet diameter
$D_3$	Nozzle exit diameter
$D_4$	Rotor inlet diameter
$D_5$	Rotor exit mean diameter
$D_{5h}$	Rotor exit hub diameter
$D_{5s}$	Rotor exit shroud diameter
$D_{k\omega}$	Turbulence model constant
F	Flux; Blend function; Force
$F_1$	SST $\gamma$ -SST blend function
$F_2$	SST second blend function
$F_{ext}$	External loads
$F_{sst}$	Chosen SST blend function
K	Constant
$L_{char}$	Characteristic length
$L_T$	Turbulence length scale
$L_{vk}$	Von Karman length scale
M	Moment
N	Number of steps
P	Power
$P_k$	Specific turbulent kinetic energy production term
Q	Volume flow; Source flux
R	Radius; Reference Radius; Gas law constant
$R_{inner}$	Inner iterations residuum
$R_{oute}$	Outer iterations residuum
Re	Reynolds number

$Re_T$	Turbulence Reynolds number
$S_{ij}$	Fluid strain tensor
$T$	Torque; Period; Temperature
$T_{ij}$	Transformation matrix
$T_T$	Turbulence time scale
$Tu$	Turbulence intensity
$U$	Peripheral velocity; Potential energy
$V$	Volume
$W$	Work
$a$	Sound velocity
$arg$	Turbulence model constant
$b$	Rotor inlet width; Nodes
$C$	Absolute velocity; Turbulence model constant
$C_m$	Absolute velocity meridional component
$C_u$	Absolute velocity tangential component
$e$	Specific internal energy
$e_t$	Specific total internal energy
$f$	Frequency; Turbulence model constant
$g$	Gravity acceleration
$h$	Specific enthalpy
$H$	Specific total enthalpy
$i$	First index direction
$j$	second index direction
$k$	Specific turbulent kinetic energy; Third index direction
$\ell$	Conformal length coordinate
$\ell_{mix}$	Mixing length
$m$	Mass, Meridional coordinate
$\dot{m}$	Mass flow rate
$n$	Normal direction; Rotation speed
$n_s$	Turbine specific speed
$P$	Pressure
$P_t$	Total pressure
$q$	Heat transfer rate
$r$	Radius; radial coordinate

$r_1$	Turbine inlet radius
$r_2$	Nozzle inlet radius
$r_3$	Nozzle exit radius
$r_4$	Rotor inlet radius
$r_5$	Rotor exit mean radius
$r_{5h}$	Rotor exit hub radius
$r_{5s}$	Rotor exit shroud radius
$t$	Time; Tangential direction;
$t_{ij}$	Viscous stress
$u$	Velocity component.
$u^+$	Dimensionless sublayer-scaled velocity
$V$	Velocity component
$w$	Velocity component
$x$	x coordinate
$y$	y coordinate; wall displacement
$y_2$	Distance from the first cell center to the wall boundary
$y^+$	Dimensionless sublayer-scaled distance
$z$	z coordinate; Axial coordinate; number of blades
$C$	Damping matrix

### Greek Letters

$\Gamma$	Diffusive coefficient
$\Delta H_{id}$	Ideal enthalpy drop
$\Delta p$	Pressure drop
$\Delta \eta$	Efficiency difference
$\phi$	General variable in Reynolds and Favre decompositions; Length scale
$\Omega$	Vorticity; Rotation frequency; Angular velocity
$\Omega_{ij}$	Rotation tensor
$\alpha$	Flow angle
$\beta$	Relative flow angle
$\nu$	Velocity ratio; Kinematic viscosity
$\rho$	fluid density
$\varphi$	Flow coefficient



$\psi$	load coefficient
$\gamma$	Heat capacity ratio
$\delta_i$	Flow incidence angle
$\delta_d$	Flow deviation angle
$\epsilon$	Dissipation rate
$\zeta$	model constant; Damping factor
$\eta$	Efficiency
$\theta$	Angle; Angle coordinate
$k$	Von Karman constant
$\mu$	Dynamic viscosity
$\sigma$	Turbulence model constant
$\tau$	Viscous normal stress; Shear stress
$\tau_{ij}$	Specific Reynolds stress tensor
$\chi$	Conformal tangential coordinate
$\omega$	Turbulence dissipation frequency; Angular velocity

### Subscripts

0	Reference value; Initial condition
1	Turbine inlet station
2	Nozzle inlet station
3	Nozzle outlet station
4	Rotor inlet station
5	Rotor exit station
abs	Absolute
h	Hub
r	Relative flow
rel	Relative
rot	Rotational
SST	Shear stress transport
t	Total condition
T	Turbulence
char	Characteristics
i	Index

j	Index
k	Index
m	Meridional plane
max	Maximum
min	Minimum
n	Normal component; Rotation speed
opt	Optimum
out	Outlet boundary conditions
ref	Reference
s	Entropy
t	Tangential; total
turb	Turbulence
x	x component
y	y component
z	z component
$\epsilon$	Dissipation rate
$\mu$	Viscous
$\rho$	Density
$\tau$	Shear stress
$\phi$	General variable
$\omega$	Turbulence dissipation frequency

### Superscripts

+	Dimensionless sublayer-scaled
*	Alternative variable; Dimensionless value
'	Oscillatory value in Reynolds decomposition
"	Oscillatory value in Favre decomposition
CDS	Central difference scheme
UDP	Upwind difference scheme
n	Iteration

### Overhead Symbols

-	Reynolds-average, i.e. time-average; Area-average
∨	Favre-average, i.e. mass-average

# Abstract

With the continuous global energy shortage and the climate change awareness, recovering the wasted energy in the automobiles is an inevitable task. However, the limitation in the size of automobile's engine requires that any additional part should be as small as possible and produce as significantly high power as possible, i.e. as high power density as possible.

The work in this thesis introduces a design procedures to achieve a complete numerical simulation and performance optimization for a radial inflow turbine which is used in the energy recovery of the automobiles. The geometry is first created for the design point making use of dimensionless parameters, such as specific speed, specific diameter, loading coefficient, flow coefficient, Mach number and other empirical correlations.

Out of many working fluids, we chose the organic fluid Ethanol  $C_2H_5OH$  to be our working fluid as it has remarkable properties that fit the requirements of the application, and it is also appropriate to be used in the turbine operating conditions, such as, it has a low boiling temperature and low critical point.

The numerical simulation has been performed to the radial inflow turbine using a finite volume FV model based, which makes use of highly sophisticated turbulence models such as *SST  $K-\omega$*  and  *$k-\epsilon$* . An appropriate turbulence modelling is a very sensitive issue to the turbomachinery design, especially when we have flow transitions and discontinuities such as shock waves.

The effect of the various boundary conditions especially the inlet thermodynamic properties and the rotational speed are shown. The impact of the variation of these boundary conditions on the produced power and the total to static efficiency are also intensively investigated. The geometrical effect also has been thoroughly analyzed, such as, the effect of the vaneless space between the nozzle trailing edge and the rotor leading edge on the total turbine performance is assessed. The effect of the number of rotor blades and the nozzle vanes on the performance has been calculated as well

The numerical optimization for the design using Multi-Objective Genetic Algorithm MOGA is performed. The response surface of the input and output parameters has been also created using the Artificial Neural Network ANN and also other embedded techniques such Kriging and Non-Parametric Regression. The design points have been calculated using the design of experiments DOE. The sensitivity of each output parameter to the input parameters has been also shown, which makes us have a clear vision about

how the parameters react to each other. From the Global Optimization, design points candidates are produced, which should achieve the optimum performance for the design.

The simulation of the candidate points of the optimization process as operating conditions of the turbine have been performed and the results have shown an additional improvement of the turbine performance. The amount of the recovered energy in the case study we took, is significant enough to apply this method in the automobile industry field as it can cutoff a reasonable amount of fuel and hence, a good impact on both the environment and the specific fuel consumption SFC i.e. economic impact.

# 1 Introduction

The limited amount of the fossil fuel, which is the main energy source around the globe, means that the reserve of this fuel is continuously reduced with the consumption. This reduction is pushing the prices higher and higher, which makes economic problems to the non-oil-producer countries. Burning the fossil fuel is always associated with entropy rise and serious environmental pollution due to the combustion products, mainly, the carbon monoxide CO, hydrocarbons HC, particulate matters PM and the nitrogen oxides NO<sub>x</sub> compounds. These two reasons made harnessing as high energy as possible from the supplied fuel to the engine is an inevitable task for the researchers and the engines designers.

The internal combustion engines ICEs have the bigger portion of the fossil fuel consumption among the other types of engines. Out of the supplied heat to the engine in form of fuel, there's approximately 30 – 40 % converted to a useful mechanical work, and the rest is wasted to the environment, mainly through the exhaust gases and the cooling water. However, engines are operating over a wide range of conditions – idling, accelerating, cruising, and stop-and-go – making the engine operates away from its ideal efficiency point. Under normal driving conditions the average efficiency of IC engines drops to approximately 20%. This is significantly lower than typical electricity-generating power plants that are between 35-55% efficient, but IC engines in cars do operate under a more restrictive set of constraints, primarily the large range of operating conditions, small sizes, and low weight requirements.

Therefore, it is imperative that serious and concrete effort should be launched for conserving this energy through waste heat recovery techniques. Such a waste heat recovery would ultimately reduce the overall energy requirement and also the impact on global warming. Over the past century, the Internal Combustion Engines have been a primary power source for automobiles.

Inserting turbochargers, enhancing the air-fuel mixing and implementing variable valve timing are among the methods that the manufacturers thought about and eventually have done in order to increase the thermal energy of the ICE engine. However, still about two thirds the available energy is being lost and needs to be recovered. Moreover, increasingly stringent emissions regulations are causing engine manufacturers to limit combustion temperatures and pressures lowering potential efficiency gains [51].

As the most widely used source of primary power for machinery critical to the transportation, construction and agricultural sectors, engine has consumed more than 60% of fossil oil. On the other hand, legislation of exhaust emission levels has focused on CO, HC, NO<sub>x</sub>, and PM. Energy conservation on engines is one of the best ways to deal with these problems since it can improve the energy utilization efficiency of the engine and

reduces emissions [42] Waste heat recovery systems has a significant impact on both reducing the fuel consumption and the environmental pollution and also increase the thermal efficiency of the engine.

In recent years the scientific and public awareness on environmental and energy issues has brought in major interests to the research of advanced technologies particularly in highly efficient internal combustion engines. The number of vehicles (passenger and commercial vehicles) produced from 2005 to 2010 shows an overall increasing trend from year to year despite major global economic down turn in the 2008 – 2010 periods (Fig. 1). Note that China's energy consumption in transportation sector is the lowest (13.5%) [45]. Although the country produced the highest number of vehicles in 2009 to 2010 as compared to the other countries (Table 1). Viewing from the socio-economic perspective, as the level of energy consumption is directly proportional to the economic development and total number of population in a country.

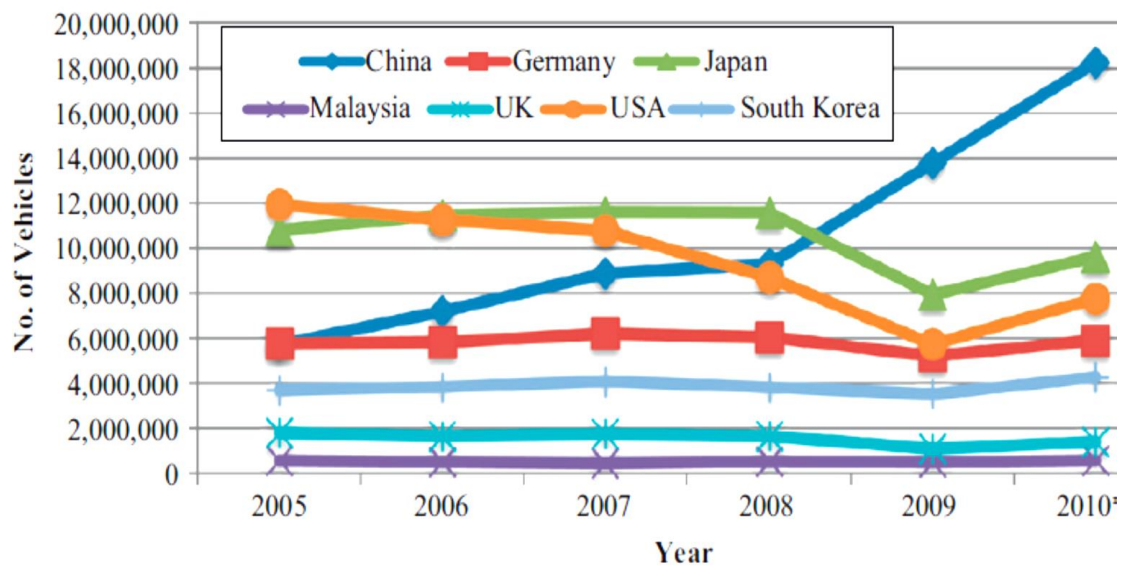


Figure 1.1 Production of vehicles from 2005 to 2010 for selected countries, [87].

*Table 1.1: Terminal energy consumption structure by region and sector, [87].*

Regions	Total consumption	Energy consumption by sector			
		Industry	Transportation	Agricultural/ commerce/civil	Non-energy use
<b>China</b>	597	327 (54.8) <sup>a</sup>	80.5 (13.5)	165 (27.6)	24.5 (4.1)
<b>USA</b>	1597	394 (25.3)	623 (40.0)	475 (30.5)	65.4 (4.2)
<b>EU (15)</b>	1057	320 (30.3)	321 (30.4)	386 (36.5)	30.2 (2.8)
<b>Japan</b>	359	135 (37.6)	94.4 (26.3)	119 (33.2)	10.5 (2.9)
<b>OECD</b>	3692	1106 (30.0)	1242 (33.6)	1120 (33.0)	125 (3.4)
<b>Total in the world</b>	6212	2144 (34.5)	1831 (29.5)	2035 (32.8)	201 (3.2)

<sup>a</sup> Percentage value inside the parenthesis.

## 1.1 The Resources of the Waste Heat Energy in Automobiles

As we try to improve IC engines, it's important to understand where the inefficiencies arise. Figure 1.2 shows the breakdown of where the incoming energy from fuel that is available for work output is going. A typical IC engine will lose 20% of its available work to the combustion process, 27% is transferred out as heat, and 16% is transferred out with the exhaust. This leaves only 35% of the energy available as work to move the vehicle. Maximizing the work output therefore can be accomplished by reducing the heat transfer, extracting the available energy from the exhaust, and reducing the inefficiency associated with combustion. Reducing losses due to heat transfer and exhaust are more easily tackled with current technologies [36] and [28]. The figure 1.2 also shows the efficiency with advanced low temperature combustion modes. Presented by Dave Foster from the University of Wisconsin. The leftmost bar is for conventional diesel combustion. The bars to the right depict observations for various forms of low temperature combustion, including partially premixed compression ignition (PPCI) and dual fuel PPCI. All efficiencies depicted are based on first law analysis. Loss terms indicated at the top of the bar graphs represent incomplete combustion of fuel.

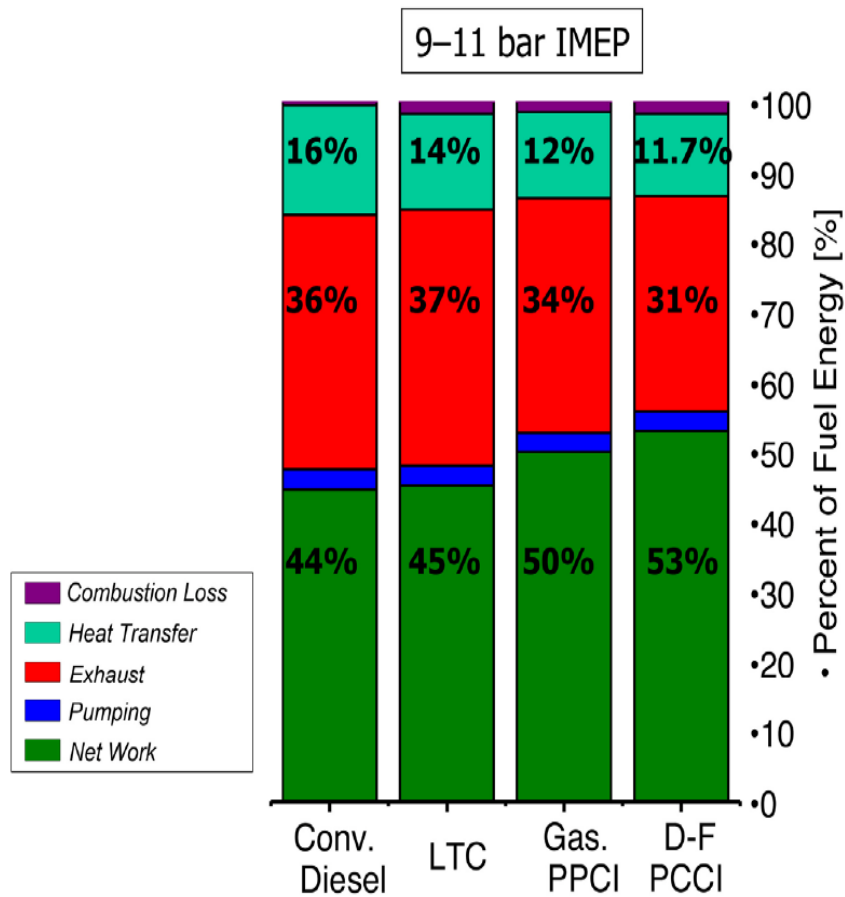


Figure 1.2: Recent achievements in peak indicated thermal efficiency in diesel engines, [28].

Many companies and research centers have come up with ideas to harness the heat in the exhaust gases and the cooling water, one of them was the BMW group where a model to the heat recovery has been introduced. The model is obviously a closed cycle with a particular working fluid, and the cycle consists mainly of heat exchanger to exchange the heat from the high temperature flow stream to the working fluid, pump, and the main part which is in this case an expander, the cycle is shown in figure 1.3 below.



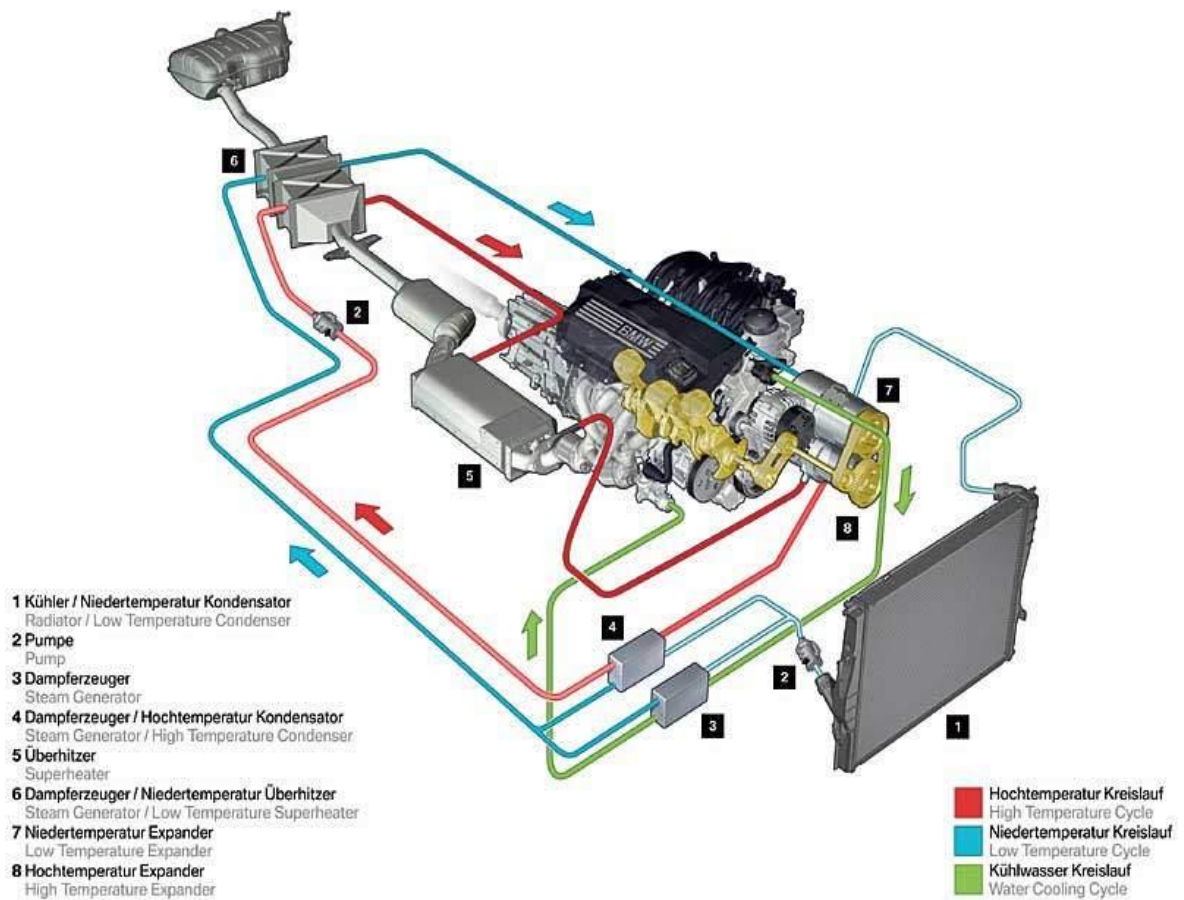


Figure 1.3 The heat recovery cycle, [98].

In our work, it will be focused on the part which is extracting the energy from the working fluid and producing the recovered mechanical work, which is by far, the most crucial and important part. For such application, which requires that the added parts to the body of the automobile have to be as small in size as possible and weigh as light as possible. Taking that into considerations, we choose the radial inflow turbine (RIT) to be the part which extracts and recovers the working fluid energy.

Choosing this kind of turbomachines was due to the exceling features of the radial turbine over the other types for this particular application.

The more compact turbine for power generation the more power density required to cope with the miniature turbomachine, to achieve this target the assigned machine has to run with a high rotational speed (sometimes 100,000-1M rpm [98]) and even more, so that, a new restriction will arise as a result of this high speed and high balancing technique must be utilized and that means the aerodynamic performance must be investigated and optimized together with the mechanical stresses analysis. A compromise must be

achieved, holding the efficiency of the radial turbine as high as possible have to be approached and care must be given to the mechanical properties in order not to let the mechanical stresses on the blade exceed a specified value of the material yield stress, keeping in mind that the centrifugal stresses that arise and exert on the turbine rotor blades is increasing with the increasing of the rotational speed and the material density, in addition to that the effect of the flow itself on the pressure side of the rotor blades.

BMW engineers used a turbosteamer to reclaim a significant amount of the wasted heated and they got a reduction in the fuel consumption by 15% and they expected to see this car on the road within the next decade [98].

A study by researchers at Loughborough University and the University of Sussex, both in the UK, has concluded that using waste heat from light-duty vehicle engines in a steam power cycle could deliver fuel economy advantages of between 6.3% and 31.7%, depending upon drive cycle, and that high efficiencies can be achieved at practical operating pressures. The basic concept of the “steam hybrid” system is that energy is recovered from the exhaust in the form of a steam/water mixture. Shaft work is produced as steam is expanded [43].

The greatest advantage of the radial turbine over the axial turbine is that the work produced by a single stage is equivalent to that of two or more stages in an axial turbine, and this property because of the radial inflow turbine usually has a higher tip speed than an axial turbine, and since the power output is a function of the square of the tip speed, for a given flow rate, the work is greater than in a single stage axial flow turbine [107]. Addition to that the cost of the radial inflow turbine is much lower than that of the axial turbine, another special advantage is that the efficiency of the radial turbine is more than that of the axial one and particularly when the Reynolds numbers are between  $Re=10^5 - 10^6$  [58]. Another advantage is that the radial turbine is much easier to manufacture and fabricate than the axial turbine.

Mainly the radial inflow turbine consists of the following parts:

1. Volute.
2. Nozzle blades.
3. Rotor blades, hub and sometimes with shroud.
4. Diffuser.

Each part has its own design requirements and limitations, the volute geometry must be satisfied with the mass, momentum and the energy equations, whether the nozzle is normally designed as a simple passage with a constant width and its function is to direct the flow with a specific angle and whirl component and the flow is accelerated before being delivered to the impeller, the rotor blade is more sophisticated part and care must be taken to many parameters in the design process and the number of rotor blades must be optimized, normally 9 to 19 blades [107].

The diffuser is to convert part of the kinetic energy from the leaving flow to a static pressure and this leads to raise the process efficiency and here care must be given because of the low-energy boundary layer may not tolerate the great adverse pressure gradient. The fatigue in the radial inflow turbine exducer (the exit section of the rotor) is a serious problem, so the exducer should be designed so that the natural frequency is higher than the blade passing frequency. The figure (1.3) shows a schematic view of the main parts of the radial inflow turbine, where the inflow comes normally from a collector or a volute and the outlet of the rotor may get into an exhaust diffuser.

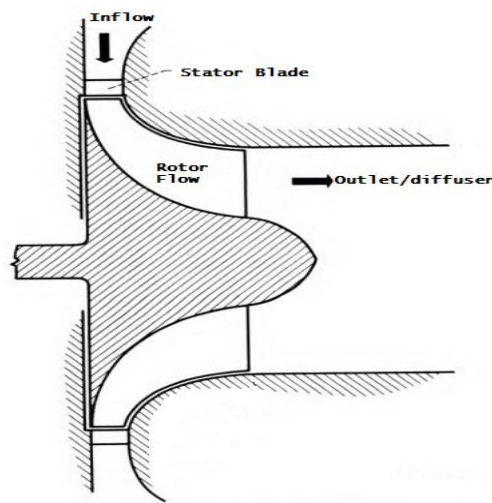


Figure 1.4 A schematic of radial inflow components.

The losses of the radial turbine are internal and external losses. The internal losses are basically from the heat loss, incidence loss, diffusion or loading loss, clearance loss and friction loss and these losses are normally minimal at the design point and increase in the off-design points (the design point normally set by a specified design parameters such as: specific speed, specific diameter and flow coefficient). However the external losses are from the disc friction, the bearing, the gear and the seal [74].

## 1.2 Design approach

The approach we suggested to deal with designing an appropriate turbine for our application is to use a radial inflow turbine, as we discussed in the previous section, the cycle through which the waste heat energy will be recovered is a Rankin cycle and the working fluid we used is an organic fluid.

That means we are using an Organic Rankin cycle ORC, and choosing an organic fluid to be our working fluid has many reasons, the first is that the low-grade temperature heat

from the exhaust cannot be efficiently converted to electrical power by using conventional methods, and also to make sure that the flow passes in the rotor blade passages will not slip in the two-phases region, i.e. the working fluid has to be super dry to avoid the corrosion problems and also the liquid drops in the flow make a turbulence and hence much losses.

Calculating the thermodynamic properties of a real gas is needed and to be coupled with CFD solver to get accurate viscous simulation results. CFD solvers capable of handling real gas have been developed since the end of the 90s [25] and [47]. BONCINELLI [19] was one of the pioneer on performing a three dimensional viscous simulation for a transonic centrifugal impeller using R134a using fitting model from gas database to get the thermodynamic properties. An optimization of the expander blades using a real gas has been made by PASQUALE [71], and CHO [24]. Peng-Robinson-Stryjek-Vera and Span-Wagner are good models for predicting the gas properties [90]

In this work we used the Redlich-Kwong empirical equations to deal with the real gas thermodynamic properties, which is accurate in giving adequate results [78].

The optimization procedures have been thoroughly explained. We used in the optimization process the Design of Experiments, DOS, in the Design Exploration to get the design points. These design points have been generated subjected to our upper and lower bounds.

The sensitivity of the output parameters to the input parameters is a graphically shown. Then the Response Surface method has been used and by employing the ANN Artificial Neural Network technique, we get a global response surface. The Multi-Objective Genetic Algorithm MOGA method is then used to explore the global optimization design points for the system of multi input multi output parameters.

After finding the design candidate points, we run the simulation for each candidate point and the main performance parameters are to be further investigated in this stage of design.

## 1.3 Thesis Structure

The motivation of this work is a part of the global interest in reducing the fossil fuel consumption for both economic and environmental sakes.

The wasted heat in the exhaust gases is a well-known problem by all the ICEs designers and researchers, and hence, the need of recovering this energy relates to the classical problems in ICEs manufacturing laboratory and their academic research counterparts. Producing an equipment i.e. turbomachine which is capable of efficiently harnessing this energy, was always the most important subject in the research, as it has to be as small as

possible, and thus, it should run as fast as possible to compensate the miniature effect and produce a valuable amount of power.

In this work we introduced a radial inflow turbine, to be the heart of a cycle that recovers the wasted energy from both the exhaust manifold and the cooling system. The radial turbine has very interesting properties that fits the requirements of our application, as it produces much more specific power than it axial and other turbomachines types. Also it is robust, easy to manufacture and has a lower cost.

In chapter 2 we discussed the fundamentals of fluid mechanics and the main governing equations need to be implemented and eventually solved to understand the flow through the different component of the turbine. The numerical simulation methods have been also described. This chapter is also discussing the turbulence modelling for CFD and the important turbulence methods used have been also introduced. The effect of the compressibility and Favre averaging have taken a great deal.

The FVM has been discussed in chapter 3. The vast majority of the industrial CFD software depend on the finite volume method. The fundamental and the background of this method has been discussed as well as the numerical development. This chapter also covers the discrete techniques for the physical domain, the fluid motion equation, the application of boundary conditions, the solvers and their numerical implementation.

Chapter 4 describes the fundamental of turbomachines design. The main design parameters and the dimensionless coefficients have been explained. The radial turbine aerodynamic considerations, the turbine sizing and the geometry constraints have been also presented. The equation of state of real gases and the analysis method used are also explained in details.

In chapter 5, the discussion was focusing on the numerical simulation of the flow in the radial turbine and the results of this simulation. A validation of the results have been introduced. The convergence criteria, a mesh independent analysis have also been accomplished. The simulation settings and the effect of the turbulence models used are also presented.

Chapter 6 consists of two parts. The first part is the optimization background of the optimization methods and techniques used, such as the genetic algorithm GA, the Design of Exploration DoE, response surface and the six sigma analysis. The second part contains the results of the optimization procedures. After having optimum candidate design points, we applied them to the project and ran the simulation again to get the optimum performance at the new design point.

In chapter 7 we discussed the results in chapter 6 and chapter 7, and presented the conclusions. For the future works, we wrote some recommendations to be a guidelines in a further academic researches.



## 2 Theory of Fluid Dynamics

The governing equation of fluid flow represents mathematical statements of the conservation law of physics:

- The mass of fluid is conserved.
- The rate of change of momentum is equal to the algebraic sum of the forces on a fluid particle (Newton's second law).
- The rate of change of energy is equal to the sum of the rate of heat addition to and the rate of work done on a fluid particle (first law of thermodynamics).

Analyzing these governing equations is the corner stone of studying the fluid flow in the turbomachines. For the compressible flow, the fluid flow velocity components  $u_i$ , the pressure value  $p$ , the gas density  $\rho$  and the thermodynamic variables  $e$  and  $h$  at every spatial and time coordinates are fully characterizing the fluid flow motion. For the incompressible fluids, there's no change in density and the thermodynamic properties throughout the fluid motion.

All the CFD-Programs together try to solve these conservation equations to compute and resolve the fluid field and make an accurate simulation. The simulation technology in many industrial application is getting rapidly improved, and this improvement is partly attributed to the new CFD techniques and models, as mentioned in JIYUAN [54].

These equations can be written in two forms, integral form and differential form, the integral form is a finite control volume and can be solved using the finite volume method, it is physically easier to be understood and is more accurate in dealing with the discontinuity and the shock waves cases but it is more complex as integrals will show up. On the other hand, the differential form is an infinitesimal control volume and could be dealt with by applying the finite difference method, it is mathematically easier to be understood but physically more complex as the volumes of the elements go to zero.

In general, in the modern CFD-Programs, the integral form, especially the Finite Volume Method FEM, is applied. It can capture the shock-wave better than the differential form, because it has discontinuities in the control volume, on the other hand the differential form i.e. the finite difference discretization requires that the flow properties in the control volume is differentiable, in other words, it has to be continuous, but that is not the case, for example, in the shock wave.

The conservation of mass or the continuity equation can be defined as follows:

$$\frac{\partial \rho}{\partial t} + \frac{\partial(\rho u_i)}{\partial x_i} = 0 \quad (2.1)$$

The equation above is the unsteady, three-dimensional mass conservation at a point in a compressible fluid.

The equation of conservation of momentum or the Navier-Stokes equations, is written as follows:

$$\frac{\partial(\rho u_i)}{\partial t} + \frac{\partial(u_j \rho u_i)}{\partial x_j} = -\frac{\partial p}{\partial x_i} + \frac{\partial t_{ij}}{\partial x_j} \quad (2.2)$$

The field force  $f_i$  has to be added if it is not absent and it would be at the right hand-side of the equation above. The first term represents the instantaneous moment variation, the second is the convective term, the third involves the pressure gradient, which can be thought as the source term in transport equations, and the last is the diffusion term. The viscous stress tensor,  $t_{ij}$ , involves the deformation tensor,  $S_{ij}$ . The formula is valid for Newtonian fluids and assumes the Stokes hypothesis for the second viscosity,  $\lambda = \frac{2}{3}\mu$ , which is correct for monoatomic gases and almost always adopted in computational fluid dynamics (CFD) and is defined as follows:

$$t_{ij} = 2 \mu S_{ij} - \frac{2}{3} \mu \frac{\partial u_k}{\partial x_k} \delta_{ij} \quad (2.3)$$

And the deformation tensor is given as follows

$$S_{ij} = \frac{1}{2} \left( \frac{\partial u_i}{\partial x_j} + \frac{\partial u_j}{\partial x_i} \right) \quad (2.4)$$

The third governing equation is the energy conservation law and is constituted by the internal energy, the enthalpy, and the heat flux, which is by far a more complex expression. The viscous tensor also appears representing the way that part of the moment is dissipated by the fluid viscosity in internal energy, the energy equation can be represented as follows:



$$\frac{\partial(\rho e_t)}{\partial t} + \frac{\partial(u_j \rho h_t)}{\partial x_j} = -\frac{\partial q_j}{\partial x_j} + \frac{\partial u_i t_{ij}}{\partial x_j} \quad (2.5)$$

Where  $e_t$  is the total internal energy and defined as follows:

$$e_t = e + \frac{1}{2} u_i u_i \quad (2.6)$$

The total enthalpy  $h_t$  is given also as follows:

$$h_t = h + \frac{1}{2} u_i u_i \quad (2.7)$$

$$h = e + p/\rho \quad (2.8)$$

$q_j$  is obtained from the Fourier heat flux law, and given as follows:

$$q_j = -k \frac{\partial T}{\partial x_j} \quad (2.9)$$

It's clear from the above governing equation that they are a coupled system of non-linear partial differential equations and are very difficult to be solved analytically and there's no general closed-form solution to these equations, as in ANDERSON et al. [2].

It is obvious that we have six unknowns and five equation, three for the momentum, the continuity and the energy equation, and thus we need another equation to close the system, which is the equation of state which relates the pressure,  $p$ , the density,  $\rho$  and the temperature  $T$ . in aerodynamics, it is general to assume the gas is a perfect gas, which assumes the intermolecular forces are negligible, as in ANDERSON [3]. What is also worth telling, is that the equation of momentum is identified as the Navier-Stokes equation, which is historically correct. However, in the modern CFD literature, this terminology has been extended to include the entire system of flow equations for the solution of viscous flow i.e. the continuity, the energy and as well as the equation of momentum, and that means, the solution of Navier-Stokes equations is the numerical solution of the complete system of the governing equations, said ADERSON et al. [2].

## 2.1 Turbulent Flow Modelling

In engineering practice all the encountered flow is becoming unstable above a certain Reynolds number. At higher Reynolds numbers flows are observed to become turbulent. A chaotic and random state of motion develops in which the velocity and pressure change continuously with time within substantial regions of flow. Just in simple cases the continuity and the Navier-Stokes equations can be solved analytically [1]. More complex flows can be tackled numerically with CFD techniques such as the finite volume method without additional approximations. Many, if not most, flows of engineering significance are turbulent, so the turbulent flow regime is not just of theoretical interest [23]. The Reynolds number of a flow gives a measure of the relative importance of inertia forces (associated with convective effects) and viscous forces. It has been observed that at a value below a critical Reynolds number  $Re_{crit}$ , the flow is smooth and the adjacent layers of fluid slide past each other in an orderly fashion, and if the flow is steady the regime is laminar. At a value above  $Re_{crit}$  the velocity and other properties vary in a very random way and chaotic and the flow eventually becomes turbulent.

In the case of inviscid or laminar flows the solution of the governing equations does not raise any fundamental difficulties. The simulation of turbulent flows presents a significant problem. Despite the performance of modern supercomputers, a direct simulation of turbulence by the time-dependent Navier-Stokes equations, called Direct Numerical Simulation (DNS), is still possible only for rather simple flow cases at low Reynolds numbers ( $Re$ ), as in BLAZEK [18]. When recalling that the number of grid points needed for sufficient spatial resolution scales as  $Re^{9/4}$  and the CPU-time as  $Re^3$ , the restrictions of the DNS become quite obvious. However, this does not mean that DNS is completely useless. It is an important tool for understanding the turbulent structures and the laminar-turbulent transition. DNS also plays a vital role in the development and calibration of new or improved turbulence models. In engineering applications, the effects of turbulence can be taken into account only approximately, using models of various complexities.

Large-Eddy Simulation (LES) approach is the first level of approximation reached for that. The development of LES is founded on the observation that the small scales of turbulent motion possess a more universal character than the large scales, which transport the turbulent energy. Thus, the idea is to resolve only the large eddies accurately and to approximate the effects of the small scales by relatively simple subgrid-scale model. The investigation of turbulent flows at much higher Reynolds numbers becomes feasible since LES requires significantly less grid points than DNS. But because LES is inherently three-dimensional and unsteady, it remains computationally very demanding.

LES is also very promising for more accurate computations of flows in combustion chambers or engines, heat transfer and of rotating flows [76].

The approximation represented by the so-called Reynolds-Averaged Navier-Stokes equations (RANS) which was presented by Reynolds in 1895, is based on the decomposition of the flow variables into mean and fluctuating parts followed by time or ensemble averaging REYNOLDS O. [80], SCHLICHTING [91] and YOUNG [112].

In cases where the density is not constant, it is advisable to apply the density (mass) weighted or Favre decomposition to the velocity components, as in FAVRE [33] and [34]. Otherwise, the averaged governing equations would become considerably more

complicated due to additional correlations involving density fluctuations. It is common to assume that Morkovin's hypothesis [68] is valid, which states that the turbulence structure of boundary layers and wakes is not notably influenced by density fluctuations for Mach numbers below 5. A typical point velocity measurement in a turbulent flow is shown in figure 2.1 below

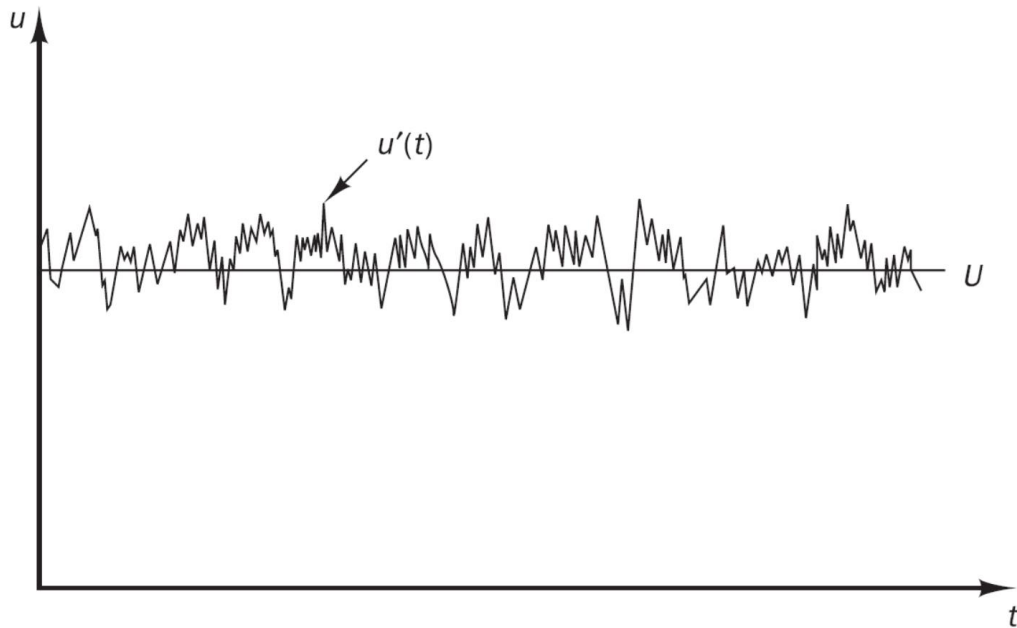


*Figure 2.1 Typical point velocity measurement in a turbulent flow, velocity versus time, [65].*

Instead of the velocity in figure 2.1, it can be decomposed into two parts, a steady mean value  $U$  and the fluctuation component  $u'(t)$ , so that

$$u(t) = U + u'(t) \quad (2.1)$$

And this is called the Reynold decomposition. A turbulent flow can now be characterized in terms of the mean values of flow properties ( $U, V, W, P$  etc.) and some statistical properties of their fluctuations ( $u', v', w', p'$  etc.). The turbulent flow is always have a three dimensional spatial character and has eddied with a wide range of length scale and the largest turbulent eddies interact with and extract energy from the mean flow by a process called vortex stretching.

observing a single point measurement in a turbulent flow, say a velocity measurement made with a hot-wire anemometer or a laser Doppler anemometer or a local pressure measurements made with a small transducer, and as we saw in the figure 2.1 that the

appearance of turbulence manifested itself as random fluctuations of the measured velocity component about a mean value. All other flow variables, i.e. all other velocity components, the pressure, temperature, density etc., will also exhibit this additional time-dependent behavior.

The Reynolds decomposition defines flow property  $\phi$  at this point as the sum of a steady mean component  $\Phi$  and a time varying fluctuating component  $\phi'(t)$  with zero mean value: hence,

$$\phi(t) = \Phi + \phi'(t) \quad (2.2)$$

The time average or the mean value  $\Phi$  of the flow property  $\phi$  can be defined as follows

$$\Phi = \frac{1}{\Delta t} \int_0^{\Delta t} \phi(t) dt \quad (2.3)$$

if  $\Delta t$  is larger than the time scale associated with the slowest variations (due to the largest eddies) of property  $\phi$ , the equation 2.3 will give a meaningful time average although in the theory  $\Delta t$  has to approach the infinity, MALALASEKERA [65]. This definition of the mean of a flow property is adequate for steady mean flows. In time-dependent flows the mean of a property at time  $t$  is taken to be the average of the instantaneous values of the property over a large number of repeated identical experiments. By definition, the time average of the fluctuation property  $\phi'(t)$  is zero,

$$\overline{\phi'(t)} = \frac{1}{\Delta t} \int_0^{\Delta t} \phi'(t) dt \quad (2.4)$$

The variance and root mean square (r.m.s.) are the descriptors used to indicate the spread of the fluctuations  $\phi'$  about the mean value of  $\Phi$ ,

$$\overline{\phi'(t)^2} = \frac{1}{\Delta t} \int_0^{\Delta t} (\phi'(t))^2 dt \quad (2.5a)$$

$$\phi_{rms} = \sqrt{\overline{\phi'(t)^2}} = \left[ \frac{1}{\Delta t} \int_0^{\Delta t} (\phi'(t))^2 dt \right]^{1/2} \quad (2.5b)$$

The r.m.s. Values of the velocity components are generally most easily measured and express the average magnitude of velocity fluctuations since they are generally most easily measured and express the average magnitude of velocity fluctuations.

One can express the total kinetic energy per unit mass  $k$  of the turbulence at a given location as follows:

$$k = \frac{1}{2} [\overline{u'^2} + \overline{v'^2} + \overline{w'^2}] \quad (2.6)$$

The turbulence intensity  $T_i$  is the average r.m.s. velocity divided by a reference mean flow velocity  $U_{ref}$  and is linked to the turbulence kinetic energy  $k$  as follows

$$T_i = \frac{(\frac{2}{3} k)^{1/2}}{U_{ref}} \quad (2.7)$$

The variance is also called the second moment of the fluctuations. Important details of the structure of the fluctuations are contained in moments constructed from pairs of different variables, the second moment of them, as for the velocity components  $u, v$  is

$$\overline{u'v'} = \frac{1}{\Delta t} \int_0^{\Delta t} u'v' dt \quad (2.8)$$

The values of the second moments of the velocity components  $u'v, u'w'$  and  $w'v$  would be equal to zero if velocity fluctuations in different directions were independent random fluctuations. Also, pressure–velocity moments  $p'u', p'v'$  etc., play a role in the diffusion of turbulent energy.

The Reynolds-Averaged Equation for incompressible flow will be written and then the effect of the compressibility will be taken later in this chapter. The equations for conservation mass and momentum are

$$\frac{\partial u_i}{\partial x_i} = 0 \quad (2.9)$$

$$\rho \frac{\partial u_i}{\partial t} + \rho u_j \frac{\partial u_i}{\partial x_j} = -\frac{\partial p}{\partial x_i} + \frac{\partial t_{ji}}{\partial x_j} \quad (2.10)$$

The  $t_{ji}$  is the viscous stress tensor

$$t_{ji} = 2 \mu S_{ij} \quad (2.11)$$

The  $S_{ij}$  is the strain rate tensor and

$$S_{ij} = \frac{1}{2} \left( \frac{\partial u_i}{\partial x_j} + \frac{\partial u_j}{\partial x_i} \right) \quad (2.12)$$

Then the Reynolds averaged equations of motion in conservation form can be written as

$$\frac{\partial U_i}{\partial x_i} = 0 \quad (2.13)$$

$$\rho \frac{\partial u_i}{\partial t} + \rho u_j \frac{\partial}{\partial x_j} (U_j U_i + \overline{u'_j u'_i}) = -\frac{\partial p}{\partial x_i} + \frac{\partial}{\partial x_j} (2 \mu S_{ij}) \quad (2.14)$$

And the equation above can be written in more recognizable form as follows

$$\rho \frac{\partial u_i}{\partial t} + \rho u_j \frac{\partial}{\partial x_j} (U_j U_i) = -\frac{\partial p}{\partial x_i} + \frac{\partial}{\partial x_j} (2 \mu S_{ij} - \overline{\rho u'_j u'_i}) \quad (2.15)$$

The equation above is usually referred to as the Reynolds-averaged Navier-Stocks equation RANS and the quantity  $-\overline{\rho u'_j u'_i}$  is the Reynolds-stress tensor and we can denote it  $-\rho \tau_{ij}$  where  $\tau_{ij}$  is the specific Reynolds-stress tensor, which is a symmetric tensor.

Hence, we have produced six unknown quantities as a result of Reynolds averaging. Unfortunately, we have gained no additional equations and for general three-dimensional flows, we have four unknown mean-flow properties, pressure and the three velocity components along with the six Reynolds-stress components, we thus have ten unknowns. Our equations are mass conservation and the three components of the RANS Equation for a grand total of four. This means our system is not yet closed MALALASEKERA [65].

To close the system we have to have the same number of equations and the unknowns. So, we will take the moment to the Navier-Stocks Equation. That is, we multiply the Navier-Stokes equation by a fluctuating property and time average the product. Using this procedure, we can derive a differential equation for the Reynolds-stress tensor, ANDERSON [3].

After tedious procedures and rearranging the Reynolds-stress equation in a suitable compact form we can get the following equation viz.

$$\begin{aligned} \frac{\partial \tau_{ij}}{\partial t} + U_k \frac{\partial \tau_{ij}}{\partial x_k} = & -\tau_{ik} \frac{\partial U_j}{\partial x_k} - \tau_{jk} \frac{\partial U_i}{\partial x_k} + \epsilon_{ij} - \Pi_{ij} \\ & + \frac{\partial}{\partial x_k} \left[ \nu \frac{\partial \tau_{ij}}{\partial x_k} + C_{ijk} \right] \end{aligned} \quad (2.16)$$

Where

$$\Pi_{ij} = \frac{p'}{\rho} \left( \frac{\partial u'_i}{\partial x_j} + \frac{\partial u'_j}{\partial x_i} \right) \quad (2.17)$$

$$\epsilon_{ij} = 2\nu \frac{\partial u'_i}{\partial x_k} \frac{\partial u'_j}{\partial x_k} \quad (2.18)$$

$$\rho C_{ijk} = \overline{\rho u'_i u'_j u'_k} + \overline{p' u'_i} \delta_{jk} + \overline{p' u'_j} \delta_{ik} \quad (2.19)$$

As the Navier-Stokes equation is a non-linear in nature, the unknowns will get higher if take a higher momentum and additional unknowns will be generated, and by no point the number of unknowns will be equal to the number of equations, as we don't produce additional physical principles the situation will remains strictly mathematical. Essentially, Reynolds averaging equation has a brutal simplification that leads to lose much information from the Navier-Stokes equation. And the function of the turbulence modeling is to advice approximation for the unknown correlations in term of flow properties that are known to close the system.

For the smallest eddies in a turbulent flow Kolmogorov scales provide an estimation of the length, velocity and time scales. The integral length scale can be also regarded as a characteristic value of the energy-bearing eddies. Another important measure of the any turbulent flow is how intense the turbulent fluctuations are. It can be quantified in term of specific normal Reynolds- stress components  $\overline{u^2}$ ,  $\overline{v^2}$  and  $\overline{w^2}$ . These three Reynold stresses can also be regarded as the kinetic energy per unit mass of the fluctuating velocity field in the three coordinate directions and these stresses are usually normalized relative to the freestream mean-flow velocity  $U_e$ , according to

$$\hat{u} = \frac{\sqrt{\overline{u^2}}}{U_e}, \hat{v} = \frac{\sqrt{\overline{v^2}}}{U_e}, \hat{w} = \frac{\sqrt{\overline{w^2}}}{U_e} \quad (2.20)$$

The quantities  $\hat{u}$ ,  $\hat{v}$  and  $\hat{w}$  are the relative intensities in  $x$ ,  $y$  and  $z$  directions respectively. And if we sum the three Reynolds stresses and divided it to two we get the turbulence kinetic energy  $k$

$$k = \frac{1}{2}(\overline{u^2} + \overline{v^2} + \overline{w^2}) = \frac{1}{2}\overline{u'_i u'_i} \quad (2.21)$$

## 2.2 Eddy Viscosity models

Joseph Boussinesq was the first practitioner of modeling the Reynolds stress, introducing the concept of eddy viscosity. In 1887 Boussinesq proposed relating the turbulence stresses to the mean flow to close the system of equations. Here the Boussinesq hypothesis is applied to model the Reynolds stress term. Note that a new proportionality constant  $\nu_t > 0$ , the turbulence eddy viscosity, has been introduced. Models of this type are known as eddy viscosity models or EVM's and the main types are the one-equation model and the two-equation model, the latter is the mostly used model. Both of these models retain the Boussinesq eddy-viscosity approximation, but differ in one important respect. One-equation models are incomplete as they relate the turbulence length scale to some typical flow dimension. By contrast, two-equation models provide an equation for the turbulence length scale or its equivalent and are thus complete.

To complete closure of the turbulence kinetic energy equation, Prandtl has postulated that the dissipation assumes the form quoted in Equation of the specific Reynold-tensor. Introducing a closure coefficient that we will call  $C_D$ , the dissipation is

$$\epsilon = C_D k^{3/2} / \ell \quad (2.22)$$

And the turbulence length scale remains the only unspecified part of the model. Prandtl could establish prescriptions for the turbulence length scale  $\ell$ . Note that in a thin shear layer gives  $\frac{\partial U}{\partial y} = (\overline{u'v'})^{1/2} / \ell_{mix}$ . So, balancing production and dissipation means  $-(\overline{u'v'}) \frac{\partial U}{\partial y} = (\overline{u'v'})^{3/2} / \ell_{mix} = C_D k^{3/2} / \ell$ , So that the  $\ell \propto \ell_{mix}$  if  $\overline{u'v'} / k = \text{Constant}$ .



Thus the Prandtl One-Equation Model is as follows:

$$\frac{\partial k}{\partial t} + U_j \frac{\partial k}{\partial x_j} = \tau_{ij} \frac{\partial U_i}{\partial x_j} - C_D k^{3/2} / \ell + \frac{\partial}{\partial x_j} \left[ \nu + \nu_T / \sigma_k \frac{\partial k}{\partial x_j} \right] \quad (2.23)$$

Where  $\tau_{ij}$  is  $2\nu_T S_{ij} - \frac{2}{3} \delta_{ij}$

Baldwin and Barth, Spalart and Allmars and Menter have device even more elaborate model equations for eddy viscosity. Baldwin and Barth, for example, includes seven closure coefficient and three damping functions.

## 2.3 Two-Equation models

During the past two decades the Two-Equation models of turbulence have served as the foundation for much of the turbulence model research. These models provide not only for computation of  $k$ , but also for the turbulence length scale or equivalent. Consequently, two-equation models are complete, i.e., can be used to predict properties of a given turbulent flow with no prior knowledge of the turbulence structure.

### 2.3.1 The $k$ - $\epsilon$ Model

Until the last decade in the last century this turbulence was by far the most popular Two-Equation model among the other ones, it has been commonly used in the industry and especially in the field of turbomachinery designing researches. In 1974 Launder and Sharma subsequently returned the model's closure coefficients and created what is generally called the standard  $k$ - $\epsilon$  model. By taking the following moment to the Navier-Stokes equation we can derive the exact equation for the  $\epsilon$  equation

$$2\nu \overline{\frac{\partial u_i}{\partial x_i} \frac{\partial}{\partial x_j} [N(u_i)]} \quad (2.24)$$

Where

$$N(u_i) = \rho \frac{\partial u_i}{\partial t} + \rho u_k \frac{\partial u_i}{\partial x_k} + \frac{\partial p}{\partial x_i} + \mu \frac{\partial^2 u_i}{\partial x_k \partial x_k} \quad (2.25)$$

After a tedious algebra we can get the exact equation for  $\epsilon$  which is as follows

$$\begin{aligned}
\frac{\partial \epsilon}{\partial t} + U_j \frac{\partial \epsilon}{\partial x_j} = & -2 \nu \overline{[u'_{i,k} u'_{j,k} + u'_{k,i} u'_{k,j}]} \frac{\partial U_i}{\partial x_i} - 2 \nu \overline{u'_k u'_{i,j}} \frac{\partial^2 U_i}{\partial x_k \partial x_j} \\
& - 2 \nu \overline{u'_{i,k} u'_{i,m} u'_{k,m}} - 2 \nu^2 \overline{u'_{i,m} u'_{k,m}} \\
& + \frac{\partial}{\partial x_i} \left[ \nu \frac{\partial \epsilon}{\partial x_i} - \overline{\nu u'_j u'_{i,m} u'_{i,m}} - 2 \frac{\nu}{\rho} \overline{p'_m u'_{i,m}} \right]
\end{aligned} \tag{2.26}$$

It is clear that the above equation is very complex and more complicated than the kinetic energy equation and contains several unknown correlations of fluctuated velocity, pressure and velocity gradients. Essentially these correlations are almost impossible to measure with any degree of accuracy so there's presently a little hope to find a reliable guidance from the experimentalists regarding a suitable closure approximations [65]. The strongest claim that can actually be made is that the conventional closure approximations used for Equation (2.26) are dimensionally correct. This is not very different from the Kolmogorov approaches that are guided almost exclusively by physical reasoning and dimensional analysis. We should keep a very important point in mind is to avoid modeling the differential equations rather than the physics of turbulence.

The Standard k- $\epsilon$  model is then as follow

The kinematic eddy viscosity

$$v_T = C_\mu k^2 / \epsilon \tag{2.27}$$

Turbulence kinetic energy

$$\frac{\partial k}{\partial t} + U_j \frac{\partial k}{\partial x_j} = \tau_{ij} \frac{\partial U_i}{\partial x_j} - \epsilon + \frac{\partial}{\partial x_j} \left[ (\nu + v_T / \sigma_k) \frac{\partial k}{\partial x_j} \right] \tag{2.28}$$

For the dissipation rate part the equation will be

$$\frac{\partial \epsilon}{\partial t} + U_j \frac{\partial \epsilon}{\partial x_j} = C_{\epsilon 1} \frac{\epsilon}{k} \tau_{ij} \frac{\partial U_i}{\partial x_j} - C_{\epsilon 2} \frac{\epsilon^2}{k} + \frac{\partial}{\partial x_j} \left[ (\nu + v_T / \sigma_\epsilon) \frac{\partial \epsilon}{\partial x_j} \right] \tag{2.29}$$

Where the closure coefficients will be

$$C_{\epsilon 1} = 1.44, \quad C_{\epsilon 2} = 1.92, \quad C_\mu = 0.09, \quad \sigma_k = 1.0, \quad \sigma_\epsilon = 1.3 \tag{2.30}$$

$$\omega = \epsilon / (C_\mu k) \quad \text{and} \quad \ell = C_\mu k^{3/2} / \epsilon \quad (2.31)$$

The equations above are involving viscous damping functions. Yachot and Arzagan have been developed a recent version of the  $k$ - $\epsilon$  model. They have used technique from the renormalization theory, they developed what's known as RNG  $k$ - $\epsilon$ . The eddy viscosity,  $k$  and  $\epsilon$  are still given in equations 2.32, 2.33 and 2.34, however the modeled used modified coefficient  $C_{\epsilon 2}$

$$C_{\epsilon 2} = \tilde{C}_{\epsilon 2} + \frac{C_\mu \lambda^3 (1 - \lambda / \lambda_0)}{(1 + \beta \lambda^3)}, \quad \lambda = \frac{k}{\epsilon} \sqrt{2S_{ij}S_{ji}} \quad (2.32)$$

The enclosure coefficients for the RNG  $k$ - $\epsilon$  model

$$C_{\epsilon 1} = 1.42, \quad \tilde{C}_{\epsilon 2} = 1.68, \quad C_\mu = 0.085, \quad \sigma_k = 0.72, \quad \sigma_\epsilon = 0.72 \quad (2.33)$$

$$\beta = 0.012, \quad \lambda_0 = 4.38 \quad (2.34)$$

### 2.3.2 The $k$ - $\omega$ Model

Kolmogorov chose the kinetic energy of the turbulence as one of his turbulence parameters and, like Prandtl, modeled the differential equation governing its behavior. His second parameter was the dissipation per unit turbulence kinetic energy,  $\omega$ . In his  $k$ - $\omega$  model,  $\omega$  satisfies a differential equation similar to the equation for  $k$ . Kolmogorov referred in formulating his model, to  $\omega$  as the rate of dissipation of energy in unit volume and time. He also called it some mean frequency determined by  $\omega = ck^{1/2}/\ell$  to underscore its physical relation to the external scale of turbulence,  $\ell$ , where  $c$  is a constant. The form of the equation for  $w$  has changed as the  $k$ - $\omega$  model has evolved over the past five decades and the following version of  $k$ - $\omega$  has been changed and improved the predictive accuracy of the Wilcox model for free shear flows and strongly separated flows.

Kinematic eddy viscosity

$$v_T = k/\tilde{\omega}, \quad \tilde{\omega} = \max\left\{\omega, C_{\text{lim}}\sqrt{\frac{2S_{ij}S_{ij}}{\beta^*}}\right\}, \quad C_{\text{lim}} = \frac{7}{8}$$

Turbulence Kinetic Energy

$$\frac{\partial k}{\partial t} + U_i \frac{\partial k}{\partial x_i} = -\tau_{ij} \frac{\partial U_i}{\partial x_j} - \beta^* k \omega + \frac{\partial}{\partial x_j} \left[ (\nu + v_T/\sigma^*) \frac{\partial k}{\partial x_j} \right] \quad (2.35)$$

Specific dissipation rate

$$\begin{aligned} \frac{\partial \omega}{\partial t} + U_j \frac{\partial \omega}{\partial x_j} = & \alpha \frac{\omega}{k} \tau_{ij} \frac{\partial U_i}{\partial x_j} - \beta \omega^2 + \frac{\sigma_d}{\omega} \frac{\partial k}{\partial x_j} \frac{\partial \omega}{\partial x_j} \\ & + \frac{\partial}{\partial x_j} \left[ (\nu + v_T/\sigma) \frac{k}{\omega} \frac{\partial \omega}{\partial x_j} \right] \end{aligned} \quad (2.36)$$

The closure coefficients and the auxiliary relations

$$\begin{aligned} \alpha = \frac{13}{25}, \quad \beta = \beta_0 f_\beta, \quad \beta^* = \frac{9}{100}, \quad \sigma = \frac{1}{2}, \quad \sigma^* = \frac{3}{5}, \\ \sigma_{d0} = \frac{1}{8} \end{aligned} \quad (2.37)$$

$$\sigma_d = \begin{cases} 0, & \frac{\partial k}{\partial x_j} \frac{\partial \omega}{\partial x_j} \leq 0 \\ \sigma_{d0}, & \frac{\partial k}{\partial x_j} \frac{\partial \omega}{\partial x_j} > 0 \end{cases} \quad (2.38)$$

$$\beta_0 = 0.0708, \quad f_\beta = \frac{1 + 85x_\omega}{1 + 100x_\omega}, \quad x_\omega = \frac{|\Omega_{ij} \Omega_{jk} S_{ki}|}{(\beta^* \omega)^3}$$

$$\epsilon = \beta^* \omega k \quad \text{and} \quad \ell = k^{1/2}/\omega \quad (2.39)$$

The value of  $x_\omega$  for the two dimensional flow and the tensors  $\Omega_{ij}$  and  $S_{ij}$  are the mean-rotation and mean strain rate tensors respectively and are defined

$$\Omega_{ij} = \frac{1}{2} \left( \frac{\partial u_i}{\partial x_j} - \frac{\partial u_j}{\partial x_i} \right), \quad S_{ij} = \frac{1}{2} \left( \frac{\partial u_i}{\partial x_j} + \frac{\partial u_j}{\partial x_i} \right) \quad (2.40)$$

Note that these equation can be used for general compressible flows by replacing  $\nu$ ,  $\nu_T$ ,  $\frac{k}{\omega}$ , and  $\frac{k}{\tilde{\omega}}$  by  $\mu = \rho \nu$ ,  $\mu_T = \rho \nu_T$ ,  $\rho k / \omega$ ,  $\rho k / \tilde{\omega}$  respectively and multiplying all but the diffusion terms by  $\rho$ , also, a mean-energy and equation of state must be added.

The main difference between this version of the  $k$ - $\omega$  model and the earlier versions of it are the cross diffusion  $\sigma_d$  and the built-in stress limiter, and those modifications have been proposed to eliminate the sensitivity to the free stream values of  $\omega$ .

One of its advantages is that it can be integrated up to the wall boundaries without the need to neither damping functions nor low Reynolds numbers corrections other advantage is that this model provides greatly improved prediction for the shock-separated flows without including any compressibility modifications to the model as it was required by the early version of this model to achieve reasonable results. One more advantage of this model is that it can predict free shear flow spreading rates much closer to the measurements, so that is applicable for both wall-bounded and free-shear flows.

## 2.4 The SST $k$ - $\omega$ Model

A two-layer model which employs the  $k$ - $\omega$  model of WILCOX [106] in the inner region of boundary layers and switches to a  $k$ - $\epsilon$  model in the outer region of boundary layers and in mixing regions MENTER [66] and [67]. This model makes use of the blend functions F1 and F2 to achieve the blending. The SST  $k$ - $\omega$  turbulence model is a two-equation eddy-viscosity model which has become very popular as the SST model has been found to provide very good calculations of wall bounded flows even with highly separated regions.

Reproducing the  $k$ - $\omega$  behavior in the viscous and logarithmic layers, where it can precisely describe the boundary layer dynamics, and to regain the  $k$ - $\epsilon$  characteristic in the defect layer, where it is less sensible to the free stream conditions, is actually the purpose behind developing this model. SST model combines both models to take the maximum advantage of their strengths in the distinct sub-layers of the boundary layer.

The kinetic energy,  $k$ , transport equation in the  $k$ - $\omega$  SST model, is the same as before, but the blending function is introduced in the turbulent dissipation frequency

$$\frac{\partial(\rho k)}{\partial t} + \frac{\partial(\bar{u}_j \rho k)}{\partial x_j} = \tau_{ij} \frac{\partial \bar{u}_i}{\partial x_j} - \beta^* \rho \omega k + \frac{\partial}{\partial x_j} \left[ (\mu + \rho_k \mu_T) \frac{\partial k}{\partial x_j} \right] \quad (2.41)$$

$$\begin{aligned}
& \frac{\partial(\rho\omega)}{\partial t} + \frac{\partial(\bar{u}_j\rho\omega)}{\partial x_j} \\
& = \frac{\gamma}{\nu_T} \tau_{ij} \frac{\partial \bar{u}_i}{\partial x_j} - \beta^* \rho \omega^2 + \frac{\partial}{\partial x_j} \left[ (\mu + \rho_k \mu_T) \frac{\partial \omega}{\partial x_j} \right] \\
& + 2(1 - F_1) \rho \sigma_{\omega 2} \frac{1}{\omega} \frac{\partial k}{\partial x_j} \frac{\partial \omega}{\partial x_j}
\end{aligned} \tag{2.42}$$

The last term comes from the transformation of the turbulent dissipation transport equation in the dissipation frequency transport equation. The factor (1 - F1) provides the blending from the  $k$ - $\epsilon$  with the  $k$ - $\omega$  model. Near to the wall boundaries,  $F1 \approx 1$  and  $(1 - F1) \approx 0$ , reproducing the original  $k$ - $\omega$  model. From the defect layer and going in the opposite direction of the wall boundaries,  $F1 \approx 0$  and  $(1 - F1) \approx 1$ , causing the equations to behave as the standard  $k$ - $\epsilon$  model.

As defined by MENTER [67] the blending functions are defined as follows

$$F_1 = \tanh(\text{arg}_1^4), \text{arg}_1 = \min \left[ \max \left( \frac{\sqrt{k}}{0,09\omega y}; \frac{500\nu}{y^2\omega} \right); \frac{4\rho\sigma_{\omega 2}}{CD_{k\omega}y^2} \right] \tag{2.43}$$

Where  $CD_{k\omega}$  has numerical limiters

$$CD_{k\omega} = \max \left( 2\rho\sigma_{\omega 2} \frac{1}{\omega} \frac{\partial k}{\partial x_j} \frac{\partial \omega}{\partial x_j}; 10^{-20} \right) \tag{2.44}$$

The turbulent dynamic viscosity  $\mu_T$  with numerical limiter to improve the Boussinisq approximation and consider the shear transport in the SST model.

$$\nu_T = \frac{a_1 k}{\max(a_1 \omega; \Omega F_2)} \tag{2.45}$$

The second blend function is given as follows

$$F_2 = \tanh(\text{arg}_2^2), \text{arg}_2 = \max \left( 2 \frac{\sqrt{k}}{0,09\omega y}; \frac{500\nu}{y^2\omega} \right) \tag{2.46}$$

The constants  $\emptyset$  in the  $k$ - $\omega$  SST model are calculated with the constants  $\emptyset_1$  and  $\emptyset_2$

$$\Phi = F_1\Phi_1 + (1 - F_2)\Phi_2 \quad (2.47)$$

The constants in the first set is chosen as  $\sigma_{k1} = 0.85, \sigma_{\omega1} = 0.85, \beta_1 = 0.075, \alpha_1 = 0.31, \beta^* = 0.09, k = 0.41, \gamma_1 = \frac{\beta_1}{\beta^*} - \sigma_{\omega1} \frac{k^2}{\sqrt{\beta^*}}$ , while the constant  $\Phi_2$  corresponds to the second set and are given by  $\sigma_{k2} = 1, \sigma_{\omega2} = 0.856, \beta_2 = 0.0828, \beta^* = 0.09, k = 0.41, \gamma_2 = \frac{\beta_2}{\beta^*} - \sigma_{\omega2} \frac{k^2}{\sqrt{\beta^*}}$ .

## 2.5 Wall Treatments

The majority of time spent in a Computational Fluid Dynamics (CFD) projects is usually devoted to successfully generating a mesh for the domain, as noted by JINYUAN [53] allowing a compromise between the desired accuracy and solution cost. This time-consuming procedure is considered a bottleneck in the analysis. The preferred method for determining the most accurate mesh is to carry out test runs on different mesh sizes and configurations and match the converged numerical solution as closely as possible to experimental data, in what is termed the grid independence test. Turbulent flows are significantly affected by the presence of walls, where the viscosity-affected regions have large gradients in the solution variables and accurate presentation of these regions determines successful prediction of wall bounded flows, GERSIMOV [38] and SALIM [88]. The boundary layer can be numerically solved up the wall boundary if appropriate turbulence models are used, like the  $k-\epsilon$  low-Reynolds, the  $k-\epsilon$  or the  $k-\omega$  SST and the boundary layer can be numerically solved up the wall boundary and hence adequate boundary conditions have to be fixed at the wall boundary. As the wall approached the turbulent kinetic energy and its derivative tend to zero, and according to its transport equation  $\epsilon = \nu \frac{\partial^2 k}{\partial y^2}$  and by double integrating it we get  $\epsilon \rightarrow 2\nu k/y^2$ . If the dissipation frequency is rather employed in the turbulence model, its limit at wall is  $\omega \rightarrow \infty$  and its numerical implementation requires the use of a numerical limiter.

Very fine computational meshes near to the wall is required for the numerical resolution of the complete boundary layer, with  $y^+$  values around 1, incurring in high computational costs. The wall function can be an alternative to the full numerical solution of the boundary layer, if the solution of the boundary layer is not the main point of interest in the fluid flow problem being addressed. In many industrial applications, the wall function can be employed without negative effects on the simulated flow characteristics, and the wall function relies on the similitude law of the stable boundary layer for most part of the flow. If the dimensionless sublayer-scaled velocity,  $u^+$ , and distance,  $y^+$ , are used, the

velocity distribution in the boundary layer describes a constant pattern, as shown in Figure 2.2.

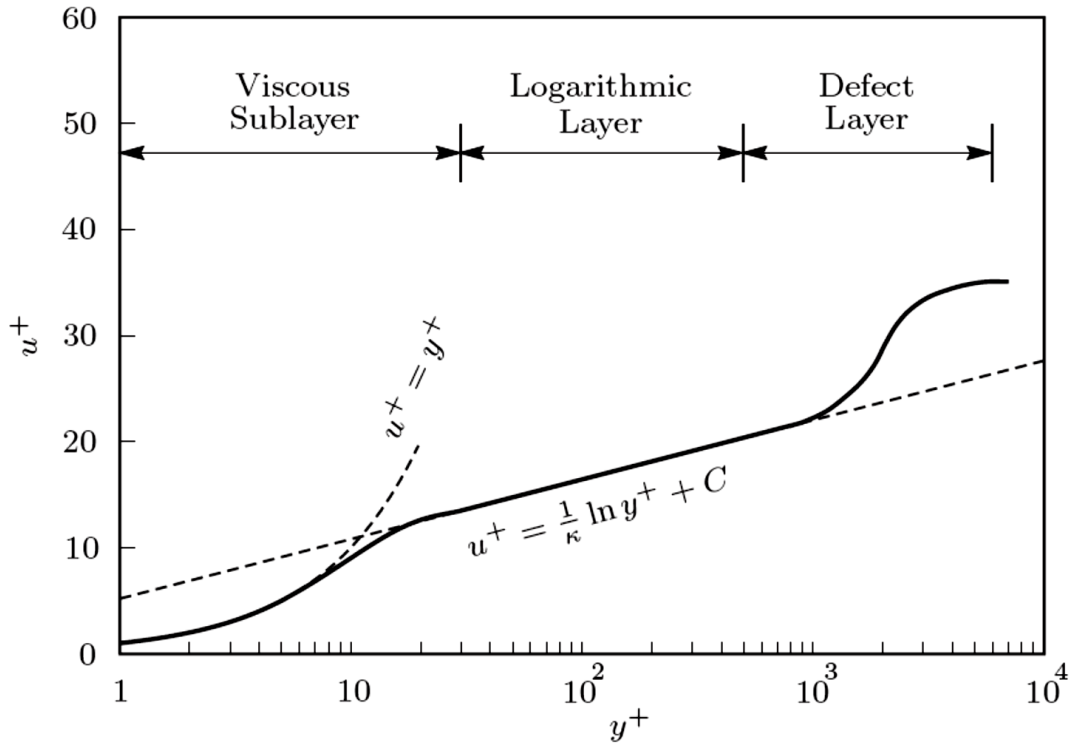


Figure 2.2: Typical velocity profile  $u^+(y^+)$  at the turbulent boundary layer, [106].

The sublayer-scaled velocity and distance are defined as follows:

$$y^+ = \frac{y u_\tau}{\nu}; \quad u^+ = \frac{u_t}{u_\tau} \quad (2.48)$$

Where  $u_t$  is the velocity component in the direction tangent to the wall and the friction velocity,  $u_\tau$  is defined with the shear stress at the wall  $\tau_w$

$$u_\tau = \sqrt{\frac{\tau_w}{\rho}} \quad (2.49)$$

The boundary layer can be divided in the viscous sub-layer, the logarithmic layer and the defect layer. In the viscous sub-layer, the sublayer-scaled velocity is equal to the sublayer-scaled distance,  $u^+ = y^+$ , as shown in the figure 2.2. In the logarithmic region, they are related by the following law:

$$u^+ = \frac{1}{k} \ln y^+ + C \quad (2.50)$$



According to WILCOX [106] the logarithmic layer goes typically from  $y^+ = 30$  until  $y^+ = 0.1\delta$ , where  $\delta$  is the thickness of the boundary layer. The von Karman constant  $k$  is 0.41 and the constant  $C$  depends on the surface roughness and for the smooth surface is 5.2. The distance between the first mesh point and the wall,  $y^2$ , has to produce  $y^+$  values in the range mentioned above, when the wall function is employed. Sometime a full numerical solution is inevitable despite the cost, especially when the boundary layer is highly unstable and the separation is massively present. In our case the wall function, automatic and scalable, can be applied with a good accuracy if the design was sufficiently adequate.

## 2.6 Effects of Compressibility

Introducing an equation for conservation of energy and an equation of state, for flows in which compressibility effects are an issue, is necessary. Just as Reynolds averaging gives rise to the Reynolds-stress tensor, we expect that similar averaging will lead to a turbulent heat-flux vector. It is also expected that new compressibility related correlations will appear throughout the equations of motion. These are important issues that must be addressed in constructing a turbulence model suitable for application to compressible flows, which can be expected to apply to constant property (low speed) flows with heat transfer [106].

Common observations pertaining to compressible turbulence, the Favre mass-averaging procedure and derive the mass-averaged equations of motion have to be accomplished. Developing a turbulence model for the compressible mixing layer and then followed with an application of perturbation methods to the compressible log layer, then apply several models to attached compressible boundary layers, including effects of pressure gradient, surface cooling and surface roughness, are all important issues in modeling a compressible turbulence flow [35].

By definition, a compressible flow is one in which significant density changes occur, even when pressure changes are small. It includes low-speed flow with large heat transfer rate. Models for high speed flows seem to fit the limited data quite well, perhaps with the expectation of combusting flow. Generally speaking, compressibility has a relatively small effect on turbulent eddies in wall-bounded flows. This appears to be true for Mach numbers up to about 5, provided the flow doesn't experience large pressure changes over a short distance such as we might have across a shock wave. At subsonic speeds, compressibility effects on eddies are usually unimportant for boundary layers provided. Based on these observations, Morkovin hypothesized that the effect of density fluctuations on the turbulence are small provided they remain small relative to the mean density. This is a major simplification for the turbulence modeler because it means that, in practice, one needs only account for the non-uniform mean density in computing compressible, shock-free, non-hypersonic turbulent flows.

There are limitations to the applicability of Morkovin's hypothesis even at non-hypersonic Mach numbers. For example, because the fluctuated density to the average density is typically not small, it applies neither to flows with significant heat transfer nor to flows with combustion. Also, because density fluctuations generally are much larger in free shear flows, models based on Morkovin's hypothesis fail to predict the measured reduction in spreading rate with increasing free-stream Mach number for the compressible mixing layer. The level of the fluctuation to the average density for a boundary layer at Mach 5 is comparable to the level found in a mixing layer at Mach 1. However, in addition, there seem to be qualitative changes in mixing layer structure as Mach number increases [106].

## 2.7 Favre Averaging

When we deal with compressible fluid medium, we will be having density and temperature fluctuation addition to the velocity and pressure fluctuation. So, using the common time-averaging procedure will produce new terms that has no analogs in the laminar equations [106]. We will first consider the conservation of mass where the instantaneous velocity is written as the sum of the mean value and the fluctuation density value

$$\rho = \bar{\rho} + \rho' \quad (2.51)$$

And by treating the instantaneous velocity in the usual way into the continuity equation yields

$$\frac{\partial}{\partial t}(\bar{\rho} + \rho') + \frac{\partial}{\partial x_i}(\bar{\rho} U_i + \rho' U_i + \bar{\rho} u'_i + \rho' u'_i) = 0 \quad (2.52)$$

And by taking the time averaging to the above equation we get the Reynolds-averaged continuity equation for compressible flow, which is sometimes referred to as the primitive-variable form of the continuity equation

$$\frac{\partial \bar{\rho}}{\partial t} + \frac{\partial}{\partial x_i}(\bar{\rho} U_i + \overline{\rho' u'_i}) = 0 \quad (2.53)$$

To achieve the closure, an approximation for the correlation between the fluctuation part of the density and the velocity has to be found. For the momentum equation the problem

is ever more complex where the Reynolds-stress tensor produced from the time averaging of the  $\rho u_i, u_j$ , and it is clear that we will be having a triple correlation involving  $\rho', u'_i$  and  $u'_j$ .

Favre suggested a mass-averaged for the velocity  $\tilde{u}_i$ , which is a density-weighted averaging procedure.

$$\tilde{u}_i = \frac{1}{\bar{\rho}} \lim_{T \rightarrow \infty} \int_t^{t+T} \rho(X, \tau) u_i(X, \tau) d\tau \quad (2.54)$$

So that the equation 4.42 can be rewritten

$$\frac{\partial \bar{\rho}}{\partial t} + \frac{\partial}{\partial x_i} (\bar{\rho} \tilde{u}_i) = 0 \quad (2.55)$$

And in terms of conventional of Reynolds averaging we have

$$\bar{\rho} \tilde{u}_i = \overline{\rho u_i} \quad (2.56)$$

The value of the above averaging known as the Reynolds averaging, and we can get also the following

$$\bar{\rho} \tilde{u}_i = \bar{\rho} U_i + \overline{\rho' u'_i} \quad (2.57)$$

Actually what we've done is treating the momentum per unit volume  $\rho u_i$  as an independent variable rather than the velocity i.e the rate of change of momentum per unit volume and not the velocity is equal to the sum of the imposed forces per unit volume in the flow, and that is a sensible thing from the physical point of view.

When Favre Average used, the usual decomposition for the instantaneous velocity into a mass averaged part  $\tilde{u}_i$  and fluctuation part  $u''_i$  i.e.

$$u_i = \tilde{u}_i + u''_i \quad (2.58)$$

After multiplying the equation 2.44 by  $\rho$  and taking the time average we will get the Favre average as follow

$$\overline{\rho u_i} = \bar{\rho} \tilde{u}_i + \overline{\rho' u''_i} \quad (2.59)$$

And after a tedious procedures and performing the conventional Reynolds average we find

$$\bar{u}_i'' = -\frac{\overline{\rho u_i'}}{\bar{\rho}} \quad (2.60)$$

The clear point after proceeding the Favre averaging is that the averaging is a mathematical simplification rather than a physical one, and this has to be born in mind.

## 2.8 Favre Average Equations

The equations governing the mass, momentum and heat, have to be solved when we deal with motion for a compressible flow medium. The instantaneous equations are as follows

$$\frac{\partial \rho}{\partial t} + \frac{\partial}{\partial x_i}(\rho u_i) = 0 \quad (2.61)$$

$$\frac{\partial}{\partial t}(\rho u_i) + \frac{\partial}{\partial x_j}(\rho u_i u_j) = -\frac{\partial p}{\partial x_i} + \frac{\partial t_{ij}}{\partial x_j} \quad (2.62)$$

$$\frac{\partial}{\partial t} \left[ \rho \left( e + \frac{1}{2} u_i u_j \right) \right] + \frac{\partial}{\partial x_j} \left[ \rho u_j \left( h + \frac{1}{2} u_i u_j \right) \right] = \frac{\partial}{\partial x_j} (u_i t_{ij}) - \frac{\partial q_j}{\partial x_j} \quad (2.63)$$

For the compressible flow the tensor  $t_{ij}$  involves the second viscosity  $\zeta$  as well as the conventional molecular viscosity  $\mu$ .

We will be eventually in need of defining the equation of state for the compressible fluid, and for gases the perfect gas law so that the pressure, density and temperature are related.

$$P = \rho RT \quad (2.64)$$

The relation between the stress and strain rate for the Newtonian fluid is

$$t_{ij} = 2\mu s_{ij} + \zeta \frac{\partial u_k}{\partial x_k} \delta_{ij} \quad (2.65)$$

The Fourier law is used to get the heat flux

$$q_j = -k \frac{\partial T}{\partial x_j} \quad (2.66)$$

For the sake of simplification we will relate the second viscosity to the molecular viscosity  $\mu$

$$\zeta = -\frac{2}{3} \mu \quad (2.67)$$

This assumption is correct for the monatomic gases and is generally used in all gases in standard CFD applications [106]. By assuming this we guarantee that the  $t_{ii} = 0$  and thus the viscous stresses don't contribute in the pressure even when  $s_{ii} = \frac{\partial u_i}{\partial x_i} \neq 0$ . The second assumption is that the fluid is calorically perfect i.e the specific heat coefficients are constants, this is just for the sake of simplification but actually the specific heat coefficients are not constant and we will deal with as they are not constants.

$$q_j = -k \frac{\partial T}{\partial x_j} = -\frac{\mu}{Pr_L} \frac{\partial h}{\partial x_j} \quad (2.68)$$

The laminar Prandtl number  $Pr_L$  is defined by

$$Pr_L = \frac{C_P \mu}{k} \quad (2.69)$$

To mass average the conservation equations, we decompose the various flow properties as follow

$$\left. \begin{aligned} u_i &= \tilde{u}_i + u_i'' \\ \rho &= \bar{\rho} + \rho' \\ p &= P + p' \\ h &= \tilde{h} + h'' \\ e &= \tilde{e} + e'' \\ T &= \tilde{T} + T'' \\ q_j &= q_{Lj} + q_{Lj}'' \end{aligned} \right\} \quad (2.70)$$

It is clear that decomposing flow properties  $p$ ,  $\rho$  and  $q_j$  is in terms of conventional mean value and the fluctuation part. And by substituting these parts in the equations of mass, momentum and energy conservation we get what is generally call the Favre (mass) averaged mean conservation equations.

$$\frac{\partial \bar{\rho}}{\partial t} + \frac{\partial}{\partial x_i} (\bar{\rho} \tilde{u}_i) = 0 \quad (2.71)$$

$$\frac{\partial}{\partial t} (\bar{\rho} \tilde{u}_i) + \frac{\partial}{\partial x_j} (\bar{\rho} \tilde{u}_j \tilde{u}_i) = -\frac{\partial P}{\partial x_i} + \frac{\partial}{\partial x_j} [\bar{t}_{ij} - \overline{\rho u_j'' u_i''}] \quad (2.72)$$

$$\begin{aligned}
\frac{\partial}{\partial t} \left[ \left( \bar{\rho} \left( \tilde{\epsilon} + \frac{\tilde{u}_i \tilde{u}_i}{2} \right) + \frac{\overline{\rho u_i'' u_i''}}{2} \right) + \frac{\partial}{\partial x_j} \left[ \bar{\rho} \tilde{u}_j \left( \tilde{h} + \frac{\tilde{u}_i \tilde{u}_i}{2} \right) + \tilde{u}_j \frac{\overline{\rho u_i'' u_i''}}{2} \right] \right] \\
= \frac{\partial}{\partial x_j} \left[ -q_{Lj} - \overline{\rho u_j'' h''} + \overline{\tau_{ij} u_i''} - \overline{\rho u_j'' \frac{1}{2} u_i'' u_i''} \right] \\
+ \frac{\partial}{\partial x_j} \left[ \tilde{u}_j (\overline{\tau_{ij}} - \overline{\rho u_i'' u_j''}) \right]
\end{aligned} \tag{2.73}$$

$$P = \bar{\rho} R \tilde{T} \tag{2.74}$$

It is easy to notice that the term of the Favre-averaged Reynold-stress tensor appear,  $\bar{\rho} \tau_{ij} = \overline{\rho u_i'' u_j''}$ , and here is to say that the tensor  $\tau_{ij}$  is symmetric.

The equation (2.62) represents the sum of internal energy, mean-flow kinetic energy and turbulence kinetic energy of the Favre-averaged mean energy equation for total energy. It is also obvious that this equation has many terms of an identifiable physical property. Where the double correlation between  $u_i''$  which is the kinetic energy per unit volume for the turbulent fluctuations. The correlation between  $u_j''$  and  $h''$  refers to the turbulent transport of heat. On the right hand side of the equation we find the two terms  $\overline{\tau_{ij} u_i''}$  and  $\overline{\rho u_j'' \frac{1}{2} u_i'' u_i''}$  correspond to the molecular diffusion and the turbulent transport of the turbulence kinetic energy, respectively [106]. These terms arise because the mass averaged total enthalpy appearing in the convective term of Equation (2.62) is the sum of mass-averaged enthalpy, mean kinetic energy and turbulence kinetic energy. They represent transfers between mean energy and turbulence kinetic energy that naturally arise when we derive the Favre-averaged turbulence kinetic energy equation. We can derive equation for  $k$  simply by multiplying the equation (2.42) by  $u_i''$  and time average.

$$\overline{\rho u_i'' \frac{\partial u_i}{\partial t}} + \overline{\rho u_i'' u_j \frac{\partial u_i}{\partial x_j}} = - \overline{u_i'' \frac{\partial p}{\partial x_i}} + \overline{u_i'' \frac{\partial \tau_{ij}}{\partial x_j}} \tag{2.75}$$

Carrying out the time averaging is done by proceeding term by term and using the tensor notation for the al derivatives i.e. proceeding from the left to the right and starting with the unsteady term and the convective term then with the pressure-gradient term and finally the viscous term at the far right end of the equation (2.64) and substituting all the result into the equation above. By doing this we arrive the Favre-averaged turbulent kinetic equation and by using the Favre-averaged continuity equation to rewrite the unsteady and the convective terms in the non-conservative form. The exact equation will be a follows

$$\begin{aligned}
\bar{\rho} \frac{\partial k}{\partial t} + \bar{\rho} \tilde{u}_j \frac{\partial k}{\partial x_j} &= \bar{\rho} \tau_{ij} \frac{\partial \tilde{u}_i}{\partial x_j} - t_{ij} \frac{\partial \overline{u_i''}}{\partial x_j} \\
&+ \frac{\partial}{\partial x_j} \left[ \overline{t_{ij} u_i''} - \overline{\rho u_j'' \frac{1}{2} u_i'' u_i''} - \overline{p' u_j''} \right] - \overline{u_i''} \frac{\partial p}{\partial x_i} + \overline{p' \frac{\partial u_i''}{\partial x_i}}
\end{aligned} \tag{2.76}$$

The last two terms are called the pressure work and the pressure dilatation, respectively.

Comparing the mean energy Equation (2.62) with the turbulence kinetic energy Equation (2.65), we see that indeed the two terms,  $\overline{t_{ij} u_i''}$  and  $\overline{\rho u_j'' \frac{1}{2} u_i'' u_i''}$  on the right-hand side of the mean-energy equation are Molecular Diffusion and Turbulent Transport of turbulence kinetic energy [32]. We can notice that the turbulence kinetic energy equation also indicates that the Favre-averaged dissipation rate is given by

$$\bar{\rho} \epsilon = \overline{t_{ij} \frac{\partial u_i''}{\partial x_j}} = \frac{1}{2} t_{ij} \left( \frac{\partial u_i''}{\partial x_j} + \frac{\partial u_j''}{\partial x_i} \right) = \overline{t_{ij} s_{ij}''} \tag{2.77}$$

One can easily derive an incompressible equation form from the equation (2.65), where the last two terms will vanish in the limit of the incompressible flow with zero density fluctuation. The pressure work vanishes because the time average of the  $u_i''$  is zero when the density fluctuation is zero and similarly the pressure dilatation term vanishes as the fluctuation field has zero divergence for the incompressible flow.

We can derive the Favre-averaged Reynolds-stress equation by assuming the following

$$\begin{aligned}
\frac{\partial}{\partial t} (\bar{\rho} \tau_{ij}) + \frac{\partial}{\partial x_k} (\bar{\rho} \tilde{u}_k \tau_{ij}) &= -\bar{\rho} \tau_{ik} \frac{\partial \tilde{u}_j}{\partial x_k} - \bar{\rho} \tau_{ik} \frac{\partial \tilde{u}_i}{\partial x_k} + \bar{\rho} \epsilon_{ij} - \bar{\rho} \Pi_{ij} \\
&+ \frac{\partial}{\partial x_k} \left[ -(\overline{t_{kj} u_i''} + \overline{t_{ki} u_j''}) + \bar{\rho} C_{ijk} \right] + \overline{u_i''} \frac{\partial P}{\partial x_j} + \overline{u_j''} \frac{\partial P}{\partial x_i}
\end{aligned} \tag{2.78}$$

Where

$$\bar{\rho} \Pi_{ij} = \overline{p' \left( \frac{\partial u_i''}{\partial x_j} + \frac{\partial u_j''}{\partial x_i} \right)} \tag{2.79}$$

$$\bar{\rho} \epsilon_{ij} = \overline{t_{kj} \frac{\partial u_i''}{\partial x_k} + t_{ki} \frac{\partial u_j''}{\partial x_k}} \tag{2.80}$$

$$\bar{\rho} C_{ijk} = \overline{\rho u_i'' u_j'' u_k''} + \overline{p' u_i'' \delta_{jk}} + \overline{p' u_j'' \delta_{ik}} \quad (2.81)$$

Now we can summarize the Favre-averaged mean equations and turbulence kinetic energy equation in conservation form.

$$\frac{\partial \bar{\rho}}{\partial t} + \frac{\partial}{\partial x_i} (\bar{\rho} \tilde{u}_i) = 0 \quad (2.82)$$

$$\frac{\partial}{\partial t} (\bar{\rho} \tilde{u}_i) + \frac{\partial}{\partial x_j} (\bar{\rho} \tilde{u}_j \tilde{u}_i) = -\frac{\partial P}{\partial x_i} + \frac{\partial}{\partial x_j} [\bar{t}_{ij} - \bar{\rho} \tau_{ij}] \quad (2.83)$$

$$\begin{aligned} \frac{\partial}{\partial t} (\bar{\rho} E) + \frac{\partial}{\partial x_j} (\bar{\rho} \tilde{u}_j H) \\ = \frac{\partial}{\partial x_j} \left[ -q_{Lj} - q_{Tj} + \overline{t_{ji} u_i''} - \overline{\rho u_j'' \frac{1}{2} u_i'' u_i''} \right] \\ + \frac{\partial}{\partial x_j} [\tilde{u}_i (\bar{t}_{ij} + \bar{\rho} \tau_{ij})] \end{aligned} \quad (2.84)$$

$$\begin{aligned} \frac{\partial}{\partial t} (\bar{\rho} k) + \frac{\partial (\bar{\rho} \tilde{u}_j k)}{\partial x_j} \\ = \bar{\rho} \tau_{ij} \frac{\partial \tilde{u}_i}{\partial x_j} - \bar{\rho} \epsilon + \frac{\partial}{\partial x_j} \left[ \overline{t_{ij} u_i''} - \overline{\rho u_j'' \frac{1}{2} u_i'' u_i''} - \overline{p' u_j''} \right] \\ - \overline{u_i'' \frac{\partial P}{\partial x_i}} + \overline{p' \frac{\partial u_i''}{\partial x_i}} \end{aligned} \quad (2.85)$$

$$P = \bar{\rho} R \tilde{T} \quad (2.86)$$

The quantities E and H are the total energy and the total enthalpy, and include the kinetic energy of the fluctuating turbulent field

$$E = \tilde{e} + \frac{1}{2} \tilde{u}_i \tilde{u}_j + k \quad \text{and} \quad H = \tilde{h} + \frac{1}{2} \tilde{u}_i \tilde{u}_j + k \quad (2.87)$$



## 2.9 $k$ - $\omega$ Model for Compressible Flows

Since many of the compressible equations are done with the  $k$ - $\omega$  model, it is instructive to focus on its equations and the closure approximations used to derive it.

We will start with the mass conservation equation then the momentum equation and then the energy conservation equation and the relevant equations.

$$\frac{\partial \bar{\rho}}{\partial t} + \frac{\partial}{\partial x_i} (\bar{\rho} \tilde{u}_i) = 0 \quad (2.88)$$

$$\frac{\partial}{\partial t} (\bar{\rho} \tilde{u}_i) + \frac{\partial}{\partial x_j} (\bar{\rho} \tilde{u}_j \tilde{u}_i) = -\frac{\partial P}{\partial x_i} + \frac{\partial}{\partial x_j} [\bar{t}_{ij} - \bar{\rho} \tau_{ij}] \quad (2.89)$$

$$\begin{aligned} \frac{\partial}{\partial t} \left[ \left( \bar{\rho} \left( \bar{e} + \frac{\tilde{u}_i \tilde{u}_i}{2} + k \right) \right) \right] + \frac{\partial}{\partial x_j} \left[ \bar{\rho} \tilde{u}_j \left( \bar{h} + \frac{\tilde{u}_i \tilde{u}_i}{2} + k \right) \right] \\ = \frac{\partial}{\partial x_j} \left[ \left( \frac{\mu}{P_{rL}} + \frac{\mu_T}{P_{rT}} \right) \frac{\partial \bar{h}}{\partial x_j} + \left( \mu + \sigma^* \frac{\rho k}{\omega} \right) \frac{\partial k}{\partial x_j} \right] \\ + \frac{\partial}{\partial x_j} [\tilde{u}_i (\bar{t}_{ij} + \bar{\rho} \tau_{ij})] \end{aligned} \quad (2.90)$$

Reynolds-stress and molecular tensors

$$\bar{t}_{ij} = 2\mu \bar{S}_{ij}, \quad \bar{\rho} \tau_{ij} = 2\mu_T \bar{S}_{ij} - \frac{2}{3} \bar{\rho} k \delta_{ij}, \quad \bar{S}_{ij} = S_{ij} - \frac{1}{3} \frac{\partial \tilde{u}_k}{\partial x_k} \delta_{ij} \quad (2.91)$$

And for the eddy viscosity

$$\mu_T = \frac{\bar{\rho} k}{\bar{\omega}}, \quad \bar{\omega} = \max \left\{ \omega, C_{lim} \sqrt{\frac{2 \bar{S}_{ij} \bar{S}_{ij}}{\beta^*}} \right\}, \quad C_{lim} = \frac{7}{8} \quad (2.92)$$

$$\frac{\partial}{\partial t} (\bar{\rho} k) + \frac{\partial}{\partial x_j} (\bar{\rho} \tilde{u}_j k) = \bar{\rho} \tau_{ij} \frac{\partial \tilde{u}_i}{\partial x_j} - \beta^* \bar{\rho} k \omega + \frac{\partial}{\partial x_j} \left[ \left( \mu + \sigma^* \frac{\rho k}{\omega} \right) \frac{\partial k}{\partial x_j} \right] \quad (2.93)$$

$$\begin{aligned} \frac{\partial}{\partial t} (\bar{\rho} \omega) + \frac{\partial}{\partial x_j} (\bar{\rho} \tilde{u}_j \omega) \\ = \alpha \frac{\omega}{k} \bar{\rho} \tau_{ij} \frac{\partial \tilde{u}_i}{\partial x_j} - \beta \bar{\rho} \omega^2 + \sigma_d \frac{\bar{\rho}}{\omega} \frac{\partial k}{\partial x_j} \frac{\partial \omega}{\partial x_j} \\ + \frac{\partial}{\partial x_j} \left[ \left( \mu + \sigma \frac{\rho k}{\omega} \right) \frac{\partial \omega}{\partial x_j} \right] \end{aligned} \quad (2.94)$$

Closure coefficients

$$\alpha = \frac{13}{25}, \quad \beta = \beta^\circ f^\circ, \quad \beta^* = \frac{9}{100}, \quad \sigma = \frac{1}{2}, \quad \sigma^* = \frac{3}{5}, \quad \sigma_{do} = \frac{1}{8} \quad (2.95)$$

$$\beta^\circ = 0.0708, \quad P_{rr} = \frac{8}{9}, \quad \sigma_d = \begin{cases} 0, & \frac{\partial k}{\partial x_j} \frac{\partial \omega}{\partial x_j} \leq 0 \\ \sigma_{do}, & \frac{\partial k}{\partial x_j} \frac{\partial \omega}{\partial x_j} > 0 \end{cases} \quad (2.96)$$

$$f_\beta = \frac{1 + 85\chi_\omega}{1 + 100\chi_\omega}, \quad \chi_\omega = \frac{|\Omega_{ij}\Omega_{jk}\hat{S}_{ki}|}{(\beta^*\omega)^3}, \quad \hat{S}_{ki} = S_{ki} - \frac{1}{2} \frac{\partial \tilde{u}_m}{\partial x_m} \delta_{ki} \quad (2.97)$$

There are a couple points worthy to be mentioned regarding applying this equation for both compressible and incompressible flow, first is that the turbulent kinetic equation has no particular compressibility terms involving pressure work, diffusion or dilatation, second, the energy conservation ensures ensure conservation of the total energy which includes the kinetic energy of the turbulence. It is clear that the closure coefficients are identical to those appears in the incompressible k- $\omega$  model.

## 2.10 Compressible boundary layers

Although the boundary layer in the radial inflow turbine is almost not a serious problem where the flow is in the direction of the negative pressure gradient and the boundary later is normally thin and low energized and the separation is not an issue to care about. But the flow in the exhaust region or in the diffuser is of course in the positive pressure gradient and thus the boundary layer in this region is highly energized and the separation can happen under particular operation points, that's why studying the boundary layer in the turbine in general and giving a special care to the exhaust part is an inevitable task to be done.

For the constant-pressure, adiabatic-wall boundary layers and in the range of 5 Mach number, the most turbulence models are capable of providing a reasonable predictions. However, the adverse pressure is still anathema for the k- $\epsilon$  while presenting no major problem for the k- $\omega$  model. In the presence of heat transfer, nontrivial discrepancies from the measured values will the model predict.

The algebraic models Cebeci-Smith [95] and Baldwin-Lomax model [14] usually require no special compressibility corrections. The Cebeci-Smith model uses the velocity thickness  $\delta_v^*$  which is defined by the equation (2.84) below, and it is used for both compressible and incompressible flow

$$\delta_v^* = \int_0^{\delta} (1 - U/U_e) dy \quad (2.98)$$

The velocity thickness used in the above is different from the displacement thickness,  $\delta^*$ , which is defined for compressible flows as follows

$$\delta^* = \int_0^{\delta} \left(1 - \frac{\bar{\rho} \tilde{u}}{\bar{\rho}_e \tilde{u}_e}\right) dy \quad (2.99)$$

Maise and McDonalds have illustrated the main reason behind why is the algebraic models can be used for the compressible boundary layers without modifications. They used the most recent experimental data at that time for the compressible boundary layers and inferred the mixing length variation, and the analysis shows that for Mac up to 5.

One of the observations was that the velocity profile for adiabatic walls correlate with the incompressible profile when the Van Driest scaling used,

$$\frac{u^*}{U_\infty} = \frac{1}{A} \sin^{-1} \left( A \frac{\tilde{u}}{U_\infty} \right), \quad A^2 = \frac{\gamma - 1}{2} M_\infty^2 \left( \frac{\tilde{T}_\infty}{\tilde{T}_w} \right) \quad (2.100)$$

And the Van Diest scaling fails to correlate the compressible velocity profiling when heat in present also it says that the classical mixing length is independent of Mach number.

It has been also shown that the algebraic models are consistent with the Maise-McDonalds observations, and that has been done by using the singular perturbation methods. A lot of scientists and researchers have used the Cebeci-Smith model and the Baldwin-Lomax models and found a great agreement with the measurements when it's applied to the adiabatic walls but there will be a larger differences when it is applied to a surface with heat transfer.

In the two equations models the problem is even more complicated as the log-layer solution indicated that the length scale for the k- $\omega$  and the k- $\epsilon$  varies linearly with the distance from the surface and independent from the Mach number and the models can also predicts the Van Driest velocity thus it is consistent with two of the most impotent observations of Maise and McDonalds.

### 2.10.1 Shock-Induced Boundary-Layer Separation

The interaction between the boundary-layer and the shock wave is one of the most challenging CFD problems. Many researchers have tried to model this physical phenomena since 1960's, and since the time required to solve the Favre-averaged continuity, Navier-Stokes and energy-conservation equation at that time was quite long as the computer capacity at that time was relatively limited, the efforts were confined to algebraic models. Also, the best compressible-flow numerical algorithms of that era was the time-marching methods that required many thousands of time-steps to get the solution solved.

The first solution to the Favre-averaged Navier-Stokes equation has been obtained by WILCOX [106] in 1974, Wilcox has used an advanced turbulence model for shock-induced separation of boundary-layer. Six computations have been included in this CFD study, three for the reflection of an oblique shock from a flat plate and three for a flow into a compression corner. It has been shown that the two-equation turbulence models give a reasonably accurate description of the flowfield of an oblique shock reflection from a flat plate. The figure below shows a comparison between the computed and the measured pitot-pressure  $P_p$ .

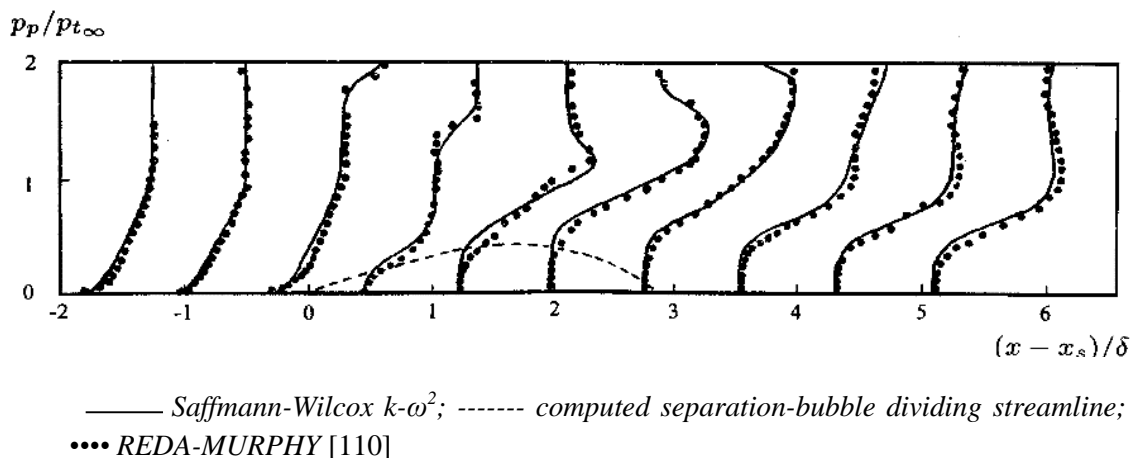


Figure 2.3: Computed and measured Pitot-pressure profile for Mach 3 shock-wave/boundary-layer interaction, [106].

The numerical flowfield for the other three computations i.e. for the compression corners, as in LAW [59] are differ significantly from the experimentally measured flowfield even though the Mach number, Reynolds number and the shock strength are identical to that of the fat-plate/shock boundary-layer flat-plate case [106]. What is worth being mentioned here is that the turbulence model used is the Saffman-Wilcox mode with surface boundary conditions given by matching the law of the wall, and the numerical algorithm used was first order accurate explicit time-marching procedure. Back then, the

limited computation capacity was an issue and made this calculations being done in a relatively long time and getting a steady-state conditions.

Later on, both computational methods and computing ability have been improved significantly, as many researchers have done an innovative work such as KNIGHT [56] and HORSTMANN [48] made, for example, using the two-equation model computation for shock-separated flow, possible within a very short CPU time.

### 2.10.2 The Use of Wall Function for Shock-Separated Flow

Reducing the CPU time is the primary motivation behind using the wall functions in the large scale computations that require usually substantial computer resources.

The most of the modern shock-separated computations have been done without using all functions although there is no evidence whatsoever that the law of the wall hold in separated regions and its use via wall functions is therefore a questionable approximation.

For the  $k-\omega$  model and following Wilcox 1989 we can derive the following compressible-flow wall function

$$\left. \begin{aligned} u^* &= u_\tau \left[ \frac{1}{k} \ln \left( \frac{u_\tau y}{v_w} \right) + C - 1.13 \frac{u_\tau y}{v_w} P^+ + O(P^+)^2 \right] \\ k &= \frac{\bar{\rho}_w}{\bar{\rho}} \frac{u_\tau^2}{\sqrt{\beta^*}} \left[ 1 + 1.16 \frac{u_\tau y}{v_w} P^+ + O(P^+)^2 \right] \\ \omega &= \sqrt{\frac{\bar{\rho}_w}{\bar{\rho}}} \frac{u_\tau}{\sqrt{\beta^*} ky} \left[ 1 - 0.30 \frac{u_\tau y}{v_w} P^+ + O(P^+)^2 \right] \end{aligned} \right\} \quad (2.101)$$

Where

$$P^+ = \frac{v_w}{\rho u_\tau^3} \frac{dP}{dx} \quad (2.102)$$

Very little sensitivity of the placement to the grid point closest to the surface or at  $y^+$  below 100, has been shown after using the above wall function with the  $k-\omega$  model.



## 3 Finite Volume Method (FVM) for CFD

### 3.1 Introduction

The finite volume method is a discretization method which is well suited for the numerical simulation of various types (elliptic, parabolic or hyperbolic, for instance) of conservation laws, it has been extensively used in several engineering fields, such as fluid mechanics, heat and mass transfer or petroleum engineering.

Some of the important features of the finite volume method are similar to those of the finite element method. It may be used on arbitrary geometries, using structured or unstructured meshes, and it leads to robust schemes. An additional feature is the local conservativity of the numerical fluxes that is the numerical flux is conserved from one discretization cell to its neighbor. This last feature makes the finite volume method quite attractive when modelling problems for which the flux is of importance, such as in fluid mechanics and heat and mass transfer. The finite volume method is locally conservative because it is based on a “balance” approach: a local balance is written on each discretization cell which is often called “control volume”; by the divergence formula, an integral formulation of the fluxes over the boundary of the control volume is then obtained. The fluxes on the boundary are discretized with respect to the discrete unknowns.

The FV approach is easy to understand and program as the all terms that need to be approximated have a physical meaning, and that’s why it is so popular among the engineers.

The disadvantage of this method is that it will be more difficult to be developed for the 3D after the second order, this is due to the fact that the FVM requires three levels of approximation which is interpolation, differentiation and integration [65].

### 3.2 FVM for diffusion problem

A numerical method based on the integration form of the control volume govern the transport equation of the fluid flow and the heat transfer has been developed, the Finite Volume (control volume) Method, and by considering a pure diffusion in the steady state, which is the simplest transport process at all, the governing equation of the steady pure diffusion process can easily be derived from the general transport equation for the property  $\phi$  by deleting the convection and the transient terms.

The general governing equation will be:

$$\text{div}(\Gamma \text{ grad } \phi) + S_\phi = 0 \quad (3.1)$$

The control volume integration which forms the key steps of the finite volume method that distinguishes it from all other CFD techniques yields the following form:

$$\int_{CV} \text{div}(\Gamma \text{ grad } \phi) dV + \int_{CV} S_\phi dV = \int_A n \cdot (\Gamma \text{ grad } \phi) dA + \int_{CV} S_\phi dV \quad (3.2)$$

$$= 0$$

Steady state diffusion in a three-dimensional situation is governed by

$$\frac{\partial}{\partial x} \left[ \Gamma \frac{\partial \phi}{\partial x} \right] + \frac{\partial}{\partial y} \left[ \Gamma \frac{\partial \phi}{\partial y} \right] + \frac{\partial}{\partial z} \left[ \Gamma \frac{\partial \phi}{\partial z} \right] + S_\phi = 0 \quad (3.3)$$

Now, a three dimensional grid is used to subdivide the domain. A typical control volume is shown in the figure (3.1) below:



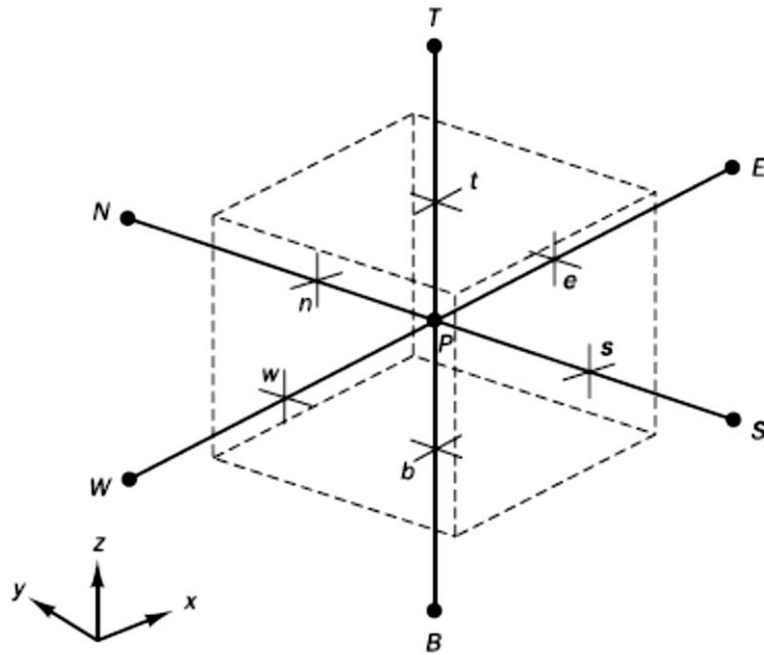


Figure 3.1 Three dimensional cell and neighboring nodes.

A cell containing node P has six neighboring nodes identified as west, east, south, north, bottom and top (W, E, S, N, B and T). Were, the notion w, e, s, n, b and t is used to refer to the west, east, south, north, bottom and top cell faces respectively [65].

Integration of equation (3.4) over the control volume shown gives,

$$\begin{aligned} & \left[ \Gamma_e A_e \left( \frac{\partial \phi}{\partial x} \right)_e - \Gamma_w A_w \left( \frac{\partial \phi}{\partial x} \right)_w \right] + \left[ \Gamma_n A_n \left( \frac{\partial \phi}{\partial y} \right)_n - \Gamma_s A_s \left( \frac{\partial \phi}{\partial y} \right)_s \right] \\ & + \left[ \Gamma_t A_t \left( \frac{\partial \phi}{\partial z} \right)_t - \Gamma_b A_b \left( \frac{\partial \phi}{\partial z} \right)_b \right] + \bar{S} \Delta V = 0 \end{aligned} \quad (3.4)$$

The equation above can be developed to a discretized form, as below,

$$\begin{aligned}
 & \left[ \Gamma_e A_e \frac{(\phi_E - \phi_P)}{\delta_{x PE}} - \Gamma_w A_w \frac{(\phi_P - \phi_W)}{\delta_{x WP}} \right] \\
 & + \left[ \Gamma_n A_n \frac{(\phi_N - \phi_P)}{\delta_{y PN}} - \Gamma_s A_s \frac{(\phi_P - \phi_S)}{\delta_{y SP}} \right] \\
 & + \left[ \Gamma_t A_t \frac{(\phi_T - \phi_P)}{\delta_{z PT}} - \Gamma_b A_b \frac{(\phi_P - \phi_b)}{\delta_{z BP}} \right] \\
 & + (S_u + S_P \phi_P) = 0
 \end{aligned} \tag{3.5}$$

The above equation can be rearranged to give the discretized equation for the entire nodes:

$$a_P \phi_P = a_w \phi_w + a_E \phi_E + a_S \phi_S + a_N \phi_N + a_B \phi_B + a_T \phi_T + S_u \tag{3.6}$$

Where:

$a_w$	$a_E$	$a_S$	$a_N$	$a_B$	$a_T$	$a_P$
$\frac{\Gamma_w A_w}{\delta_{x WP}}$	$\frac{\Gamma_e A_e}{\delta_{x PE}}$	$\frac{\Gamma_s A_s}{\delta_{y SP}}$	$\frac{\Gamma_n A_n}{\delta_{y PN}}$	$\frac{\Gamma_b A_b}{\delta_{z BP}}$	$\frac{\Gamma_t A_t}{\delta_{z PT}}$	$a_w + a_E + a_S + a_N + a_B + a_T - S_P$

The boundary conditions can be introduced by cutting links with the appropriate face(s) and modifying the source term accordingly.

### 3.3 FVM for Convection Problem

The effect of the convection has to be taken into consideration in the problems where the fluid flow plays a role. In nature, the convection always occurs alongside with the diffusion, so a method of predicting combined convection and diffusion is examined.

The steady convection-diffusion equation can be derived from the transport equation for a general property  $\phi$  by deleting the transient term.

$$\text{div}(\rho \mathbf{u} \phi) = \text{div}(\Gamma \text{grad} \phi) + S\phi \tag{3.7}$$

The integration over the control volume

$$\int_A \mathbf{n} \cdot (\rho \mathbf{u} \phi) dA = \int_A \mathbf{n} \cdot (\Gamma \text{grad} \phi) dA + \int_{CV} S_\phi dV \tag{3.8}$$

The equation represent the flux balance in a control volume, where, the net convection flux is given in the left hand side whether the right hand side gives the net diffusive flux and the generation or the destruction of the property  $\phi$  within the control volume.

The principal problem in the discretization of the convective terms is that the calculation of the value of transported property  $\phi$  at control volume faces and its convective flux across these boundaries. The central differencing method of obtaining discretized equations for the diffusion and source terms on the right hand side of equation has been introduced. It would seem obvious to try out this practice, which worked so well for diffusion problems, on the convective terms. However, the diffusion process affects the distribution of a transported quantity along its gradients in all directions, whereas convection spreads influence only in the flow direction. This crucial difference manifests itself in a stringent upper limit to the grid size, which is dependent on the relative strength of convection and diffusion, for stable convection– diffusion calculations with central differencing [65].

The central differencing scheme CDS has been used to represent the diffusion, and it seems logical to try linear interpolation to compute the cell face values for the convective terms on the left hand side of this equation.

One of the properties of the CDS is that it doesn't recognize the direction of the flow and the strength of the diffusion relative to the convection and also doesn't possess transportiveness at high Peclet numbers and it is stable and accurate only at Peclet number less than 2. In the Upwind Differencing Scheme UDS, the diffusion term still discretized using piecewise linear profile and if the flow is not aligned with the grid lines, false diffusion will be produced. Many interpolation methods have been developed to overcome the limitation of the UDS and the CDS. The quadratic upwind interpolation scheme QUICK form is one of them LEONARD [60] which doesn't offer a significant advantage over the other schemes. High-order-interpolation schemes, which involve more neighbor cells, acceptable convergence but lower robustness than the UDS, have been summarized by SKODA [94] like SMART from GASKELL AND LAU [37], MINMOND by HARTEN [44] and OSHER by CHAKRAVARTHY AND OSHER [21].

Other schemes like the Exponential Scheme, which is accurate for any Peclet number for the 1-D steady convection-diffusion but it is not accurate for the 2,3-D and it is computationally so expensive. The Hybrid Scheme which combines the advantage of both UDS and CDS where it is identical to the CDS for  $-2 \leq P_e \leq 2$  and it reduces to UDS with zero diffusion outside this range, but it still a first order accuracy in term of Tylor series.

### 3.4 Properties of discretization schemes

In theory numerical results may be obtained that are indistinguishable from the ‘exact’ solution of the transport equation when the number of computational cells is infinitely large, irrespective of the differencing method used. However, in practical calculations we can only use a finite – sometimes quite small – number of cells, and our numerical results will only be physically realistic when the discretization scheme has certain fundamental properties. The most important ones are the conservativeness, boundedness and transportiveness.

#### 3.4.1 Conservativeness

Integration of the convection–diffusion equation over a finite number of control volumes yields a set of discretized conservation equations involving fluxes of the transported property  $\phi$  through control volume faces [65]. To ensure conservation of  $\phi$  for the whole solution domain the flux of  $\phi$  leaving a control volume across a certain face must be equal to the flux of  $\phi$  entering the adjacent control volume through the same face. To achieve this, the flux through a common face must be represented in a consistent manner by one and the same expression in adjacent control volumes. Inconsistent flux interpolation formula gives rise to unsuitable schemes that do not satisfy overall conservation.

#### 3.4.2 Boundedness

The discretized equations at each nodal point represent a set of algebraic equations that needs to be solved. Normally iterative numerical techniques are used to solve large equation sets. These methods start the solution process from a guessed distribution of the variable  $\phi$  and perform successive updates until a converged solution is obtained. It has shown that a sufficient condition for a convergent iterative method can be expressed in terms of the values of the coefficients of the discretized equations:

$$\frac{\sum |a_{nb}|}{|a'_p|} \quad (3.9)$$

Here  $a'_p$  is the net coefficient of the central node, and the summation in the numerator is taken over all the neighboring nodes (nb). If the differencing scheme produces coefficients that satisfy the above criterion the resulting matrix of coefficients is diagonally dominant. To achieve diagonal dominance we need large values of net coefficient  $a_{p-S_p}$  so the linearization practice of source terms should ensure that  $S_p$  is always negative. If this is the case  $-S_p$  is always positive and adds to  $a_p$ . Diagonal dominance is a desirable feature for satisfying the ‘boundedness’ criterion. This states

that in the absence of sources the internal nodal values of property  $\phi$  should be bounded by its boundary values.

### 3.4.3 Transportiveness

The transportiveness property of a fluid flow can be illustrated by considering the effect at a point P due to two constant sources of  $\phi$  at nearby points W and E on either side as shown in Figure below. We define the non-dimensional cell Peclet number as a measure of the relative strengths of convection and diffusion:

$$Pe = \frac{F}{D} = \frac{\rho u}{\Gamma/\delta x} \quad (3.10)$$

Where  $\delta x$  is the characteristic length (cell width)

The lines in the figure below indicate the general shape of contours of constant  $\phi$  (say  $\phi = 1$ ) due to both sources for different values of Pe. The value of  $\phi$  at any point can be thought of as the sum of contributions due to the two sources.

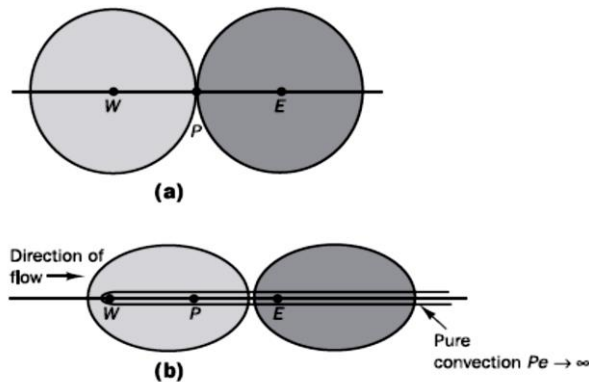


Figure 3.2 Distribution of  $\phi$  in the vicinity of two sources at different Peclet numbers, [65].

Let us consider two extreme cases to identify the extent of the influence at node P due to the sources at W and E:

- No convection and pure diffusion ( $Pe \rightarrow 0$ ).
- No diffusion and pure convection ( $Pe \rightarrow \infty$ ).

In the case of pure diffusion the fluid is stagnant ( $Pe \rightarrow 0$ ) and the contours of constant  $\phi$  will be concentric circles centered on W and E since the diffusion process tends to spread  $\phi$  equally in all directions. Figure 5.9a shows that both  $\phi = 1$  contours pass through P,

indicating that conditions at this point are influenced by both sources at W and E. As  $Pe$  increases the contours change shape from circular to elliptical and are shifted in the direction of the flow as shown in Figure (3.2). Influencing becomes increasingly biased towards the upstream direction at large values of  $Pe$ , so, in the present case where the flow is in the positive  $x$ -direction, conditions at P will be mainly influenced by the upstream source at W. In the case of pure convection ( $Pe \rightarrow \infty$ ) the elliptical contours are completely stretched out in the flow direction. All of property  $\phi$  emanating from the sources at W and E is immediately transported downstream. Thus, conditions at P are now unaffected by the downstream source at E and completely dictated by the upstream source at W. Since there is no diffusion  $\phi_p$  is equal to  $\phi_W$ . If the flow is in the negative  $x$ -direction we would find that  $\phi_p$  is equal to  $\phi_E$ . It is very important that the relationship between the directionality of influencing and the flow direction and magnitude of the Peclet number, known as the transportiveness, is borne out in the discretization scheme.

### 3.5 The upwind differencing scheme.

One of the major inadequacies of the central differencing scheme is its inability to identify flow direction. The value of property  $\phi$  at a west cell face is always influenced by both  $\phi_P$  and  $\phi_W$  in central differencing. In a strongly convective flow from west to east, the above treatment is unsuitable because the west cell face should receive much stronger influencing from node W than from node P. The upwind differencing or ‘donor cell’ differencing scheme takes into account the flow direction when determining the value at a cell face: the convected value of  $\phi$  at a cell face is taken to be equal to the value at the upstream node. In Figure (3.4) we show the nodal values used to calculate cell face values when the flow is in the positive direction (west to east) and in Figure (3.3) those for the negative direction.

Figure 3.3 The Upwind Differencing Scheme in the Positive Direction, [65]

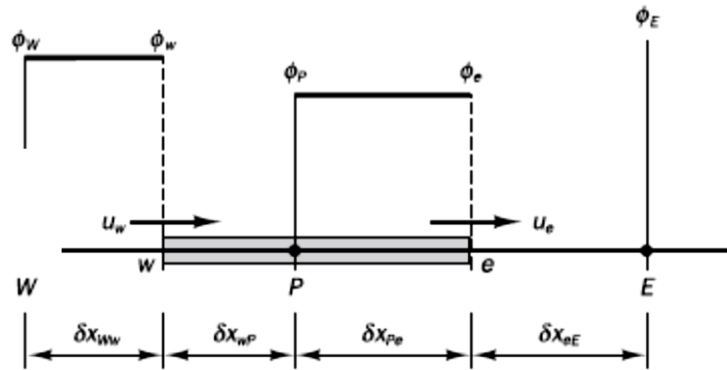
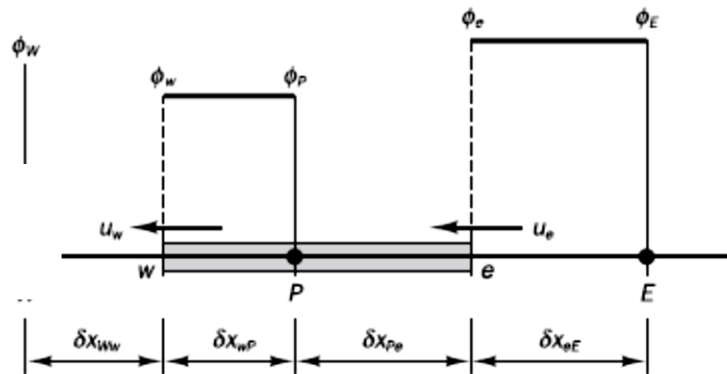


Figure 3.4 The Upwind Differencing Scheme in the Negative Direction, [65]



When the flow is in the positive direction,  $u_w > 0$ ,  $u_e > 0$  ( $F_w > 0$ ,  $F_e > 0$ ) and When the flow is in the negative direction,  $u_w < 0$ ,  $u_e < 0$  ( $F_w < 0$ ,  $F_e < 0$ ).

### 3.6 The Hybrid differencing

The hybrid differencing scheme of SPALDIN [97] is based on a combination of central and upwind differencing schemes. The central differencing scheme, which is second-order accurate, is employed for small Peclet numbers ( $Pe < 2$ ) and the upwind scheme, which is first-order accurate but accounts for transportiveness, is employed for large Peclet numbers ( $Pe \geq 2$ ). The hybrid differencing scheme uses piecewise formulae based on the local Peclet number to evaluate the net flux through each control volume face.

### 3.7 Discretization of Instationary Term

The coordinate of time has to be considered in the unsteady flows computation. Like the other three space coordinates the time must be discretized. The solution methods are essentially step by step. The conservation equation can be rewritten including the unsteady term, the convection, the diffusive flux and the source term, and as follows

$$\frac{\partial(\rho\phi)}{\partial t} = -div(\rho\phi v) + div(\Gamma grad \phi) + q_\phi = f(t, \phi(t)) \quad (3.11)$$

The second-order implicit Euler method has been chosen to be used, which is accurate in term of taking the information from the previous two time steps for the current time step. The instationary term can be approached as follows

$$\int_v \frac{\partial(\rho\phi)}{\partial t} dv \approx \frac{3(\rho\phi_P)^m - 4(\rho\phi_P)^{m-1} + (\rho\phi_P)^{m-2}}{2\Delta t} \quad (3.12)$$

The superscripts  $m$ ,  $m-1$  and  $m-2$  correspond to the two previous time steps and the current one.

It is clear that the values of the transport variable used in the convection, the diffusive flux and the source terms, is  $\phi^m$  and thus the method is fully implicit. The terms  $\phi^{m-1}$  and  $\phi^{m-2}$  are added to the vector in the metrical equation.

There are other methods like the explicit method, Crank-Nicolson Method mentioned in CRANK-NICOLSON [27] and Three Time Level method mentioned in REGAL [79].

### 3.8 Boundary Conditions

To solve the mathematical system, boundary conditions have to be applied at the borders of the control volume and these boundary conditions should reflect the physical conditions at the boundaries.

Mainly there are two methods of imposing the boundary conditions, the first is imposing the values of the variables at the boundary faces which is the so called Dirichlet boundary conditions. Also the boundary conditions can be imposed by specifying a fixed gradient at the boundary faces which is the so called von Neumann boundary conditions.

In the FVM the types of the boundary conditions are basically, inlet, outlet, walls, symmetry and periodicity. The conservation of the scalar and the vectorial fluxes has to be ensured fat the interfaces of the multi-blocks computational domains. There are different possible combinations of the boundary conditions, and below the most common and numerically stable ones.



### 3.8.1 Inlet and Outlet Boundary Conditions

In most cases, the values of the velocity components at the inlet is either given or can be directly calculated.

As we implement a compressible working fluid, the pressure gradient is also imposed, where the pressure correction is given  $U'_{i, in} = U_{ci} P'_{in}$ , this for the case of subsonic flow. For the case of supersonic flows, the pressure is specified at the inlet using Dirichlet instead of Neumann boundary conditions, and hence the pressure correction becomes zero as its value is explicitly specified.

Since the internal energy transport equation for the compressible flows has to be solved, the value of the temperature  $T$  has to be specified at the inlet cell faces. Normally, the value of the kinetic energy  $K$  is prescribed at the inlet face based on the turbulence intensity. Typically, the value of the turbulence intensity is being between 1% and 20% and it is known from the experiments or its influence on the numerical simulation is tested.

Fixed value of the turbulence dissipation  $\epsilon$ , using an estimation based on the kinetic energy and the characteristic length. The characteristic length is specific for each case.

The values of the turbulence dissipation frequency,  $\omega$ , for the case of the turbulence models derived from  $k-\omega$ , can be computed from  $\epsilon$ .

At the outlet domain, the components of the velocity distribution make a part of the problem unknowns. Therefore, a constant velocity gradient is imposed at the outlet leading to extrapolate the values of the domain interior to the outlet boundary

$$U_{i,out} = U_{i,P} + \lambda_{out}(U_{i,P} - U_{i,Q}) \quad (3.13)$$

The parameter  $\lambda_{out}$  is the extrapolation factor and is derived from the distance between the cell centers and the boundary.

$$\lambda_{out} = \frac{|X_{pq} - X_p|}{|X_Q - X_{pq}| - |X_{pq} - X_p|} \quad (3.13)$$

The index  $Q$  makes reference to the center point of the cell neighboring the boundary cell, whose center is  $P$ .

In case of subsonic flow, the pressure at the outlet is set constant and the pressure correction  $P'$  set to zero. In the individual boundary cells the pressure level set to constant

$P_{const}$  or the pressure surface averaged at the outlet boundary,  $P_{PQ}$ , can be fixed. A blending for both conditions is also possible

$$p_{out} = \alpha_P P_{PQ} + (1 - \alpha_P) P_{const} \quad (3.14)$$

For the supersonic flow, the pressure value at the outlet can be also extrapolated from the domain interior values, corresponding to a constant gradient, as the outlet pressure is also a part from the solution.

### 3.8.2 Block Interface

Most of the problems are made up of more than one domain with different topology, and the fluid flows from one domain to the other. These domains may be stationary or rotating components or through different parts. Different meshing strategies are desired and the position of the grid nodes at both sides of the blocks interface may not exactly match, which is known as the non-matching interface, and this problem needs to be dealt with.

The non-matching in the turbomachines can take place between the rotor and the stator vanes or between the rotor and the exhaust nozzle, in both cases the non-matching is due to the relative motion, grid density, different blocking or the periodicity, the figure below shows a typical non-matching interface between two structural grids.

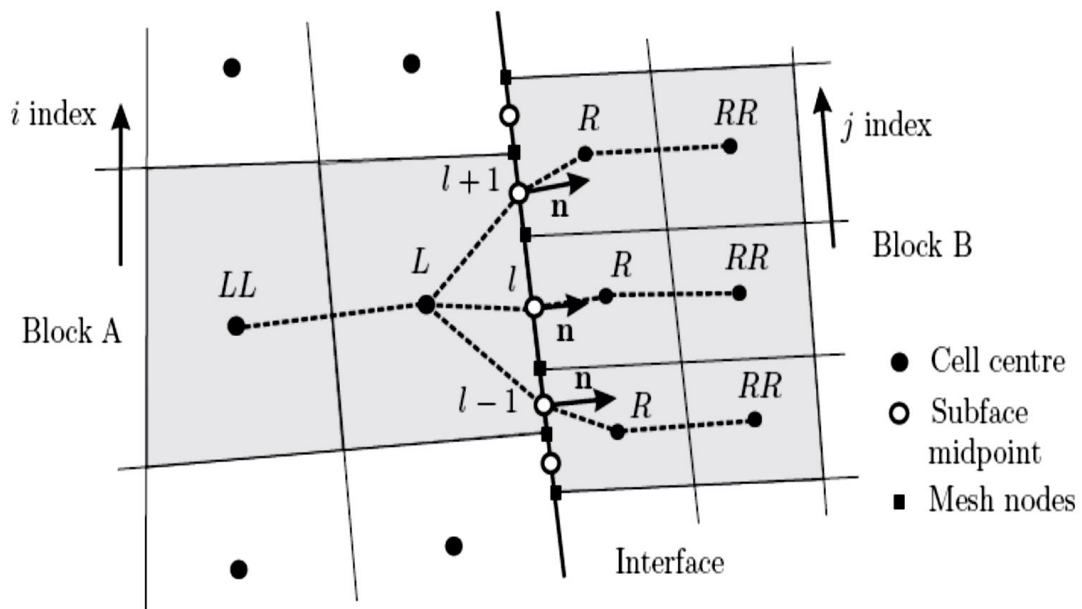


Figure 3. 5: Typical block interface with non-matching nodes.

LILEK ET AL [61] suggested a numerical procedure and implemented further by RIEDEL [83], consists in dividing the interface faces into surfaces, defined by intersection of the interface faces of one block with the edges of the other non-matching block and calculating the fluxes conservation with these subfaces [63].

The numerical method used for GGI (general grid interface) in CFX is that the control surface approach used to perform the connection across a GGI attachment or periodic condition. To have a full freedom to change the grid topology and the physical distribution across the interface, a physically based intersection algorithm has been employed. A general intersection algorithm permits connections to be successfully made even when the resultant surfaces on either side of an interface do not physically “fit” together to form a well-defined physical connection. In addition, an automatic surface trimming function is performed by the GGI algorithm, to account for mismatched surface extent [5]. This gives the ability for successful attachment even if the surface of one side of the interface is larger than the surface on the other side, where the intersection is constructed between the overlapped regions.

For the domains that rotate relative to one another the Multiple Frame of Reference MFR allow the analysis, which is appropriate for the cases focus on the rotor-stator interaction for rotating turbomachinery, and the MFR is actually a GGI base approach.

### 3.8.3 Wall Boundary Conditions

Considering an impermeable or non-porous walls where no mass flow in the wall normal direction and the convective flux at the wall flux disappeared. The velocity components at the wall velocity, due to the non-slip condition at the wall  $U_i = U_{i,w}$ . For the solution of the momentum equations at the wall cells, the diffusive flux is determined with the shear stress at the wall,  $\tau_w$ , and its direction. The derivation of the diffusive flux makes use of the wall local coordinate system,  $(n, t, \text{ and } b)$ , where  $n$  corresponds to the direction normal to the wall,  $t$  to the flow direction in the cell center point,  $P$ , and  $b$  completes the orthogonal system, being normal to the  $n$  and  $t$  directions.

The shear stress components can be directly evaluated with the local coordinate system aligned to the flow direction, where the shear stress is calculated with the velocity partial derivative.

$$\tau_{nn} = 2\mu \frac{\partial U_n}{\partial n} = 0, \tau_{nt} = 2\mu \frac{\partial U_t}{\partial n}, \tau_{nb} = 2\mu \frac{\partial U_b}{\partial n} = 0 \quad (3.15)$$

The normal vector,  $n_i$ , is known from the problem geometry, while the tangential vector,  $t_i$ , is only determined by the flow. In the third vector direction,  $b_i$ , no flow takes places,

$U_{b,p} = 0$ . The normal velocity component,  $U_{n,p}$ , is calculated with the scalar product  $U_{i,p} n_i$ . The tangential velocity vector,  $U_{i,t,p}$ , is obtained from the distance between the velocity vector,  $U_{i,p}$ , and the normal velocity vector,  $U_{i,n,p}$ .

$$U_{i,t,p} = U_{i,p} - U_{i,n,p} = U_{i,p} - (U_{j,p} U_j) n_i \quad (3.16)$$

The tangential direction vector.  $t_i$  for the tangential velocity vector  $U_{i,t,p}$  is evaluated as follows

$$t_i = \frac{U_{i,t,p}}{|U_{i,t,p}|} \quad (3.17)$$

As usual, the diffusive flux at the wall face is calculated with the shear stress in the flow direction and the integral is approximated by the midpoint rule. The diffusive flux at the wall, in the numerical implementation of the FVM is computed with differ correction, with the shear stress from the previous iteration in order to keep the matrix diagonal coefficient the same for all cells.

Neumann boundary conditions are imposed at the wall for both the pressure and the pressure correction term, and that leads to the extrapolation from the domain interior.

The value of the wall temperature can be fixed or the derivative of it can be imposed, which is equivalent to specify the wall heat flux  $q_w = -\lambda \left( \frac{\partial T}{\partial n} \right)_w$ .

The value of the derivative of the kinetic energy at the wall is also assumed to be zero, which leads to Dirichlet,  $K_w = 0$ , and Neumann,  $\left( \frac{\partial k}{\partial n} \right) = 0$ , boundary conditions.

The value of the dissipation is fixed at the wall boundary, for the turbulence models based on the kinetic energy  $k$  and the dissipation  $\epsilon$ . CHAPMAN AND KUHN [22] suggested an appropriate approximation

$$\epsilon_w^{k-\epsilon} = \nu \frac{4k_p}{y_p^2} - \epsilon_p \quad (3.18)$$

The wall function assumes that the first mesh point is inside the logarithmic region of the boundary layer, otherwise, the application is not valid, as in some case where a successive meshes need to be generated until satisfying the logarithmic conditions, or to employ a modified version of the wall function, as VIESER, ESCH AND MENTOR [57] have

done, where the law of the wall is blended with analytical expression of  $\omega$  near the wall for  $k$ - $\omega$  based turbulence model.

### 3.8.4 Free Slip

Symmetry boundary condition, Euler wall or the free slip wall, are incompressible, like the non-slip wall but the flow can slip freely at its surface without any frictional stress at the wall boundary. No mass flux crosses the wall and the diffusive flux accounts for the momentum conservation. It normally constitutes simplifications of physical aspects of the fluid flow [63].

### 3.8.5 Periodic Interface

The spatial periodicity is a characteristic of the cases where geometrical patterns are repeated in the computational domain. The blading channel of the turbomachines is the typical example of that.

For the simplicity of the periodic cases only one instance of the whole pattern can be simulated, so we can save much computational resources [63]. This simplification is acceptable for the stationary and homogenous flows. And since we simulate single periodic element, adequate boundary conditions have to be set at the interface where the next periodic element would be. At the periodic interface, the transport values have to be assumed to have the same value at the both sides of the interface.

## 3.9 The Pressure-Velocity Coupling

Discretizing the mass flow through a surface of the control volume must be done carefully to lead to a proper pressure-velocity coupling and to accurately handle the effect of compressibility. The CFD code we implement, uses a co-located or non-staggered grid layout such that the control system we use is identical for all transport equation, as mentioned in PATANKER [72] but the co-located method lead to a decoupled pressure field. An alternative discretization for the mass flow, has been introduced by RHI AND CHOW [81] to avoid the decoupling. MAJUMDAR [64] has modified this method to remove the dependence of the steady-state solution on the time step. In Ansys CFX, a similar strategy is adopted by applying a momentum-like equation to each integration point [4].

### 3.10 Solver

Solving the following algebraic system

$$A_p^\phi + \sum_l A_l^\phi \phi_l = Q_p^\phi \quad (3.19)$$

Where the matrix A contains the coefficients related to the variables, which are implicitly solved, as the independent vector Q contains the source term, the explicitly related variables and the differed correlations. We have the matrix coefficients  $A_p$  and  $A_l$  depend on the velocity components which are themselves unknowns, because of the non-linearity property of the transport equation. Thus, the solution of the system is divided into inner and outer iterations. The source terms and the matrix coefficients at a given iteration n, can be calculated with the previous values of n-1. Constant values of  $A_p$  and  $A_l$  are chosen for the processing of inner iterations, where the algebraic system is solved, and after that the values of the velocity and the density are updated with the new values and then the outer iteration begins. Convergence criteria are needed to decide when the outer and the inner loops to stop. The most common criteria are based on the sum-norm, maximum-norm and the root-mean-square RMS- norm of the residuum vector. When the residuum vector is chosen, a common convergence criteria can be applied where the value of the vector is smaller than a given value of  $\epsilon$ . To increase the stability and as the other procedures can be used and the under-relaxation is one of the common techniques. Reinforcing the matrix diagonal dominance for the impulse equation in the inner interaction, can also increase the convergence stability.

#### 3.10.1 The Segregated Solver and the Implicit Pressure Correction

An explicit treatment has been applied to the impulse equations, the pressure term, which means that it is included in the source term and its value is taken from previous solution iteration. So that, the impulse equation gives only a solution for the velocity components. To solve the pressure field, a coupling of pressure and the mass flow rate, by applying the equation of mass conservation, is needed, which is known as pressure correction method.

Making use of the staggered variables arrangement instead of the collected arrangement, is first introduced by PATANKAR [72] in the SIMPLE algorithm. DEMERDZIC ET AL [30] has extended the SIMPLE algorithm to be applied to the compressible fluids by proposing an approximation of the pressure and the pressure correlation. VAN DOORMAL AND RAITHNY [101] have modified it further with the SIMPLER algorithm or by ISSA [50] in the PISO algorithm, which is for the instationary problem or when large time steps.

### 3.10.2 Coupled Solver

The segregated solvers was the base of the first FVM codes but the recent ones are based also on the coupled solvers or just on the coupled solvers, as the coupled solvers make no use of the implicit pressure correction method but rely directly on the discretization of the original mass conservation equation. The unknown vector includes the pressure variable and it is no anymore treated explicitly but implicitly in the algebraic system and solved simultaneously with the velocity component. Generally, the solution procedure is the same of the staggered solver but the pressure and the velocity components and the mass flow don't need correction. Finally, the mass and impulse conservation are first solved then the energy conservation equation and then the turbulent transport equation and eventually the additional transport equation of the system [63].

### 3.10.3 Linear Solver

A multigrid accelerated Incomplete Lower Upper factorization technique for solving the discrete system of linearization equations has been used by the solver we applied.

It is an iterative solver, whereby the exact solution of the equation is approached during the course of several iteration [5]. A general matrix represent the linearized system of discrete equations

$$[A][\varphi][B] \quad (3.20)$$

by starting with an approximate solution  $\varphi^n$ , the above equation can be solved iteratively, which is to be improved by a correction  $\varphi'$  to yield a better solution

$$\varphi^{n+1} = \varphi^n + \varphi' \quad (3.21)$$

Where  $\varphi'$  is the solution of:

$$A\varphi' = r^n \quad (3.22)$$

With  $r^n$ , the residual obtained from

$$r^n = b - A\varphi^n \quad (3.23)$$

And by repeating the application for this algorithm will yield to the desired accuracy. Iterative solvers such as ILU tend to rapidly decrease in performance as the number of the computational mesh elements increases, and the performance also decrease if there a large aspect ratio [5]. The Strongly Implicit Decomposition behaves likewise.

Interactive methods like the Conjugate Gradient Square CGS or the Biconjugate Stabilized BCGSTAB are considerably faster and more stable as mentioned in PERIC [35].

By solving the algebraic system by distributing it over several computers or computer clusters which run in parallel, can also accelerate the computational speed, as mentioned by SKODA [94]. For the parallelization, the original computational mesh is divided, or partitioned, in several blocks, as if they were blocks with non-matching interfaces. The solution of each one of these blocks is assigned to one computer or core and the interface information, or interface fluxes, are exchanged between them. Mainly due to the data exchange between processing units, the performance increase is not a linear function of the number of processor or cores and is bound to a maximum.





# 4 Turbines Concepts and Configuration

## 4.1 Introduction

The automobile turbocharger is the best known use of the radial inflow turbines, but they also appear in the auxiliary power turbines and, for example, in the turboprop aircraft. They are used also in the geothermal energy production, in processing industries, including refineries, natural-gas processing, and air liquefaction. In the automotive application burned gases from the engine exhaust manifold are directed into a radial inflow turbine of the turbocharger, which powers a centrifugal compressor on the same axis. The compressor, in turn, increases the pressure and density of the supplied air to the engine. As the engine speed may change quite rapidly, turbochargers must respond to the changing operating conditions nimbly. Therefore they are made light in weight and low in inertia.

The main difference between the radial inflow turbine used in the turbocharger and the one proposed in our application is that the power available in the exhaust gases for the turbine in the turbocharger is much more than sufficient than the power demand to run the compressor and that's why the designer for this kind of applications doesn't really care about the efficiency and the optimum design. Therefore, we see that the turbine in the turbocharger is normally designed to be nozzleless, to gain some production cost and to produce it with a lower inertia. However, in our application and in the applications where the efficiency and designing the turbomachine at its optimum state, is a matter, more care has to be given to the design of the nozzle row and of course, for the other components.

In this chapter we introduce the main design procedures used in the up-to-date research development process. Then we'll go through defining the main parameters and constraints and the effect of each parameter on the turbine performance.

## 4.2 Aerodynamic design strategy

In the design procedures we shall address the basic stage component design, the nozzle and the rotor, the interstage or the vaneless annular passage will as well be dealt with, and inserted before and after the nozzle row. Specific aerodynamic and geometric calculations at stations located at the exit and inlet of all components, are required for component sizing.

It is conveniently used to specify the stage performance in term of total-to-static  $\eta_{t-s}$  performance to the rotor as shown in the equation 4.1, mentioned in AUNGIER [8]. Basically, the designer has to provide the stage inlet total temperature  $T_{t1}$ , the stage inlet total pressure,  $P_{t1}$ , the stage mass flow rate, the pressure ratio, the specific speed  $n_s$ , the velocity ratio  $v_s$ , the total-to-static efficiency  $\eta_{t-s}$  and the equation of state of the working fluid. The figure (4.1) below is a schematic represent in the station notations of the turbine used.

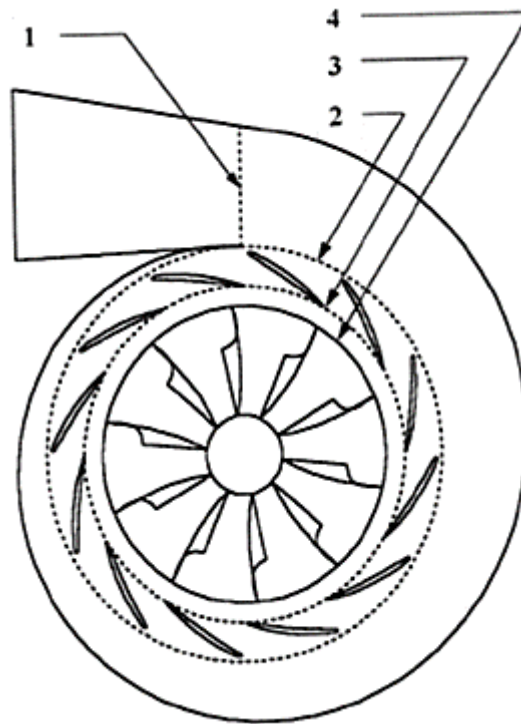


Figure 4.1: The station notations of the stage.

Where the  $\eta_{t-s}$  is defined as follows

$$\eta_{t-s} = \frac{h_{t1} - h_{t5}}{h_{t1} - h_5} \quad (4.1)$$

After BALJE [15] we define the specific speed in a dimensionless form as follows:

$$n_s = \frac{\omega \sqrt{Q_5}}{(\Delta H_{id})^{3/4}} \quad (4.2a)$$

Where the  $\Delta H_{id}$  is the ideal heat drop correspond to an isentropic expansion from the stage inlet total conditions to the rotor exit static pressure, and  $Q_5$  is the volume flow rate at the exit of the od the rotor and it is defined as the ratio of the mass flow rate to the rotor exit total density

$$Q_5 = \frac{\dot{m}}{\rho_{t5}} \quad (4.2b)$$

Selecting the values of the velocity ratio and the specific speed really determine the quality of the design, but the selection of the total-to-static efficiency is a consequence of these choices. General correlations have been proposed to help in the initial choice of these parameters. For the radial inflow turbine, there are already some correlations existed which have been introduced by many researchers, such as, WOOD [110], LINHAR [62] BALJE [15], CORDIER [26] and ROHLIK [85].

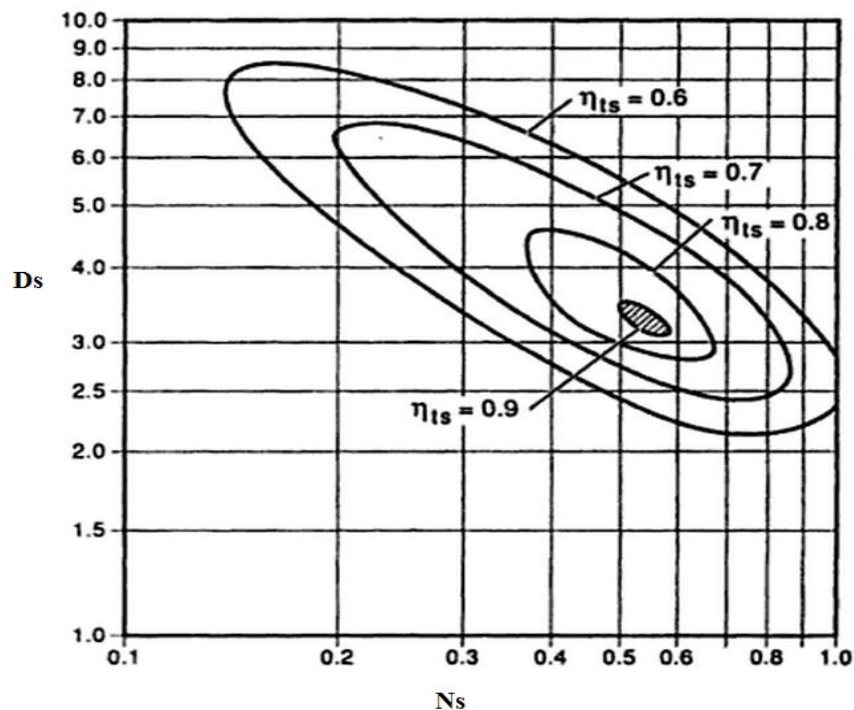


Figure 4.2: Balje Diagram for radial inflow turbines, [32].

Using extensive empirical data, CORDIER [26] carried out intensive empirical analysis of good turbomachines and attempted to correlate the data in term of specific speed,  $N_s$ ,

and the specific diameter  $D_s$ . This concept has been further improved by BALJE [15] and eventually plotted a graph correlates these two parameters, as shown in the figure (4.2) above.

Where the specific diameter defined as follows

$$D_s = \frac{D_4 (\Delta H_{id})^{1/4}}{\sqrt{Q_5}} \quad (4.3)$$

For the preliminary design system, a generalized stage performance chart, shown in figure (4.3), has been used to help in choosing the initial values. This chart is based on the work done by the researcher mentioned in the paragraph above. The preferred range for the specific speed, and as a general rule, can be taken between 0.45 -0.75, although we are not really free and sometimes we've to choose beyond this range of values due to some restrictions like mechanical integrity, Mach number and speed. And that's why the chart has been extended further.

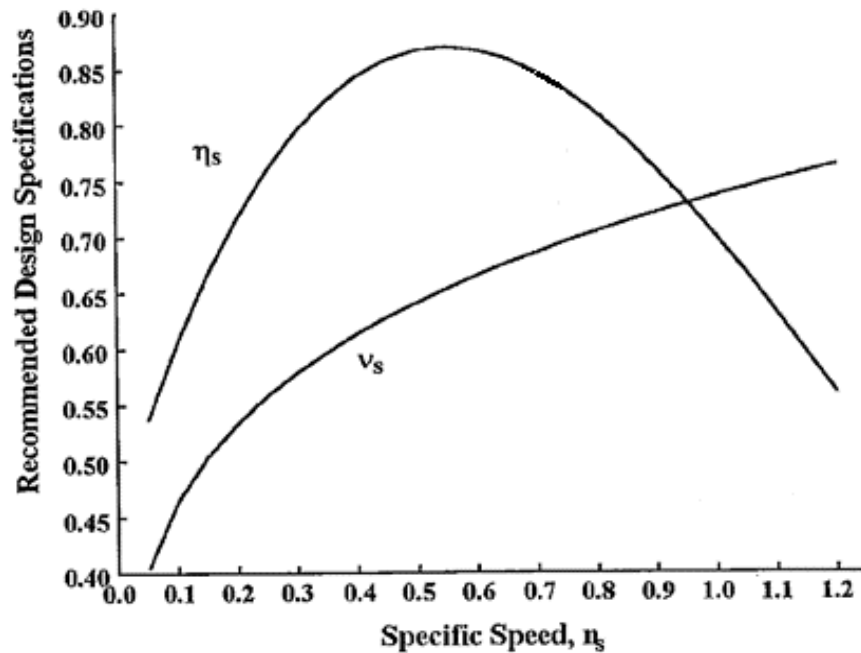


Figure 4.3: Balje diagram for a radial inflow turbine, [32].

The correlations which relates the values of the total-to-static efficiency, the speed ratio with the specific speed can also be presented to make use of it in choosing arbitrary values.

$$v_s = 0.737 n_s^{0.2} \quad (4.4)$$

$$\eta_{t-s} = 0.87 - 1.07(n_s - 0.55)^2 - 0.5 (n_s - 0.55)^3 \quad (4.5)$$

The performance analysis can be proceeded when we finished the preliminary design of the turbine, and improving the estimated values of the specific speed, the total-to-static efficiency and the velocity ratio.

To complete a well-matched and optimized stage components, the preliminary procedure is rather ineffective as it needs more parameters to be introduced, but it can be used as a candidate where the designer starts adjusting these parameters to reach an acceptable or even an optimum design point.

ROHLIK [85] showed a breakdown of the losses for each component of the radial inflow turbine, and as can be seen in the figure 4.4 below

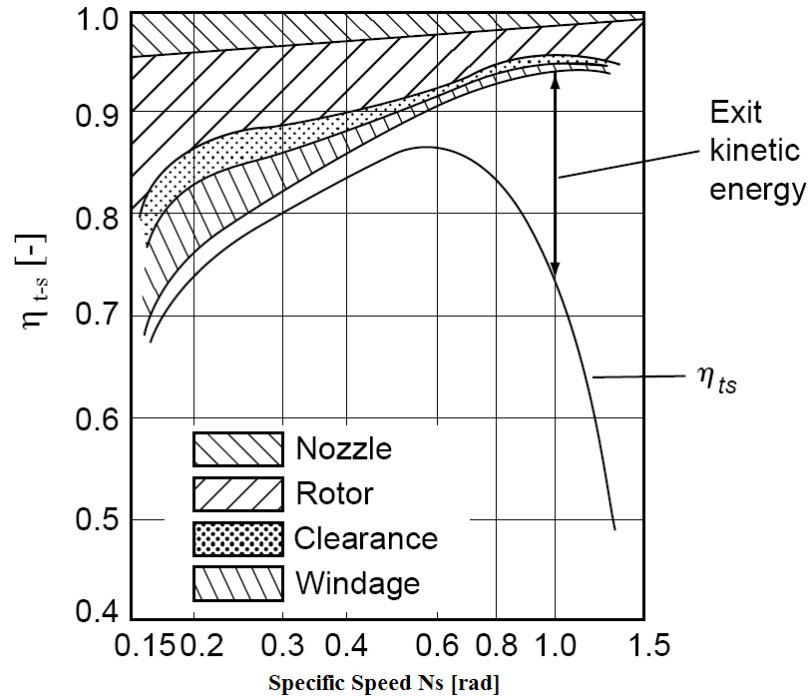


Figure 4.4: Distribution of losses along envelope of total to static efficiency, [85].

### 4.2.1 The flow and load coefficients

Defining the flow and the load coefficients enable the designer to describe the overall dimension of the machine so that assessment and comparison can be easily made. These parameters have been extensively used in the design of axial turbines and eventually also have been used to the same extent with the radial turbines. The blade speed in the radial turbine is widely varied due to the change in the radius between the inlet and exit, unlike in the axial turbines. The loading coefficient can be defined based on the rotor inlet speed

$$\psi = \frac{\Delta h_0}{U_4^2} = \frac{C_{\theta 4}}{U_4} - r \frac{C_{\theta 5}}{U_4} \quad (4.6)$$

Where  $r = \frac{r_{5s}}{r_4}$ , and  $C_{\theta 5}$  is the tangential component for the velocity at the exit of the rotor which is negligibly small compared to the  $U_4$  at the design point.

The flow coefficient is non-dimensionlized to the rotor inlet speed, and it is defined in term of the meridional velocity as follows

$$\varphi = \frac{C_{m4}}{U_4} \quad (4.7)$$

The power coefficient is also an important parameter and it is defined as the ratio of the produced power to the inlet total enthalpy and as follow

$$S_w = \frac{W}{\dot{m} h_{01}} \quad (4.8)$$

BAINES [11] has introduced a correlation between the flow and load coefficients with a contour of constant total to static efficiency, and as shown in the figure (4.5) below

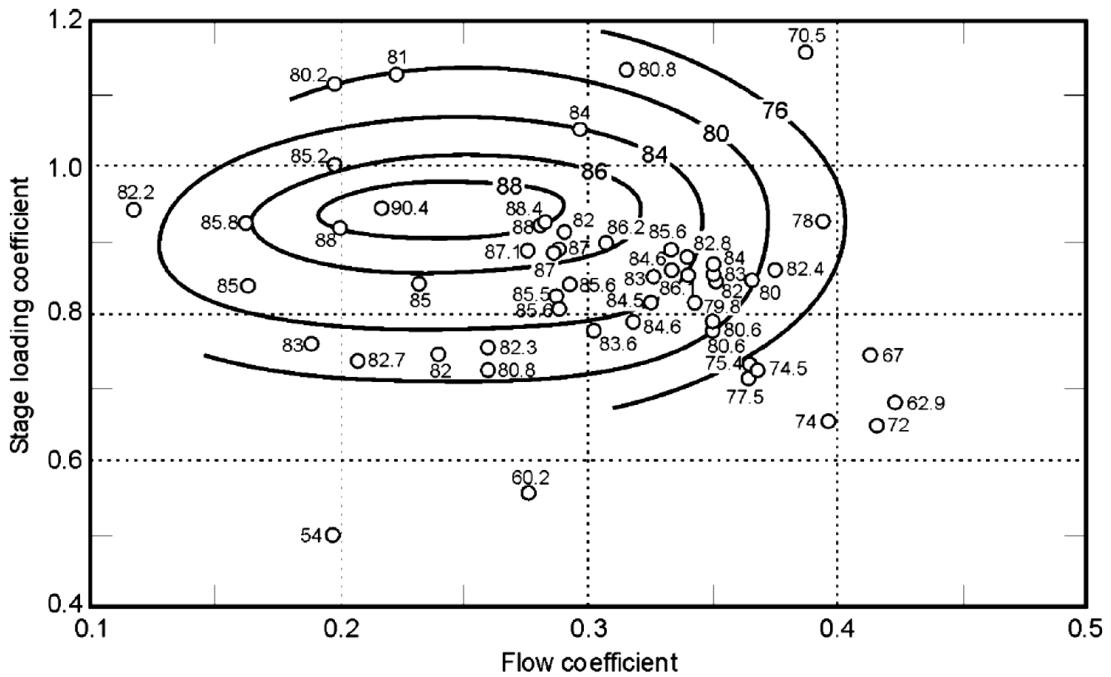


Figure 4.5: Correlation of measured efficiency of a range of turbine designs with stage loading and flow coefficients, [11].

From the figure above, the maximum efficiency occurs for the flow coefficient in the range of 0.2-0.3 and loading coefficient in the range of 0.7-0.9. We have started with combinations of values within these ranges.

#### 4.2.2 Aerodynamic Considerations of the Rotor Exit

The Mach number at the shroud has to be designed in a way not to reach unity to avoid an oblique or a normal shock wave from being happened. The blade height at the exit is also to be chosen sufficiently large to reduce the relative velocity. However, choosing the minimum exit Mach number begins by assuming the radial inflow turbines operates under conditions such that the absolute velocity at the exit of the rotor is axial, then the mass balance is to be written as follows.

$$\dot{m} = \rho_5 C_5 A_5 = \rho_5 C_5 \pi (r_{5s}^2 - r_{5h}^2) = \rho_5 C_5 \pi r_{5s}^2 (1 - k^2) \quad (4.9)$$

Where  $k = r_{5s}^2/r_{5h}^2$ , and then,

$$\dot{m} = \frac{P_5}{RT_5} M_5 \sqrt{\gamma RT_5} \pi r_{5s}^2 (1 - k^2) \quad (4.10)$$



A form of the flow coefficient as introduced in KORPELA [57] is as follows

$$\Phi = \frac{\dot{m}}{\rho_{o1} C_{o1} \pi r_2^2} = \frac{P_5}{P_{o1}} \left( \frac{T_{o1}}{T_5} \right)^{1/2} M_5 \frac{r_{5s}^2}{r_4^2} (1 - k^2) \quad (4.11)$$

Substituting  $\frac{U_{5s}^2}{U_2^2} = \frac{r_{5s}^2}{r_2^2}$  and dividing it through  $U_4^2$  in the equation above and by have  $W_{5s}^2 = C_5^2 + U_{5s}^2$  we get,

$$\Phi = \frac{P_5}{P_{o1}} \left( \frac{T_{o1}}{T_5} \right)^{1/2} M_5 \frac{M_{5Rs}^2 - M_5^2}{M_{ou}^2} (1 - k^2) \quad (4.12)$$

By solving it to the  $M_{5Rs}$

$$M_{5Rs}^2 = M_5^2 + \frac{\Phi M_{ou}^2}{(1 - k^2)} \frac{1}{M_5} \left( 1 + \frac{\gamma - 1}{2} M_5^2 \right)^{1/2} \left( \frac{P_5}{P_{o1}} \right) \left( \frac{T_{o1}}{T_{o5}} \right)^{1/2} \quad (4.13)$$

Where the pressure ratio and the stagnation temperature ratio are given as follow:

$$\frac{P_5}{P_{o1}} = \left( 1 - \frac{S_w}{\eta_{ts}} \right)^{-\gamma/(\gamma-1)} \quad \frac{T_{o1}}{T_{o5}} = \frac{1}{1 - S_w} \quad (4.14)$$

We can also define B as

$$B = \Phi_f \left( 1 - \frac{S_w}{\eta_{ts}} \right)^{-\gamma/(\gamma-1)} \frac{1}{1 - S_w} \quad (4.15)$$

Where

$$\Phi_f = \frac{\Phi_o M_{ou}^2}{(1 - k^2)} \quad (4.16)$$

The relative Mach number at the exit will be as follows:

$$M_{5RS}^2 = M_5^2 + B \left( \frac{1}{M_5^2} + \frac{\gamma - 1}{2} \right)^{1/2} \quad (4.17)$$

After differentiating the equation above and setting it equal to the zero, we get the minimum relative exit Mach number as follows:

$$M_{5RS} = \left[ M_5^2 + B \left( \frac{1}{M_5^2} + \frac{\gamma - 1}{2} \right)^{1/2} \right]^{1/2} \quad (4.18)$$

The figure below shows the minimum of  $M_{5RS}$  marked by small circles, and since we assumed that the velocity at the exit is axial, this follows:

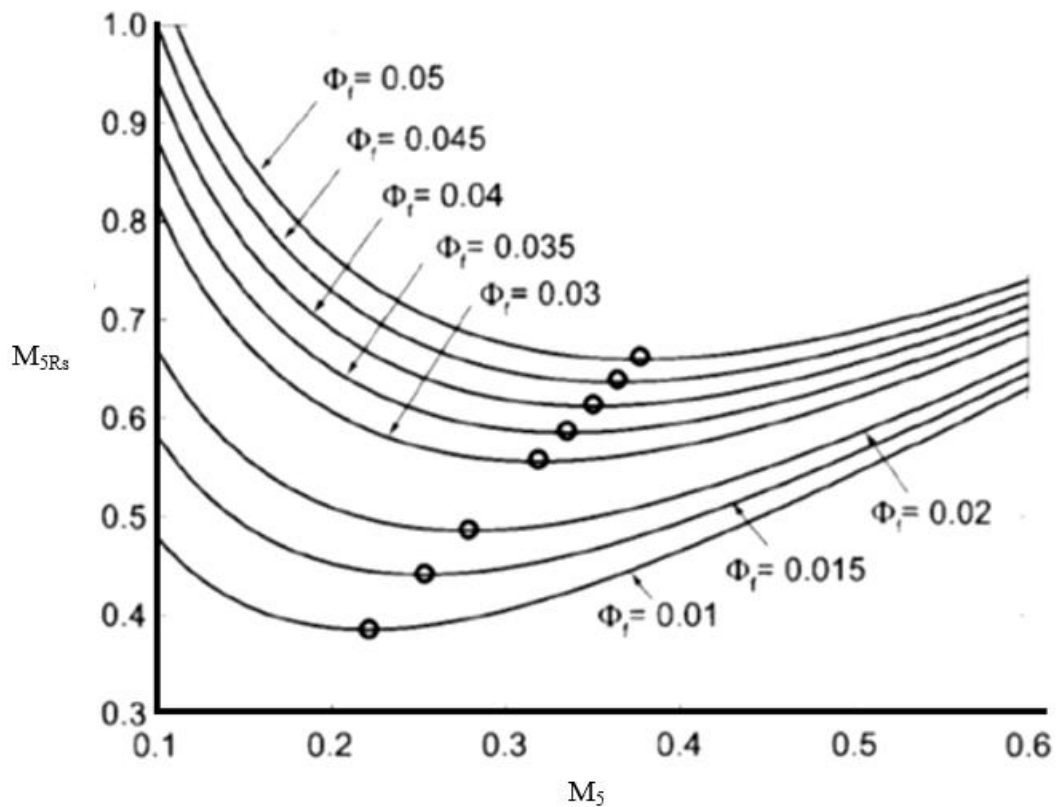


Figure 4.6: Relative Mach number  $M_{5R}$  as a function of Mach number  $M_5$ , with  $\Phi_f$  as a parameter. The pressure ratio is  $p_{01}/p_5 = 2$ , with  $\eta_{ts} = 0.85$  and  $\gamma = 1.4$ , [57]

$$\frac{M_5^2}{M_{5Rs}^2} = \frac{C_5}{W_{5s}} \cos \beta_{5s} \quad (4.19)$$

It's clear from the plotting that the minimum Mach number at the exit of the rotor occurs when the value of  $\beta_5 = -56^\circ$  for the pressure ratio of value 2 and  $\eta_{ts} = 85\%$ . These values can be deviate a little bit due to violating some other design constraints and to meet the mechanical and the manufactural integrity of the complete design.

ROHLIK [85] has suggested to the relative exit to the inlet velocity ratio  $W_5/W_4 = 2$ , which gives a good design from the rotor. And that for the shroud  $W_{5s}/W_4 = 2.5$ .

The ratio of the blade height to the rotor inlet diameter is also assumed to be in arrange of 0.5 – 1.5.

### 4.2.3 The Optimum Incidence Angle and the Blade Number

KORPELA [57] has suggested that the slip factor of the centrifugal compressor to be adopted, which is, as Sanitz reported, given as follows:

$$\sigma = \frac{C_{\theta 4}}{C'_{\theta 4}} \quad \text{with} \quad \sigma = 1 - \frac{0.63 \pi}{Z} \quad (4.20)$$

Where  $Z$  is the number of blades and  $C'_{\theta 4}$  is the tangential velocity component at the inlet of the rotor in the absence of the slip factor. For the radial blades  $C'_{\theta 4} = U_4$ . And that gives the following:

$$\frac{C_{\theta 4}}{U_4} = 1 - \frac{0.63 \pi}{Z} \quad (4.21)$$

We have also

$$C_{\theta 4} = U_4 + W_{\theta 4} = U_4 + W_{r4} \tan \beta_4 = U_4 + C_{\theta 4} \frac{\tan \beta_4}{\tan \alpha_4} \quad (4.22)$$

And that leads the ratio  $\frac{C_{\theta 4}}{U_4}$  to be as follows:

$$\frac{C_{\theta 4}}{U_4} = \frac{\tan \alpha_4}{\tan \alpha_4 - \tan \beta_4} \quad (4.23)$$

At the condition of minimum Mach number we have, (See appendix A),  $\alpha_4 = \pi/2 + \beta_4/2$ .

We get

$$\frac{C_{\theta 4}}{U_4} = \cos \beta_4 \quad (4.24)$$

We have also the number of blades related to the inlet relative flow angle  $\beta_4$

$$\cos \beta_4 = 1 - \frac{0.63 \pi}{Z} \quad (4.25)$$

KORPELA [57] suggested that if this angle corresponds to the optimum nozzle angle for a minimum Mach number at the entry, the substitution  $\beta_4 = 2 \alpha_4 - \pi$ , and the suggestion of WHITFIELD [104] leads to the formula of the optimum nozzle angle

$$\cos \beta_4 = \frac{1}{\sqrt{Z}} \quad (4.26)$$

The figure 4.7 shows the optimum angle along with the GLOSSMAN's [41] suggestions

$$Z = \frac{\pi}{3} (110 - \alpha_4) \tan \alpha_4 \quad (4.27)$$

AUNGIER [8] suggested also a correlation for the number of blades as function of the rotor inlet flow angle

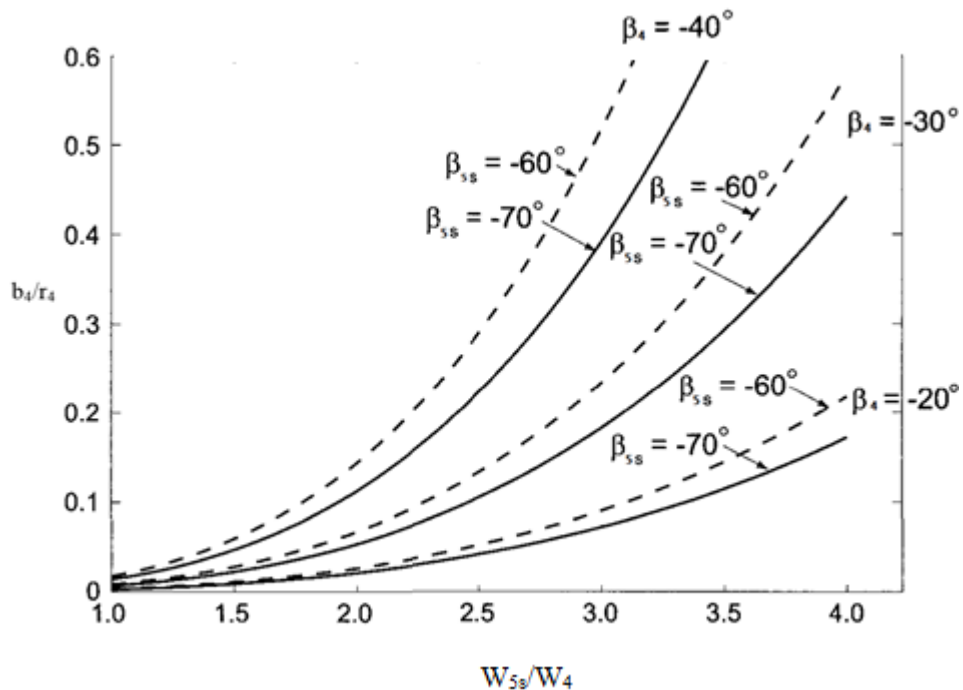


Figure 4.7: Blade width-to-radius ratio as a function of the relative velocity ratio  $W_{5s}/W_4$  for relative flow angles corresponding to minimum Mach number at the inlet and at axial exit. The pressure ratio is  $p_{05}/p_5 = 2$ , with  $\eta_{ts} = 0.85$ ,  $\gamma = 1.4$ , and the static enthalpy loss coefficient of the stator is  $\zeta_s = 0.15$ . The exit hub to shroud radius ratio is  $k = 0.2$ , [57].

## 4.3 Turbine Geometry

The researchers, ROHLIK [85], BALJE [15] and AUNGIER [8] have invested a lot of effort in outlining a unified methodology of approaching the optimum design geometry of a radial inflow turbine for a particular operating conditions. Therefore, turbine geometries have been examined in detail for calculated points on and near the curve of maximum static efficiency. To illustrate the change in optimum turbine shape with the application as represented by specific speed, several design parameters were then plotted as functions of specific speed.

Among these parameters, the optimum stator-exit angle, the ratio of the stator exit height to the rotor inlet diameter versus the specific speed have been plotted. The ratio of the exit tip diameter to the rotor inlet diameter has been also showed. The variation of the blade- speed ratio with the specific speed along the maximum static efficiency is also plotted by ROHLIK [85], and the nature of calculations was such that the ratio of the blade tip speed to the actual work is almost constant for the all points calculated, as the blade speed ratio includes ideal rather than actual work, and its variation reflex the variation in static efficiency in the turbine.

### 4.3.1 Radial-Inflow Turbine Rotor Sizing

After introducing the inlet total pressure and temperature, the mass flow rate and the pressure ration and with the aid of the equation of state, we can immediately calculate the static pressure at the exit of the rotor and the ideal enthalpy drop. The rotor tip blade speed and the discharge spouting velocity can be given as follows:

$$C_{os} = \sqrt{2 \Delta H_{id}} \quad (4.28)$$

$$U_4 = v_s C_{os} \quad (4.29)$$

And from the specified efficiency, the total enthalpy at the exit of the rotor can be calculated

$$H_5 = H_1 - \Delta H_{id} \eta_s \quad (4.30)$$

After AUNGIER [8] the discharge total density can be assumed, for the sake of, simplicity to be equal to the static density at the exit of the rotor. This assumption is true when the absolute velocity at the exit of the rotor is negligibly small otherwise, this value needs to

be corrected. The specific speed equation introduced by BALJE [15] can then be solved for the rotor speed  $\omega$ , and hence the rotor tip radius is defined

$$r_4 = \frac{U_4}{\omega} \quad (4.31)$$

The effect of the losses that occurs upstream the rotor influences the rotor tip sizing, and by estimating the isentropic enthalpy loss an estimate of the rotor inlet total pressure found to be as follows:

$$P_{t4} = P_{t1} - \rho_{t1} \Delta H_{id} (1 - \eta_s)/4 \quad (4.32)$$

For the calculations of the sizing the turbine at the optimum design point, it is assumed that the rotor exit tangential velocity equal to zero, in practice the value of it deviates a bit away from the zero, and then the inlet tangential velocity can be defined as follows:

$$C_{\theta 4} = U_4 \eta_s / (2v_s^2) \quad (4.33)$$

### 4.3.2 Radial-Inflow Turbine Design Specifications

AUNGIER [8] suggested the following design specifications to be effective and sufficient to complete the rotor design, which are, the inlet flow angle  $\alpha_4$ , the inlet blade thickness  $t_{b4}$ , the exit blade thickness  $t_{b5}$ , the exit hub radius  $r_{h5}$ , the exit shroud radius  $r_{s5}$ , the axial length  $L_R$ , the number of rotor blades  $N_R$ , the inlet blade angle  $\beta_4$ , and the impeller blade type, the latter considered either a straight-line-element or radial element blade which is preferred for our application and for the applications of high speed turbines, where the inlet blade is considered to be right angled i.e.  $90^\circ$

Default values considered to be a reasonable estimation and these values are to be subsequently revised. For the nozzle exit flow angle or the rotor inlet absolute angle ROHLIK [85] has recommended an equation which relates it to the specific speed and as follows:

$$\alpha_4 = 10.8 + 14.2 n_s^2 \quad (4.34)$$

A similar correlations have been suggested by AUNGIER [8] for the blade thickness and exit hub radius:

$$t_{b4} = 0.04 r_4 \quad (4.35)$$

$$t_{b5} = 0.02 r_4 \quad (4.36)$$

$$r_{h5} = 0.18 r_4 \quad (4.37)$$

The following procedure has been found to be effective in estimating values for exit shroud radius and the axial length which based on maintaining a reasonable ratio passage width-to-the flow path radius of curvature.

$$C_{m5}/C_{m4} = 1 + 5(b_4/r_4)^2 \quad (4.38)$$

From the mass balance and the values of  $C_{m4}$  and  $b_4$  with the assumption of  $C_{\theta 5}$  is zero, the value of  $r_{h5}$ , and similarly we can find the value of  $r_{s5}$  and then the axial length can be estimated as follows:

$$L_R = 1.5(r_{s5} - r_{h5}) \quad (4.39)$$

The correlation proposed by JAMIESON [52] has been modified by AUNGIER [8] and ROHLIK [85] to develop an empirical equation to estimate the optimum number of the turbine blades and as follows:

$$N_R = 12 + 0.03(33 - \alpha_4) \quad (4.40)$$

Where  $\alpha_4$  is measured from the tangent. It is clear the number of blades has to be rounded to get an integer value for the number of blade. It is also worth to be mentioned here that the estimation of the inlet blade angle is based on the operation at the optimum incidence angle and based in the slip factor model described by AUNGIER [8] and as the slip factor depends on the inlet blade angle, iteration is needed to converge on a correct blade angle of the turbine rotor inlet

The limiting radius ratio has been ignore form the sip factor model to get a simplified form of it, and that assumes avoiding the blade too short to be effective, and the this assumption can be checked in the performance analysis of the design procedures, hence the slip factor is being given as follows:

$$\sigma = 1 - \sqrt{\sin \beta_4} / N_R^{0.7} \quad (4.41)$$

$$K_{B4} = 1 - N_R t_{b4} / [2\pi r_4 \sin \beta_4] \quad (4.42)$$

$K_{B4}$  is the impeller blockage factor.

This parameter defines the fraction of the flow passage available for the through-flow inside the blade after correction for the blade metal blockage. AUNGIER [8] said that since the slip factor is defined based on the flow velocity inside the blade, and since the  $C_{m4}$  defines the outside flow velocity, the ideal tangential velocity inside the blades is approximated by assuming the gas density equal to its value outside the blades, and that means,

$$C_{\theta 4}^* = \sigma [U_4 - C_{m4} \frac{\cot \beta_4}{K_{B4}}] \quad (4.43)$$

Inside the blades, the ideal and the actual incidence angle can be defined as follows:

$$i_4^* = \beta_4 - 90^\circ + \tan^{-1} [ (U_4 - C_{\theta 4}^*) \frac{K_{B4}}{C_{m4}} ] \quad (4.44)$$

$$i_4 = \beta_4 - 90^\circ + \tan^{-1} [ (U_4 - C_{\theta 4}) \frac{K_{B4}}{C_{m4}} ] \quad (4.45)$$

It's clear that for the default values of the blade inlet, both values of the incidence angles will be equal.

The value of the static enthalpy can be found from the velocity components and the absolute value of the enthalpy at the inlet, and as follows:

$$h_4 = H_4 - \frac{1}{2} (C_{m4}^2 - C_{\theta 4}^2) \quad (4.46)$$

Using the equation of state at the rotor inlet, the entropy can be found as the total enthalpy and pressure at the inlet are known, and thus, we can find all the other properties at the rotor exit using the equation of state, the entropy and the exit static pressure. The width of the blade inlet can be estimated from the equation of mass conservation,

$$b_4 = \dot{m} / [2\pi r_4 \rho_4 C_{m4}] \quad (4.47)$$



The rotor exit width is the, of course, the difference between the rotor exit hub and shroud radiuses. We already found the value of the total rotor exit enthalpy in the equations previously and since we have assumed the tangential velocity component at the rotor exit is zero, the mass balance can be performed at the rotor exit by an iterative way,

$$C_{m5} = \dot{m} / [2\pi r_5 \rho_5 b_5] \quad (4.48)$$

$$h_5 = H_5 - \frac{1}{2} C_{m5}^2 \quad (4.49)$$

All the static thermodynamic conditions are defined as the static density and enthalpy by applying the equation of state, and these values are to be improved throughout the iteration procedure.

### 4.3.3 Rotor Design Evaluating

The researchers have provided some useful guidelines for evaluating the rotor design results in the preliminary phase of design and the table below shows the most important parameters and the preferred relations of them.

*Table 4.1: The Recommended Range of the Optimum Design Parameters.*

Parameter	Recommended Range	Source
Flow angle at the rotor inlet $\alpha_4$	68-75°	DIXON [31] and ROHLIK [85]
Rotor vane exit angle $\beta_5$	-50 - -70°	WHITFIELD and BAINES [104]
Rotor exit vane diameter hub to shroud ratio $D_{5h}/D_{5s}$	< 0.4	DIXON [31] and ROHLIK [85]
Rotor exit to the inlet vane diameter Ratio $D_{5s}/D_4$	< 0.7	DIXON [31] and ROHLIK [85]
Mean rotor diameter ratio $D_5/D_4$	0.53-0.66	WHITFIELD and BAINES [104]
Rotor inlet width to the inlet diameter ratio $b_2/D_4$	0.05-0.15	WHITFIELD, BAINES [104], DIXON [31] and ROHLIK [85]
Rotor tip speed to the spouting velocity $U_2/C_o$	0.55 - 0.80	BALJE [15]
Rotor exit to inlet relative velocity ratio $W_5/W_4$	2 - 2.5	BALJE [15]
Rotor exit absolute velocity to inlet rotor tip speed ratio $C_5/U_4$	0.15 - 0.5	WHITFIELD and BAINES [104]
Rotor loss coefficient $\lambda_R$	0.4 - 0.8	BALJE [15]
Nozzle Loss coefficient $\lambda_N$	0.06 - 0.24	BALJE [15]
The reaction R	0.45 – 0.65	WATANABE [103]
The ratio of the meridional velocity	1 – 1.5	WOOD [110]
The ratio of the rotor exit meridional velocity to the blade velocity	0.2 – 0.4	AUNGIER [8]
Exit shroud velocity to the inlet velocity	$\leq 0.7$	ROHLIK [85]
The flow coefficient $\phi$	0.2 – 0.3	BAINES [23]
The load coefficient $\psi$	0.7 – 0.9	BAINES [23]
Specific Diameter $D_s$	2.5 – 5	BALJE [15]
Specific Speed $n_s$	0.45 - 0.8	BALJE [15]
Power ratio $S_w$	0.15-0.25	WHITFIELD, BAINES [104]

### 4.3.4 Rotor End-Wall Contours

To avoid excessive flow profile distortion due to passage curvature effect and to get a reasonable passage area distribution, we have to confirm in the preliminary design that the inlet and exit stations are connected with smooth end-wall contours. To minimize the curvature effect, the rotor hub contour is constructed by using the large circular-arc that is compatible with the rotor dimensions obtained from the rotor sizing procedures. The radius of the circular-arc  $R_c$  is the smaller of either  $(r_4 - r_{h5})$  or  $L_R$ , and the remainder of the hub contour is constructed with a linear segment at an appropriate end of the circular-arc of the hub. At  $R_c = L_R$  the figure 4.7 illustrate the hub contour, where the segment  $L_4$  is added to complete the contour. If the  $R_c = (r_4 - r_{h5})$  it is clear that the segment  $L_5$  at the exit of the rotor is required. Using the power law relation the shroud contour is constructed to obtain a reasonable passage area distribution.

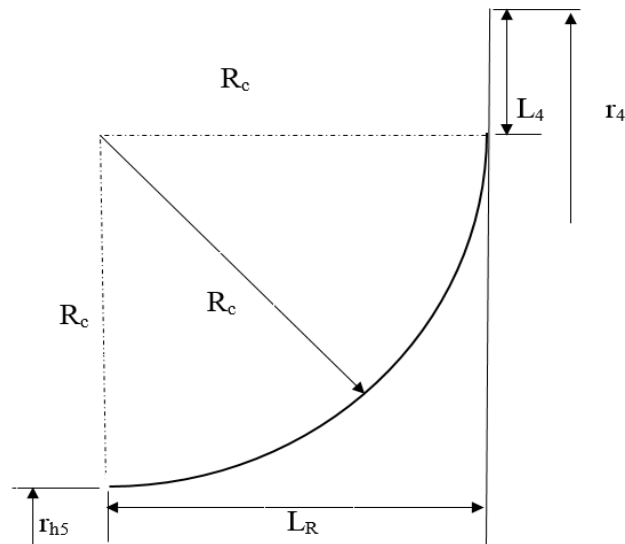


Figure 4.8: A typical hub contour as Aungier suggested.

$$r = r_{s5} + (r_4 - r_{s5})\xi^n \quad (4.50)$$

$$\xi = \frac{z - z_5}{(L_R - b_4)} \quad (5.51)$$

After defining the two end-wall contours, the meridional distance along the contours can be calculated by numerical integration then the coordinates of the contour at  $te$  mean value of  $m$  can be obtained by interpolation and as follows:

$$dm = \sqrt{(dz)^2 - (dr)^2} \quad (4.52)$$

The figure 4.9 below, shows also the mean quasi-normal used to construct the contour.

BALJE [15] suggested a reasonable basis for shroud contour design by achieving area on this mean quasi-normal,  $A_m$ , and this is approximately equal to the average of the inlet and outlet rotor areas. This is achieved by constructing contours using values of  $n$  from 2 to 9, and choosing the one at which the desired curvature passage is performed. The quasi normal length and as the ratio of the passage width is computed,  $b/R_c$  at each point on the surface, this value is qualitative measure the hub-to-shroud flow profile distortion to be expected and this parameter has to be kept less than unity.

A good illustration of the value of the preliminary end-wall contours is done by BALJE [66] where the normalized passage width and the area distribution area reasonably smooth. The distribution of the  $b/R_c$  is also reasonably smooth and within the expectable limit, as can be seen in the figure 4.8, but still this is also for the preliminary design phase and modifications are needed before the manufacturing.

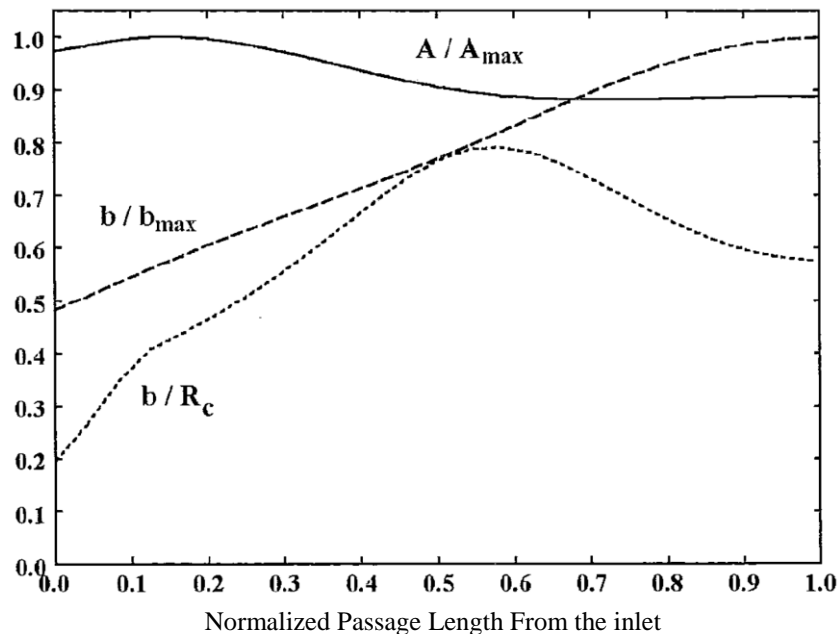


Figure 4.9: Typical Rotor Geometry Distributions,  $Aria/Aria_{max.}$ , Rotor inlet width  $b/$  Rotor inlet width  $b_{max.}$  and the Rotor inlet width  $b/$  Chord radius, [15].

### 4.3.5 Straight Line Element Rotor Blade Camberline

Constructing the straight-line element blades is done as described in BALJE [15] by defining the blade geometry on the end-wall contours and connecting the corresponding blade camberline and surface defining points with straight-line elements. An acceptable three-dimensional blade geometry is provided and is relatively easy to design, analyze and manufacture. Integrating the equation 5.53 from the exit to the inlet of the rotor i.e.  $m_5 = 0$  and  $m_4 =$  the total meridional length of the contour, where the camberline along the shroud contour is defined as follows:

$$\theta(m) = Am + B m^3 + C m^4 \quad (4.53)$$

The coefficients of the right-hand side of the equation above can be defined to match the blade angles at the inlet and the outlet of the rotor blade and to require the first and the second derivative of the equation 4.54 to be zero at the end point. This requires the blade angles on the end-wall contours to be related to the known blade angles at the midpassage position. It is also assumed that the blade angle at the inlet is constant from the hub to the shroud, and at the exit it is assumed that the  $C_\theta = 0$  and  $C_m$  is constant from the hub to the shroud. Therefore,

$$r_{s5} \tan \beta_{s5} = r_{h5} \tan \beta_{h5} = r_5 \tan \beta_5 \quad (4.54)$$

The coefficients then can be defined as follows:

$$A = \frac{\cot \beta_{s5}}{r_{s5}} \quad (4.55)$$

$$B = \frac{1}{m_4^2} \left[ \frac{\cot \beta_5}{r_5} - \frac{\cot \beta_{s5}}{r_{s5}} \right] \quad (4.56)$$

$$C = \frac{B}{2m_4} \quad (4.57)$$

The camberline of the hub contour is defined by the equation

$$\theta(m) = Dm + E m^2 + F m^3 \quad (4.58)$$

The coefficients of the right hand side of the equation above can be determined by matching the blade angles at the end points and requiring that  $\theta_4$  is constant from the hub to the shroud at the rotor inlet, and it is shown from the shroud camberline

$$\theta_4 = \frac{m_4}{2} \left[ \frac{\cot \beta_5}{r_5} + \frac{\cot \beta_{s5}}{r_{s5}} \right] \quad (4.59)$$

And the constants of the hub camberline can be defined as follows:

$$D = \frac{\cot \beta_{h5}}{r_{h5}} \quad (4.60)$$

$$E = \frac{3\theta_4}{m_4^2} - \frac{1}{m_4} \left[ \frac{\cot \beta_{h5}}{r_{h5}} + \frac{\cot \beta_4}{r_4} \right] \quad (4.61)$$

$$F = \frac{1}{m_4^2} \left[ \frac{\cot \beta_{h5}}{r_{h5}} + \frac{\cot \beta_4}{r_4} \right] - \frac{2\theta_4}{m_4^3} \quad (4.62)$$

The definition of the corresponding blade angle distribution for either contour is

$$\cot \beta = r \frac{\partial \theta}{\partial m} \quad (4.63)$$

The end-wall angle distributions generated with the camberline constructed for the end-wall-contour in the preliminary design stage, is shown in the figure 4.9 below.

The thickness for the blade is set to be equal to the blade inlet thickness except the last 10% of the blade length where it is tapered linearly to the discharge blade thickness, which is assumed to be the half of the inlet blade thickness.

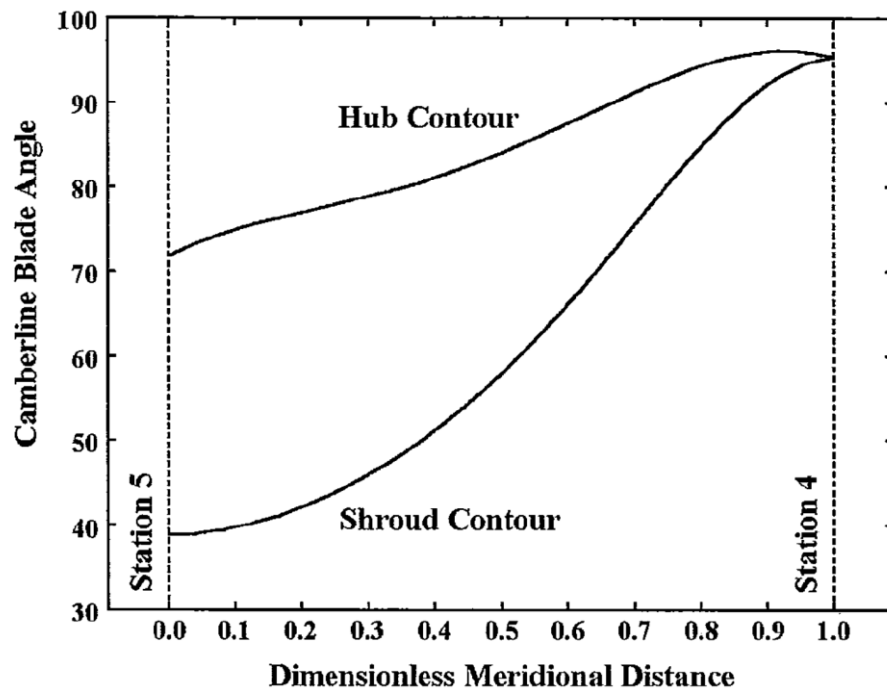


Figure 4.10: Straight-Line Elements Blade Angles, [15].

### 4.3.6 Radial Element Rotor Blade Camberline

As our application needs that the turbines operates at high speed, the radial elements method is used to construct the rotor blade camberlines. Using this method eliminate the bending stresses in the blade due to the centrifugal forces, as it is not the optimum choice from the perspective of the aerodynamics design performance, the radial-element blade may be used to provide an adequate mechanical integrity. This radial element blade camberline is defined as follows:

$$\frac{\partial \theta}{\partial r} = 0 \quad (4.64)$$

Therefore, one end-wall contour is sufficient to define the blade camberline at  $\theta$  distribution i.e.  $\theta$  must be defined as constant from  $z_{h4}$  to  $z_{s4}$ , so, the shroud camberline is the obvious choice. That means for the radial element camberline, the shroud camberline defined in the equation 4.54 through the equation 4.57 is also used. The coefficients are somewhat simplified by putting  $\beta_4 = 90^\circ$ , and that defines the distribution of  $\theta$  as a function of  $z$  and the hub camberline can be constructed by numerical interpolation of  $\theta$  as a function of  $z$ , as we can see it in the figure 5.65 below. The blade thickness distribution is the same of the straight-line element method.

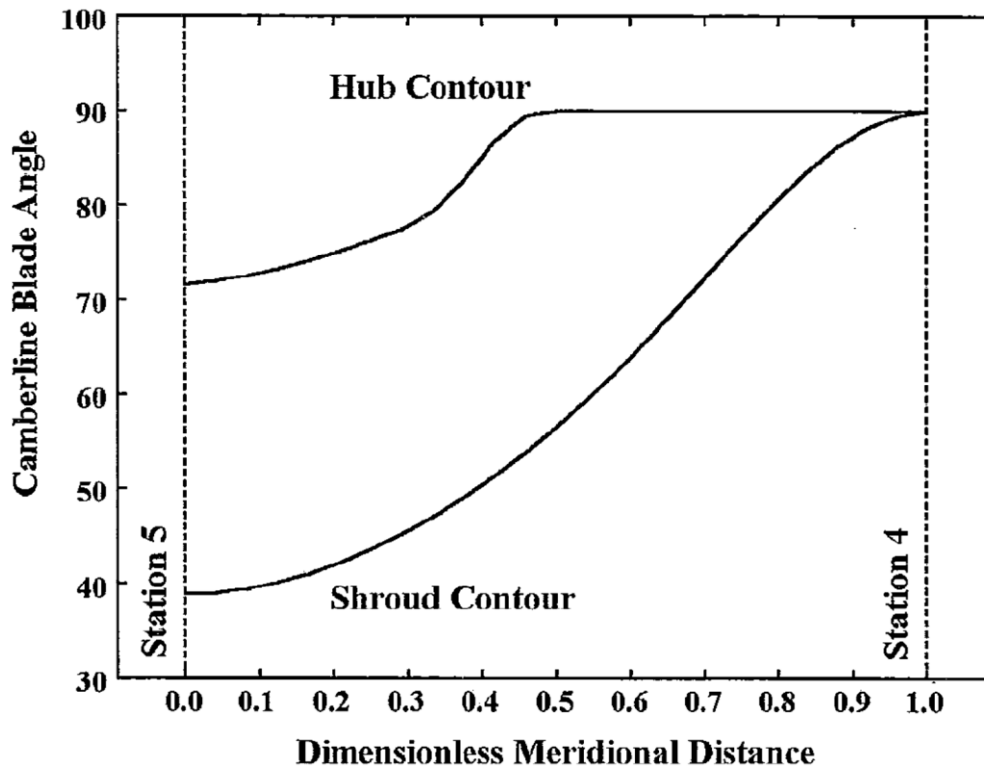


Figure 4.11: Radial-Elements Blade Angle Distribution, [15].

### 4.3.7 The Equation of State of Real Gases

As we introduced the ethanol ( $C_2H_5OH$ ) to be the working fluid and as it has to be a dry gas throughout its flowing in the turbine components, we have to be aware of choosing its properties according to the real gas equation of state. The general thermal equation of state for any fluid is as follows:

$$\frac{P}{\rho RT} = z(T, P) \quad (4.65)$$

Where  $z$  is the compressibility factor. The thermally perfect gas is a special case where  $z=1$ . For many years the compressibility factor was obtained from tabular data as in NELSON and OBERT [70] and PILTZER [75]. In the recent time there are many excellent real gas equations of state and one can employ to in the practice. Real gas equations of state can provide the many other thermodynamic parameters required and normally yield better accuracy and superior computational speed when used in numerical



analysis. For a general aerodynamic analysis one of the simple two-parameter equations is a good choice. These models offer a good accuracy, excellent computational speed and easy access to the required gas property data for almost any working fluid or fluid mixture, as AUNGIER [8], said. Among the most accurate two-parameter equation is the Redlich-Kwong equation, and other modifications made by AUNGIER [7], SOAVE [96], and WILSON [108]. These equation of states have been evaluated by Aungier in a considerable details for twelve compounds over a wide range of temperature and pressure. More care has been taken to the acentric factors,  $\omega$ , as this parameter has been extensively used in the modified Redlich-Kwong equation of state, which can improve the accuracy of the prediction, acentric factor is defined by PITZER [75] as follows:

$$\omega = -\log_{10} \left( \frac{P_v}{P_c} \right) - 1 \quad \frac{T}{T_c} = 0.7 \quad (4.66)$$

Where  $P_v$  is the pressure on the vapor saturation line and the subscript c designates a critical point property.

It was concluded that the original Redlich-Kwong equation of state and the Aungier's modified Redlich-Kwong are suitable for general turbomachinery aerodynamics design and analysis, but the other modified equations by other researchers are only applicable over a particular compounds and where they were developed and show some improvement but they show a reduction in the accuracy and serious deficiency when the acentric factor  $\omega$  less than zero and also they exhibited less accuracy for the supercritical pressure i.e. when the pressure is greater than the critical pressure, as AUNGIER [8] said.

The original Redlich-Kwong equation is

$$P = \frac{TR}{V - b} - \frac{a}{V(V + b)\sqrt{T_r}} \quad (4.67)$$

Where  $T_r = T/T_c$  is referred to as the reduced temperature, and

$$a = 0.42747 R^2 \frac{T_c^2}{P_c} \quad (4.68)$$

$$b = 0.08664 R \frac{T_c}{P_c} \quad (4.69)$$

The equation requires only the critical temperature and the critical pressure for the fluid and the caloric equation of state data for its application. It offers a good accuracy over a wide range of thermodynamic conditions, but it has one well-known deficiency near the critical point of the fluid, as mentioned in AUNGIER [8].

The AUNGIER's modified Redlich-Kwong equation of state [7] is

$$P = \frac{TR}{V - b + c} - \frac{a}{V(V + b) T_r^n} \quad (4.70)$$

$a$  and  $b$  are the same for the original; Redlich-Kwong Equation, and  $n$  is given by the following equation,

$$n = 0.4986 + 1.1735 \omega + 0.4754 \omega^2 \quad (4.71)$$

The constant  $c$  is calculated by applying all the critical point properties. And it is included to remove the deficiency for the original equation near the critical point.

As mentioned in JOHNSON [55] a more complex but a highly accurate real gas model is the eight-parameter Benedict-Webb-Rubin, BWR. In the solver we used the equation used is the Redlich-Kwong as it is sufficiently accurate enough for our analysis.

## 4.4 Inviscid Solution Method

The equation of continuity, momentum and energy governing the flow of an inviscid flow, in their most general form, contain time derivatives, as we have seen in the previous chapter. Two solution techniques are available for the steady flow. The first is by removing the time from the equation and the remaining terms then may be solved in their existing form for the so called primitive variables such as temperature, pressure and velocity. In practice it is more common to rewrite the equation and solve them in term of non-simple functions such as the velocity potential or stream function, as mentioned in WHITFIELD [104]. The advantage of this is the reduction of the number of terms to be solved at each grid point from four in the two dimensional flow and five in the three dimensional flow (two thermodynamic properties and two or three velocity components) to a single term. However, this procedure is normally accompanied with less in generality and difficult in setting the boundary conditions, due to the new complex form of the variables.

The second method is to solve the full time-varying equation by starting a guessed initial flow of the field and proceeding in marching the equation through the time until the

solution converges to a steady state and the time part disappeared, and this method is often known as time marching method, and it is widely applicable for the turbomachinery problems. But it is more expensive as it requires more iterations and hence longer time.

Streamline curvature method, potential flow methods and time dependent Euler equation solution are also related to this category

## 4.5 Viscous Solution Method

There is now a little doubt that there exist in the radial turbines, significant regions in the flow dominated by viscous processes. The diffusion in process in the stator is strongly dependent on the growth of the boundary layers. In the rotor of the radial inflow turbine, evidence exists that the secondary flows are significant in redistributing low momentum fluid through the passage, and this not only a fraction of the total aerodynamic loss but also influences the rotor exit flow angle or deviation  $\beta_5$ , said WHITFIELD [104]. To model these features demands the solution of the full Navier-Stokes equations including the viscous shear term, and since in very few cases are flows likely to be wholly laminar, turbulence must also be included. Some difficulties are also existed in dealing with shock waves and thin shear layers such as boundary layers and wakes, which need a large number of grid points and highly refined mesh.

The flow of compressible fluids through the turbomachines are invariably turbulent during some, if not all, of their progress through the machine and even if the Reynolds number is sufficiently low in a way that the natural transition doesn't occur itself, but there is enough sources of disturbance in a form of blade and rows bends and discontinuities in the flow passages to introduce transitions. So that, the solution of Navier-Stokes equations requires that the account should be made for the effect of the turbulence.

The Navier-Stokes equations in their Reynolds average form is a common choice for the engineering applications in which the effect turbulence appears shear stress terms to be added to the laminar viscous stress [104].

## 4.6 Coupled Viscous-Inviscid Methods

As mentioned in many literatures, in many cases viscous effects are important only in limited regions of the complete domain, and thus it is recommended to combine both viscous and inviscid methods mentioned in the last two sections. In which the bulk of the flow is solved by one of inviscid technique, and only in those regions where it is important are viscous terms brought into the calculations. The solution with this method is considerably acceptable and more economical.

## 4.7 Nozzle Row Analysis and Sizing

The main function of the nozzle vanes is to set the angle of approach of the working fluid to the rotor and imparting some swirl to the stream. The form of the nozzle depends on whether the nozzle ring is preceded by a volute or by a simple collector. However, sometimes the swirl provided by the volute is sufficient to present the fluid to the rotor with an appropriate incidence angle and the nozzle row is simply removed or the function of the nozzle vanes will be just to remove the circumferential non-uniformities in the flow and accelerate it further. Sometimes, additional turning for the flow is required and thus a little camber is needed or possibly none at all. Whether if the nozzle is preceded by a collector, the nozzle has to accelerate the flow and turn its direction, as the collector doesn't generate the swirl itself.

The conformal transformation of the axial design cascade is one of the most common design method used to transform the axial cascade to the annular plane, and the used equations are

$$\theta = \frac{x}{r_o} \quad (4.72)$$

$$r = r_o \exp(y/r_o)$$

Where  $r_o$  is the reference radius, such as the trailing edge radius and the  $x, y$  are the usual Cartesian coordinates of the linear vane and  $r, \theta$  are the polar coordinates of the transformed profile. This method has been described by WICEL SINUS [109] and explained further by HIETT and JOHNSON [46], RIBAUD and MISCHEL [82] and WHITFIELD [10].

An important parameter that has to be sized is the throat area of the nozzle which has to be sized to pass the required mass flow rate, which can be given in the following equation.

$$A_{th} = \frac{\dot{m} \sqrt{RT_{o th}} / \gamma}{P_{o th}} \frac{1}{M_{th}} \left( 1 + \frac{\gamma - 1}{2} M_{th}^2 \right)^{\frac{\gamma + 1}{2(\gamma - 1)}} \quad (4.73)$$

If the nozzle is purely convergent the throat area can be written in term of the nozzle exit geometry and the lockage factor .the latter would be expected to be small in an accelerating passage.

$$A_{th} = \pi d_2 b_2 (1 - B K_{th}) \cos \alpha_2 \quad (4.74)$$

The nozzle exit Mach number in the unchecked nozzles is the throat Mach number which is also the absolute Mach number at the entry of the rotor. The nozzle can be assumed to be adiabatic in the preliminary design as the flow is very fast and spending very short

time in the nozzle passage, and then the exit temperature is constant. An isentropic approach is sufficient at the beginning of the design, and since the losses in the nozzle has a very small fraction of the overall turbine losses, which is estimated by Kofsky and Wassebauer to be about 5 per cent and increased to 15 per cent with increasing the velocity and the frictional area surface. The total pressure can also be assumed to be constant [10].

In the choked nozzles, further acceleration in the gas can only be achieved if a convergent-divergent nozzle is arranged, but this is an unusual situation in the radial turbine and especially in our application it is to be avoided as it adds more complexity and hence cost to the design.

Another approach is a tuning process placed on the trailing edge via an expansion fan and if the expansion is assumed to be isentropic the flow angle at the throat and the exit can be related using the following equation [89].

$$\frac{\cos \alpha_2}{\cos \alpha_{th}} = \frac{1 - BK_{th}}{M_2} \left[ \frac{2}{\gamma + 1} \left( 1 + \frac{\gamma - 1}{2} M_2^2 \right) \right]^{\frac{\gamma + 1}{2(\gamma - 1)}} \quad (7.75)$$

And for the supersonic nozzle, the equation above needs to be solved to specify the exit conditions.

The nozzle-rotor interspace is also to be estimated. However, it is common in the nozzle turbine design a small vaneless region between the nozzle exit and the rotor blade tip to be inserted which is called interspace. The smaller interspace the more compact design we get, which is preferred also in our case. But this vaneless region has to be sufficient enough to give the nozzle vane wake some space in which to mix out and produce circumferentially uniform conditions at the entry to the rotor and prevent the effect of passing rotor blades from travelling upstream and influencing the flow in the nozzle.

It is well known in the axial turbines that the wake can be observed for several chord lengths, and there's no sufficient reasons that the radial turbine will behave differently.

An empirical determination done by WATANABE [103] has been introduced at which the maximum efficiency of a radial turbine can be occurred at value of an interspace geometry parameter  $k$

$$k = \left( \frac{\Delta r}{b} \right) \cos \alpha \cong 2 \quad (4.76)$$

Or  $\frac{r_3}{r_4} = 1 + 2b \sin \alpha_4 / r_4$

Where  $\Delta r$  is the radial interspace distance between the nozzle exit and the rotor inlet and  $\alpha$  is the mean flow angle and  $b$  is the nozzle vane width. A significant influence of the rotor speed on the nozzle and also on the rotor blade surface pressure distribution if the interspace is about 2 percent and has no significant effect if it was about 20 percent, said WHITFIELD [10]. So the maximum efficiency can be reached is a compromise between the interface between nozzle and rotor which increases with reducing the clearance between the nozzle and the rotor and on the other hand the fluid friction and the boundary layer growth which increases with increasing the interspace.

AUNGIER [7] suggested also that the nozzle length has to be restricted to the following inequality an within its range

$$1.1 \leq \frac{r_2}{r_3} \leq 1.7 \quad (4.77)$$

Where  $r_2$  is the nozzle inlet radius and the  $r_3$  is the nozzle exit radius.

A governing equation of a parabolic arc for the nozzle vane camber line has been suggested by AUNGIER [7], and a very general airfoil geometry can be produced as follows

$$x^2 + \frac{c - 2a}{b} xy + \frac{(c - 2a)^2}{4b^2} y^2 - cx - \frac{c^2 - 4ac}{4b} y = 0 \quad (4.78)$$

The nozzle blades are designed by imposing a general lade thickness distribution on this parabolic arc, as a restriction  $a/c$  has to be within the following range.

$$0.25 < a/c < 0.75 \quad (4.78)$$

$\gamma_3$  is the vane setting angle and has to be equal or greater than  $5^\circ$ .

It is been recommended to adopt the blade thickness distribution in any location along the camberline as follows

$$t = t_{ref} + [t_{max} - t_{ref}] \xi^e \quad (4.79)$$

$$t_{ref} = t_2 + [t_3 - t_2] (x/d) \quad (4.80)$$

$$\xi = \frac{x}{d}; x \leq d \quad (4.81)$$

$$\xi = \frac{c - x}{c - d}; x > d \quad (4.82)$$

$$e = \sqrt{0.4d/c} \left[ 0.95 \left( 1 - \frac{x}{c} \right) (1 - \xi) + 0.05 \right] \quad (4.83)$$

Where  $t_{max}$  is the maximum thickness along the camberline and  $d$  is its location, a nose-radius is imposed at each end and  $c$  is the chord length.

## 4.8 Operating Points Estimation

The operation conditions of the turbine have been estimated based on a case study with the assumption that the lost energy through the exhaugst gases is a between 75% and 83% of the shaft power, as we have seen in the figure 1.1 above. The heat exchanger used by the turbosteamers led to salvage around 80% of the heat energy [9]. Therefore, a bout 219.7 hp (163.83 kW) automobile leads to about 15 bar and 650 K of Ethanol.

We calculated the results as we used the Rankin cycle and the fluid has been heated from the boiling line to the final superheated point as it enters the turbine.

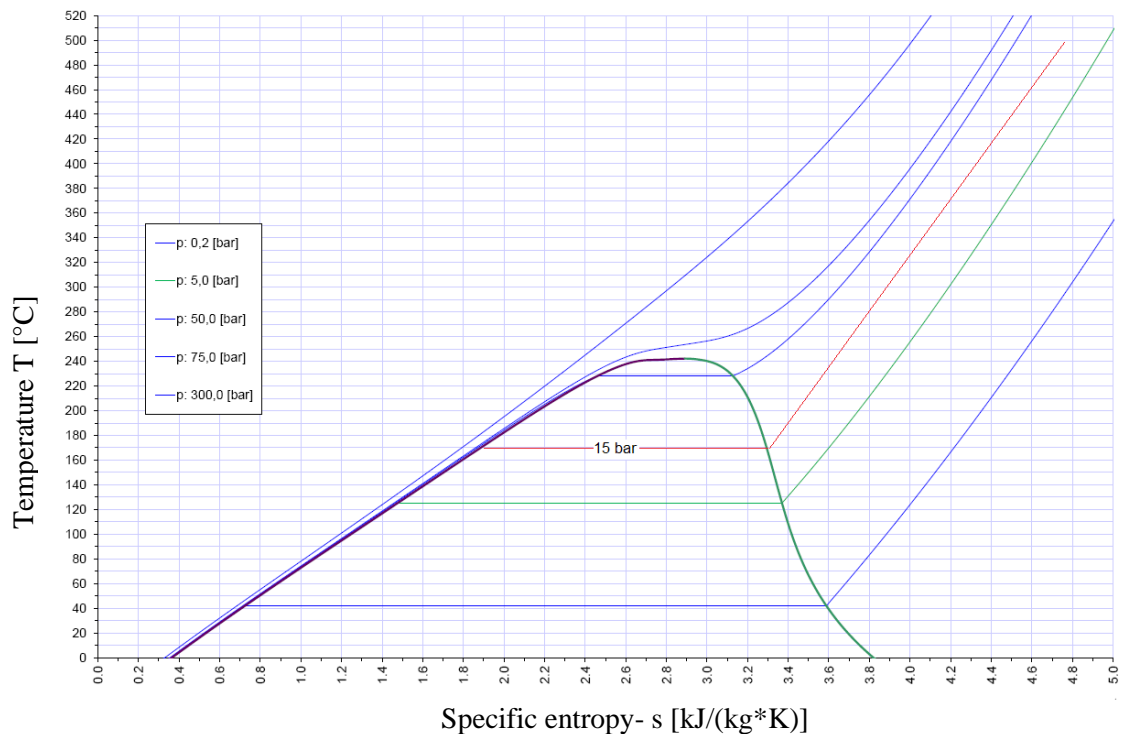


Figure 4.12: Ethanol T-S diagram.





## 5 Simulation of Radial Inflow turbine

Design the radial inflow turbine, which is the most important part in the process of recovering energy in our system, needs taking care of many design parameters and application requirements. We started the design procedure by making use of some dimensionless parameters, which are very useful for the preliminary design. The applied parameters have been recommended and reported by researchers, such as in BALJE [15], AUNGIER [8] and BAINES [10]. The main parameters are, the specific speed,  $n_s$ , the specific diameter,  $D_s$ , the Reynolds number, the velocity ratio  $v$ , Mach number, the loading and the flow coefficients,  $\psi$  and  $\phi$  respectively, and some other geometrical parameters.

The turbine inlet boundary conditions have been estimated by the energy balance. We calculated the energy transferred from the exhaust gas flow to the working fluid, which is an organic working fluid, as we assumed to be more suitable.

Choosing an appropriate turbomachine, which serves efficiently in the application of energy recovery in the automobile, is one of the main targets of this work. The organic working fluid has been first suggested is the Ethanol ( $C_2H_5OH$ ) in our case.

From our intensive literature survey, and having in mind the requirements of our application and the main characteristics of the suggested turbomachine, the radial inflow turbine is the type we chose to design and optimize to serve this duty. We used the fore written equations and correlations, with the aid of the up-to-date numerical methods, the simulation of the radial turbine is accomplished. Starting with the preliminary design and going through the parameter study and the optimization. The operating conditions of the radial turbine can be estimated by taking into consideration the thermal efficiency of the ICEs, which is 30%-50% [29] and [51], then we can calculate the wasted energy that can be redirected to the working flow (Ethanol) via a heat exchanger, and after that using the thermodynamic table of the organic working fluid together with the equation-of-state the turbine inlet conditions can be found. Different ranges of design conditions are also investigated. For calculating the energy in the heat gases, the average calorific value of diesel is (42-45) MJ/kg [49].

## 5.1 Turbine preliminary design

A number of methods have been suggested for obtaining the overall dimensions of the turbine geometry. ROHLIK [85] drew a chart that related the specific speed to the ratio of tangential velocity to the rotor tip speed. BENSON [17] and [16] has analyzed the turbine performance at a wide range of operating conditions and the sensitivity of the performance to various geometrical and aerodynamic parameters. BAINES [13] and [10] has suggested an integrated approach of designing a radial inflow turbine, which is a rapid cost-effective design and optimization method, he suggested using the loading and flow coefficients in combination with the mean-line approach and then he plotted a contour shows the correlation between these two coefficients, as shown in the figure 5.1 below

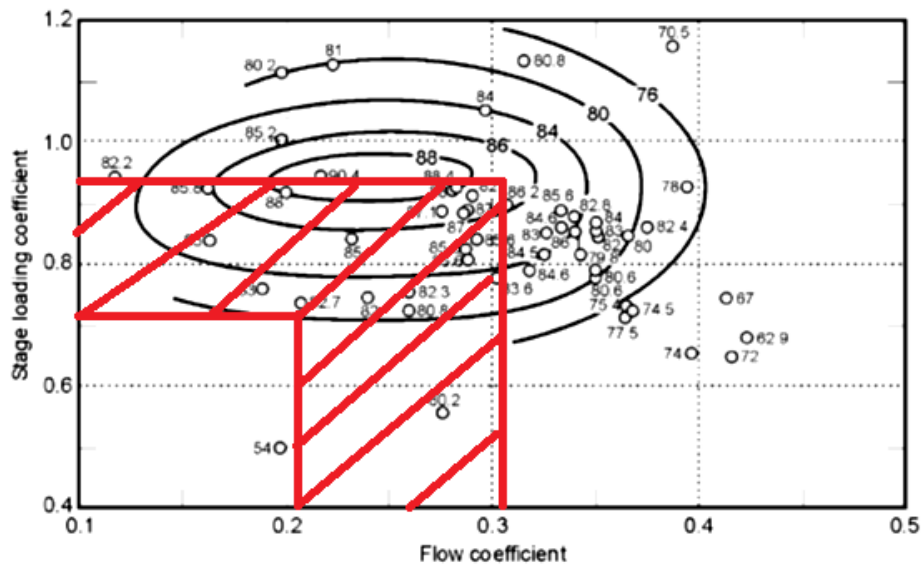


*Figure 5.1: Stage loading coefficients for radial turbines with radial section blades versus flow coefficient and the data points show the total to static efficiency, [12]*

As mentioned in WRIGHT [111], Cordier diagram which has been developed further by BALJE [15], introduced a guide lines for the combination of the specific speed and the specific diameter at the optimum efficiency.

We used this diagrams together with the flow and load coefficient to choose the operating points and the preliminary design for our radial inflow turbine. The figure 5.2 below shows the correlation between the specific speed and the specific diameter.

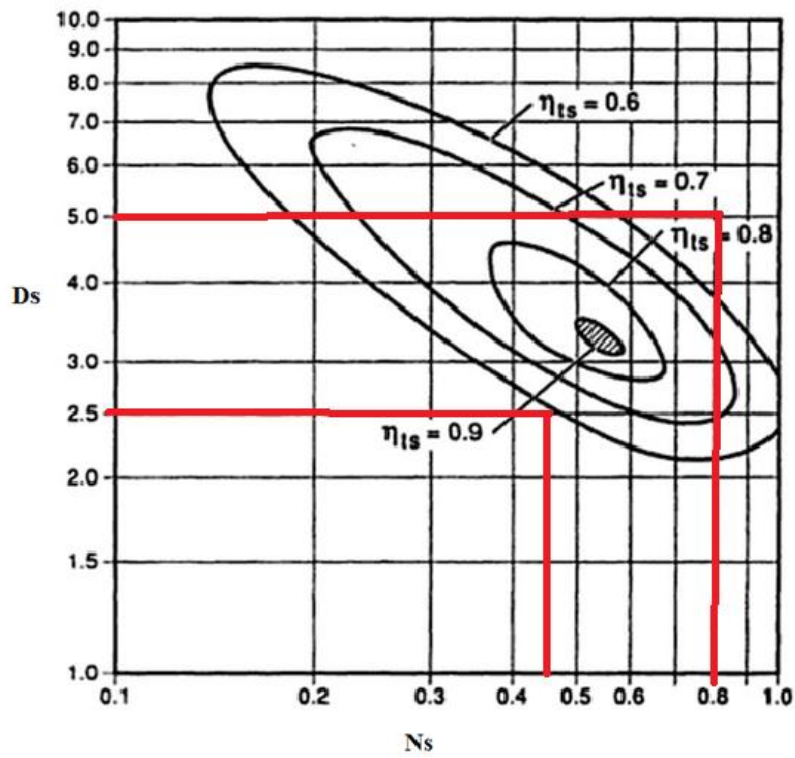


Figure 5.2: Balje diagram for the radial inflow turbine, [32].

Starting with Euler turbomachinery equation

$$\frac{w}{m} = \frac{1}{2} [(U_4^2 - U_5^2) + (C_4^2 - C_5^2) - (C_{w4}^2 - C_{w5}^2)] \quad (5.1)$$

Since many losses including friction and exit kinetic energy increase as the square of velocity so in general the aim is to keep the flow velocities as low as reasonably possible. The incidence angle is also a crucial parameter on the performance of the turbine, where the optimum incidence of through flow depends solely on the geometric characteristics of the runner, i.e., blade curvature, thickness and solidity SHAH [89].

## 5.2 Mesh Independence Analysis

Using the commercial ANSYS-CFX 14.5 software, a 3D viscous turbulent simulation has been carried out. The three dimensional computational mesh for the simulation of the radial inflow turbine used, has been shown in the figure 5.1 for the nozzle passage. ICEM and Turbogrid are commercial software for generating the mesh. They are capable enough to create an efficient grid for the turbine components in use. The figures 5.3 to 5.6 shows a part of the mesh created for the numerical simulation.

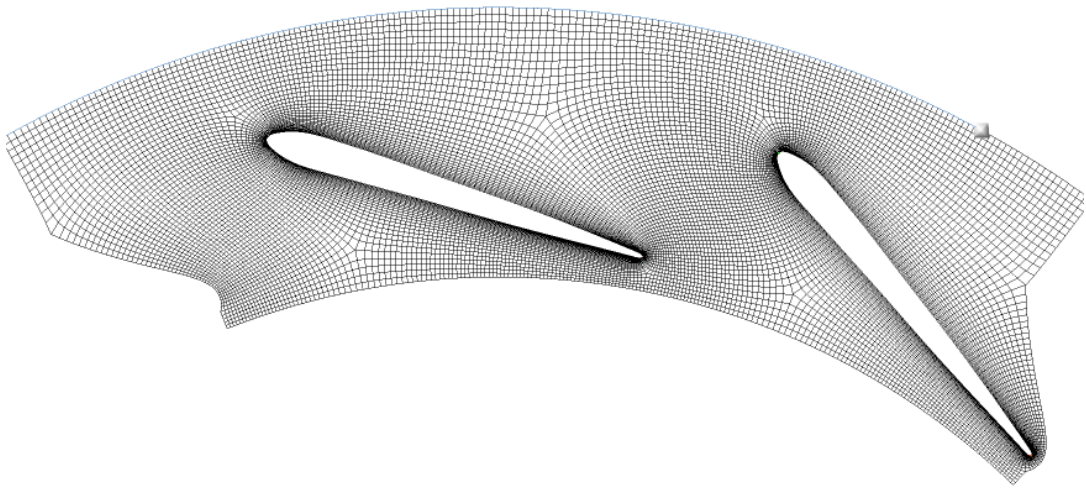


*Figure 5.3: Mesh of the nozzle passage.*

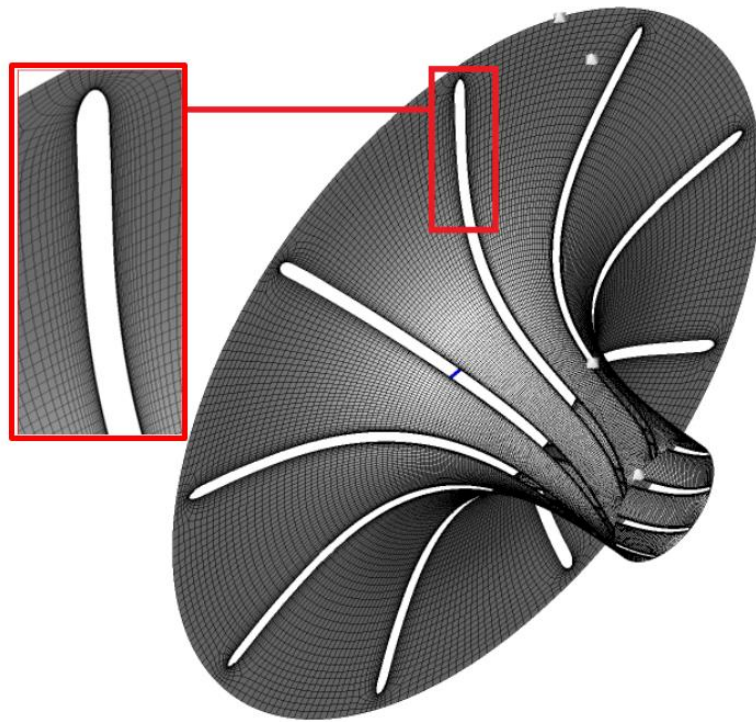


*Figure 5.4: The mesh of the rotor blades at the hub.*



*Figure 5.5: Control volume with one nozzle passage.*

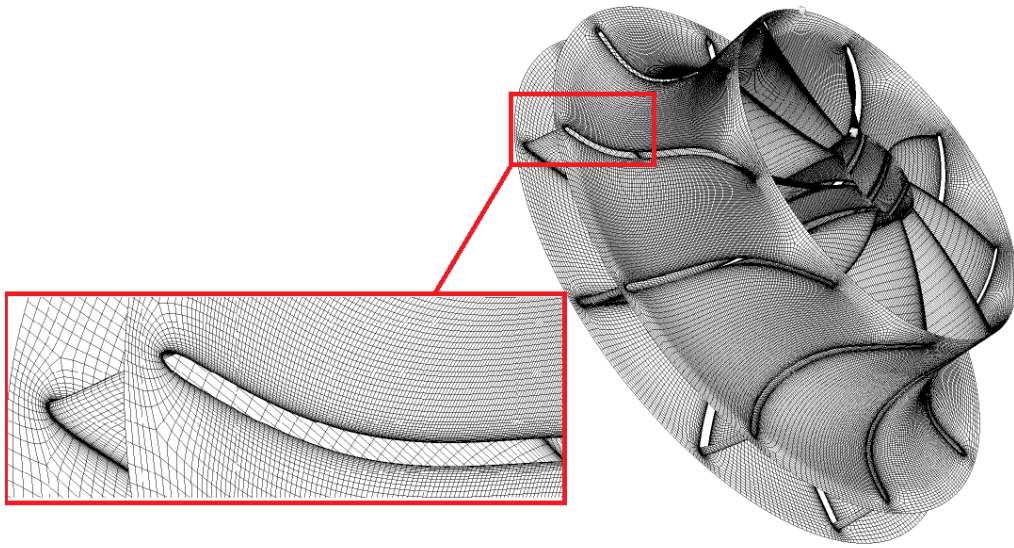


*Figure 5.6: The mesh of the rotor blade.*

The total grid number of the initial created mesh has been analyzed. A mesh independence analysis has been done by running the simulation from a very coarse mesh with 116,256 nodes to a very fine mesh with 1,247,145 nodes, and for different intermediate refinements values between these two upper and lower limits. We found the numerical calculations can be regarded to be mesh-independent with 363,300 nodes. 153,318 nodes for the nozzle and 209,982 nodes for the rotor passage.

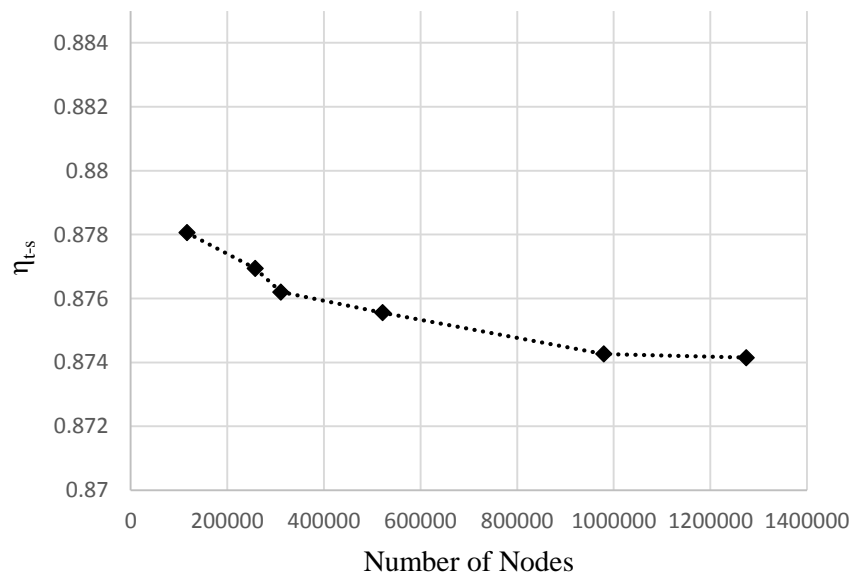


*Figure 5.7: Mesh independence analysis.*

After the computational system has been discretized with different degrees of mesh refinement. The convergence criteria have been examined, and for this purpose the total-to-static efficiency was taken as a monitoring parameter of interest and insured to have reached the steady state, the imbalances and the residuals have been also observed and checked of being equal or less than the recommended ranges of the convergence criteria. For the imbalances a value below 1% is acceptable and for the minimum residuals a value below  $1E-4$  and a value below  $1E-3$  for the maximum RMS residuals are also acceptable [5]. Monitoring points have been used to observe the total pressure, Mach number, total enthalpy, total temperature and the isentropic efficiency at these points. We have put two points exactly at the nozzle exit, other two point at the inlet of the rotor blade and other two at the exit section of the rotor blade.

All of the parameters have reached a steady state at the end of the simulation, as we can see below the figures 5.5, 5.6, 5.8 and 5.7 are for the total pressure, Mach number, total temperature at point 4 which is at the trailing edge of the rotor blade.

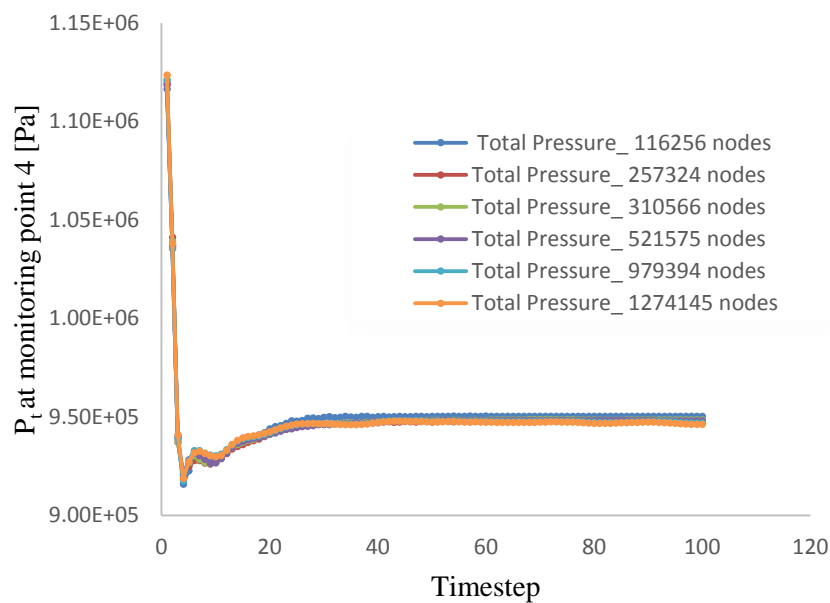


Figure 5.8: Total pressure at monitoring point 4.

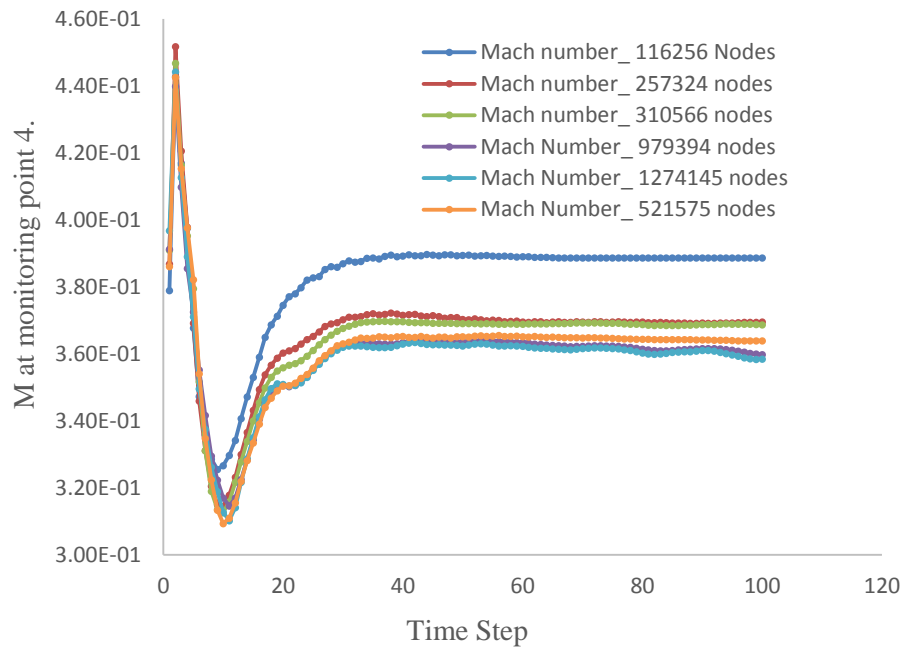


Figure 5.9: Mach number at monitoring point 4.

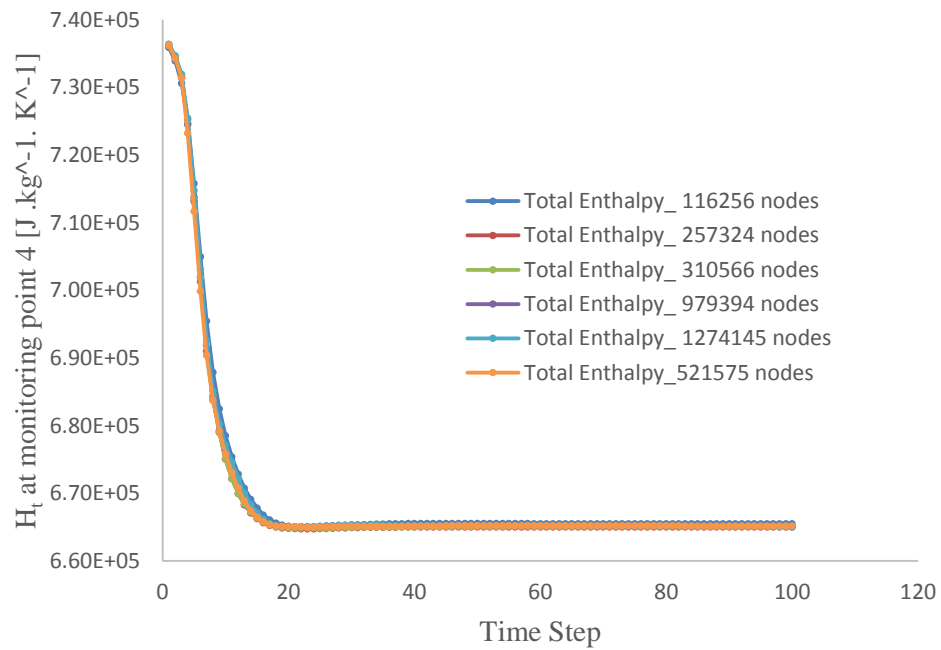


Figure 5.10: Total enthalpy at monitoring point 4.



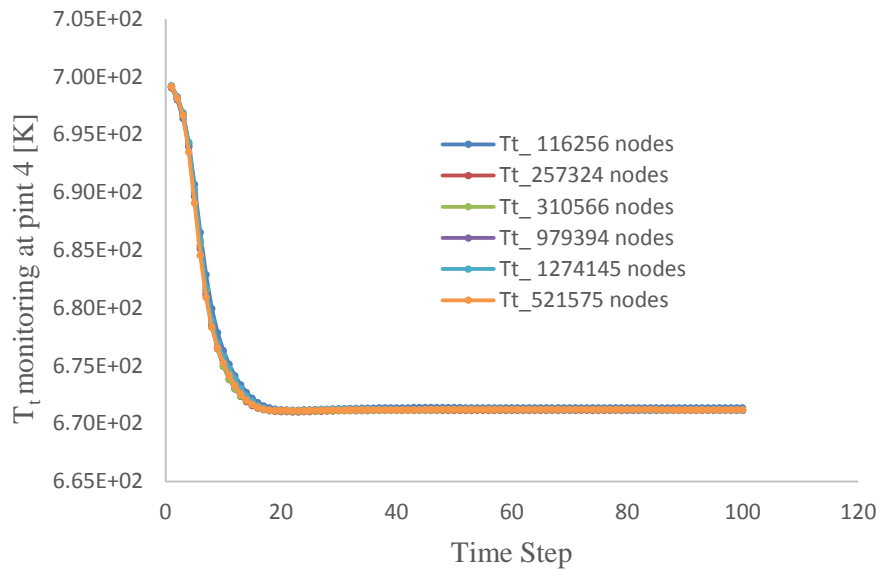


Figure 5.11: Total temperature at monitoring point 4.

The turbulence model used was the SST  $k-\omega$  model which has been found to have the efficiency to capture the flow details better than the other turbulence models although its ability in capturing accurate details in the transitions needs to be improved, as we will later see in this chapter. It has been recommended by many other researchers, like in TSUEI [99], WILCOX [106].

For our further calculations a case of 363,300 nodes is fine enough and can be regarded as a grid independence.

The table 5.1 below summarize the results of the calculations made for the grid independence analysis.

Table 5.1: Summary of the mesh-independence work-through.

Total Number of Nodes	Mass imbalance in the Stator domain (%)	Mass imbalance in the rotor domain (%)	Total energy imbalance in the stator domain (%)	Total energy imbalance in the rotor domain (%)	RMS Residuals for the U-Mom.	RMS Residuals for the V-Mom.	RMS Residuals for the W-Mom.	RMS Residuals for the H-Energy	RMS Residuals/turb. K.E
116256	2.70E-03	1.58E-02	3.10E-03	1.28E-02	2.50E-05	2.10E-05	1.30E-05	4.80E-05	1.10E-04
257324	1.60E-03	1.51E-02	1.70E-03	1.73E-02	7.90E-05	5.20E-05	6.50E-05	5.40E-05	1.80E-04
310566	1.30E-03	2.00E-03	1.40E-03	2.50E-03	6.50E-05	2.90E-05	3.90E-05	3.60E-05	1.00E-04
521575	1.10E-03	2.30E-03	1.00E-03	1.20E-03	1.50E-05	1.10E-05	1.10E-05	1.90E-05	4.70E-05
979394	2.00E-04	2.01E-03	3.00E-04	3.07E-03	2.40E-05	1.00E-05	2.40E-05	1.30E-05	8.20E-05
1274145	6.40E-03	1.81E-03	7.10E-03	2.92E-03	3.50E-05	1.20E-05	2.80E-05	2.00E-05	1.30E-05

### 5.3 Validation of the results

The data of the turbines which work with an Organic Rankine Cycle near or above the critical point and with high density working fluid, are rare and especially for the 3D simulation, analysis, design and optimization. In this case and as a validation for our first step in the preliminary design, we compared our preliminary results from the 3D simulation with ANSYS-CFX 14.5 to those got from a Vista RTD, which is a commercial mean-line code, and this mean-line code has been validated over a wide range of experimental results. This code needs a fixed value of mass flow rate, the stage input thermodynamic properties, the number of blades, rotational velocity [73]. The required input values have been calculated by using MATLAB R2014a to solve the turbomachinery equations of the recommended input parameters for the preliminary design.

The table 5.2 below shows a very good agreement between the values we got from the mean-line code Vista RTD and those simulated in the 3D CFD tool, the ANSYS-CFX 14.5 is in this case.

The main thermodynamic and geometrical parameters have been compared, and it is clear that the shaft power has notable difference and the reason behind that is that the mean-line code accepts just a constant specific heat capacity and gas constant values whether the value of them are changing significantly with the temperature,  $C_p, R = f(T)$ , and the values of them in ANSYS-CFX are used as proposed by Redlich-Kwong as we mentioned that previously.

Table 5.2: Comparison of the mean-line analysis and the 3D-CFD simulation.

Variable	Mean-line Design	Preliminary 3D Viscous CFD	Difference %
$\eta_{t-s}$ [%]	79.2	83.7164	8.978408
$\Pi_{t-s}$ [-]	1.72	1.6168	6.382979
Shaft power [kW]	20.918	23.0488	9.244733
$P_{t2}$ [kPa]	1500	1490.97	0.605646
$M_{abs\ 3}$ [-]	0.582	0.606	3.960396
$M_{rel\ 3}$ [-]	0.271	0.2555	6.066536
$U_3$ [m s <sup>-1</sup> ]	258.126	265.18	2.66008
$V_3$ [m s <sup>-1</sup> ]	238.402	254.514	6.330497
$\alpha_3$ [deg.]	65.757	67.6925	2.859253
$\beta_3$ [deg.]	-18	-17.8854	0.640746
$T_{t4}$ [K]	680	673.1	1.025108
$T_4$ [K]	676.4	671.565	0.71996
$P_{t4}$ [kPa]	925.93	921.729	0.455774
$P_4$ [kPa]	873.15	885.036	1.342996
$d_3$ [mm]	39.409	42	6.169048
$b_3$ [mm]	3.9	4	2.5
$d_{hub\ 4}$ [mm]	7.094	7.4	4.135135
$d_{shroud\ 4}$ [mm]	26.246	27.8	5.589928
$d_3/d_{rms\ 4}$ [-]	2.05	2.064	0.678295

## 5.4 The Turbulence Models Effect

For the turbomachinery simulation, selecting a suitable turbulence model can be a challenging task. There's no single model suitable for all types of turbomachinery simulation. Two equation models, like  $K-\epsilon$  and  $K-\omega$ , are common choices for predicting cases with difficulties like flow separation, rotating flow, the flow strongly affected by secondary flow etc. The two equation models are based on the Boussinesq eddy viscosity assumption which leads to an over production of the turbulent energy in the regions of strong acceleration or deceleration like the leading edge, SCHMITT [92]. An SST-  $k-\omega$  model with automatic wall function can, generally, better predict the flow behavior compared to the classical like  $k-\epsilon$  and  $k-\omega$  models.

The figure 5.12 below shows the static pressure predicted by using the standard  $K-\epsilon$  turbulence model with scalable wall function and the SST  $K-\omega$  model with automatic wall function, and the figure below shows the difference between the two models in predicting the static pressure. It is clear that there's difference between the two models particularly in the boundary layer region, which is actually expected as these two turbulence models behave differently in these regions.

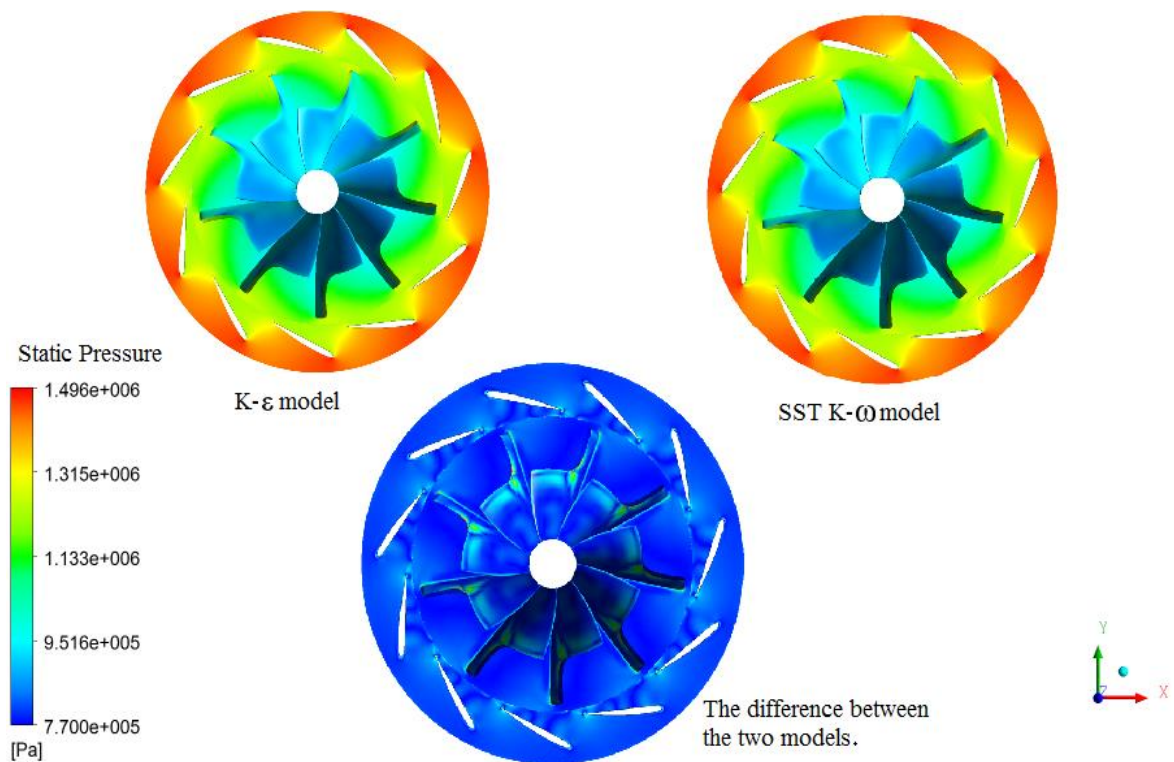


Figure 5.12: The effect of using  $k-\epsilon$  and SST  $k-\omega$  turbulence models on the pressure prediction.

## 5.5 Inlet boundary and off-design conditions effect

The effect of different boundary conditions has been analyzed and the sensitivity of the main thermodynamic properties has been studied. A 3D numerical simulations have also been performed at off-design conditions for different total inlet temperature and at different rotational speed. For the nominal rotational speed, 80% and 120% of the nominal speed. The velocities and the different flow angles have been calculated at the midline of the blade i.e. at 50% span.

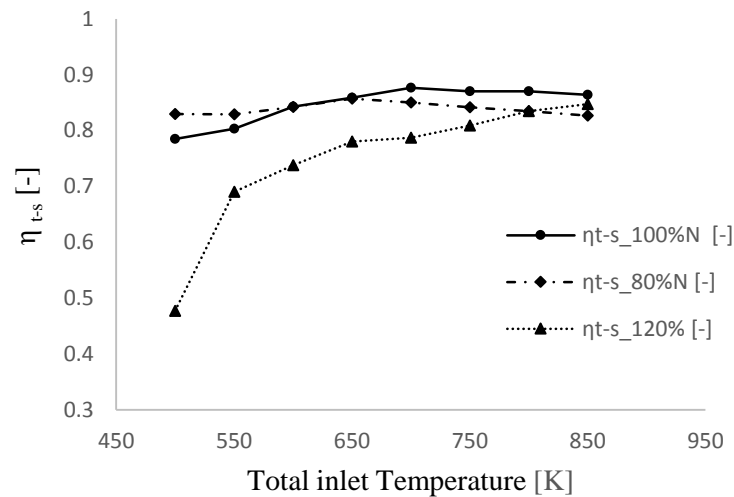


Figure 5.13: The effect of the total inlet temperature on the total to static efficiency  $\eta_{t-s}$  at different rotational speeds  $N$ .

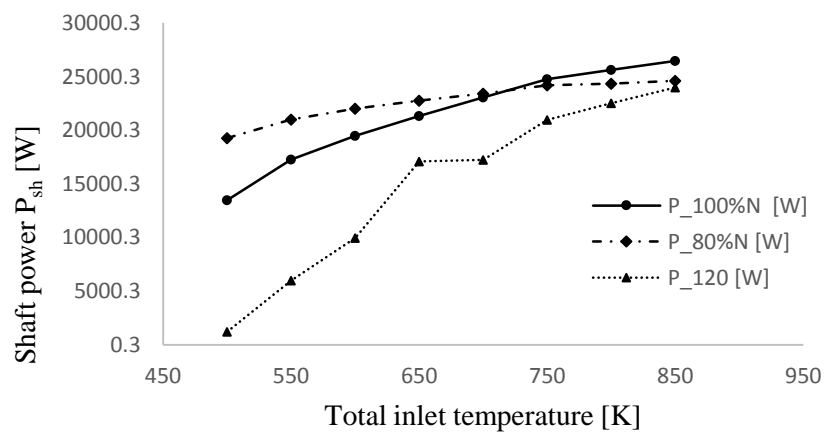


Figure 5.14: The effect of the total inlet temperature on the shaft power  $P_{sh}$  at different rotational speeds  $N$ .

From the figures 5.13, it is clear that at the nominal speed, the turbine can effectively handle temperature variation with a variation of the total to static efficiency in the range of 6%, over the tested range of temperature. At temperatures lower than the nominal one the 80% nominal speed has a total to static efficiency slightly higher than the nominal at total inlet temperature lower than 590 K, the nominal speed has the maximum efficiency, as one can see in the figure 5.13 above.

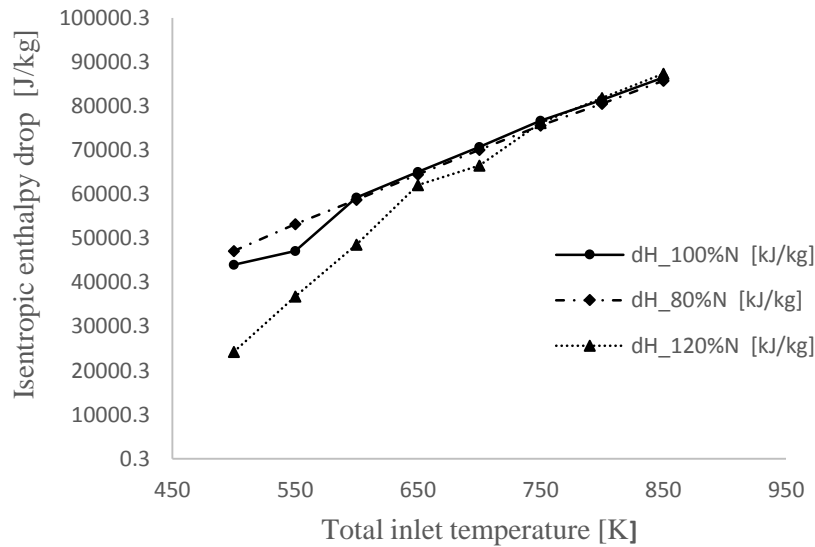


Figure 5.15: The effect of the total inlet temperature on the isentropic enthalpy drop at different rotational speeds  $N$ .

In the figures 5.14 and 5.15, and as we expected, the behavior of the turbine for the output power and the isentropic drop of enthalpy is similar. It is clear that both parameters are increasing with the increase of the total inlet temperature, as the specific heat constant at constant pressure,  $c_p$ , is increasing with increasing of temperature and at specified temperature drop the enthalpy drop will be a function  $c_p$ .

The degree of reaction of the turbine, which represent the ratio of the static enthalpy drop in the rotor to the enthalpy drop in the stage, recommended to be in the range of 0.45-0.65, as mentioned in WATANABE [11]. It behaves, as shown in figure 5.16, not much sensitively to the inlet temperature at the nominal speed, but the sensitivity increases at the off-design conditions. At the nominal speed the reaction is 0.5336, and the deviation of it over the range of the inlet total temperature is for 0.59 to 0.54, which is acceptable and within the recommended range. While at 120% nominal speed, the reaction exceeds the recommended range, particularly at low temperatures.

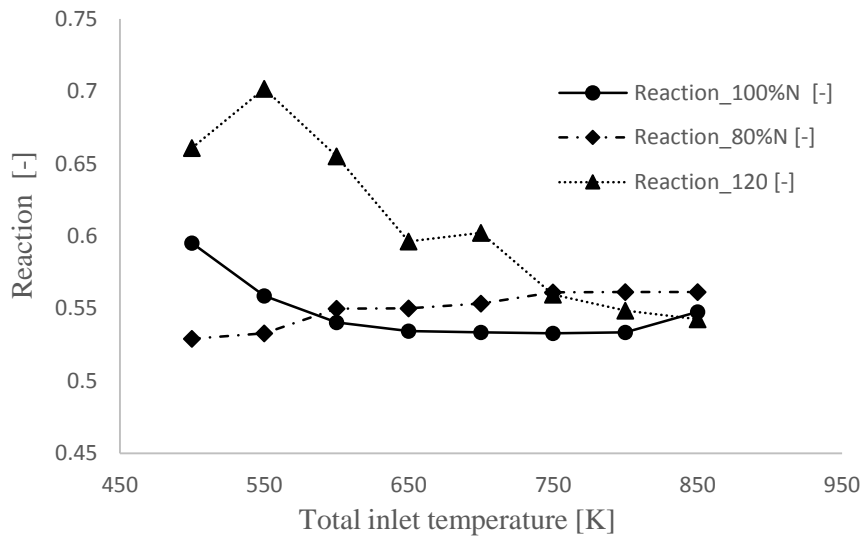


Figure 5.16: The effect of the total inlet temperature on the total to reaction at different rotational speeds  $N$ .

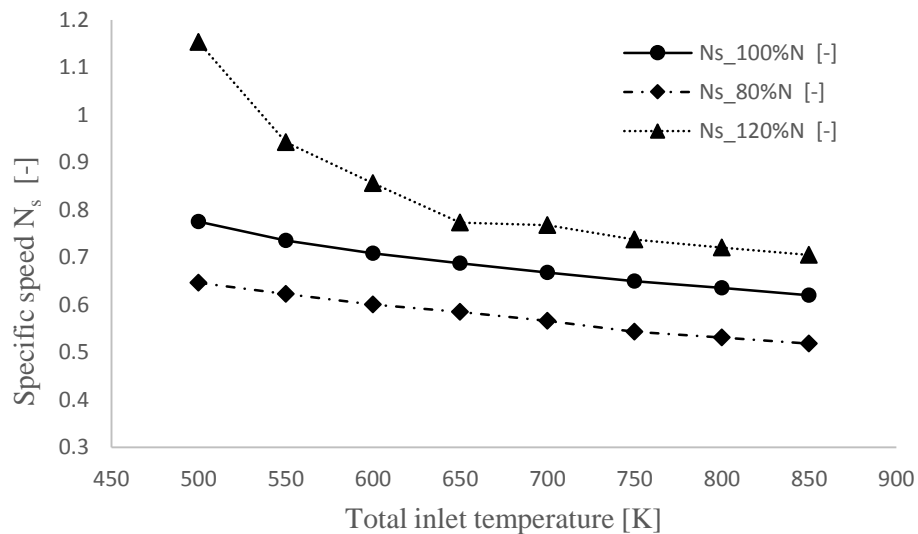


Figure 5.17: The effect of the total inlet temperature on the specific speed  $N_s$  at different rotational speed  $N$ .

The dimensionless specific speed  $N_s$  and the specific diameter  $D_s$  are the most important parameters in characterizing the performance of the radial inflow turbine. As mentioned in BALJE [15] and later in WHITFIELD [104], the recommended range of the specific speed is between 0.45 -0.8, and as shown in the figure 5.17, the turbine at the nominal speed can handle the range of temperature variations and keep the specific speed within

the recommended range. However, at off-design rotational speed, the turbine efficiency and the performance become more sensitive to the total inlet temperature variation and slip away from the recommended values. The recommended value of  $D_s$ , as mentioned in BALJE [15], is in the range of 2.5-5. The sensitivity of the specific diameter to the temperature over the tested range, behaves similar to the specific speed but the values still within the recommended range as shown the figure 5.18 below.

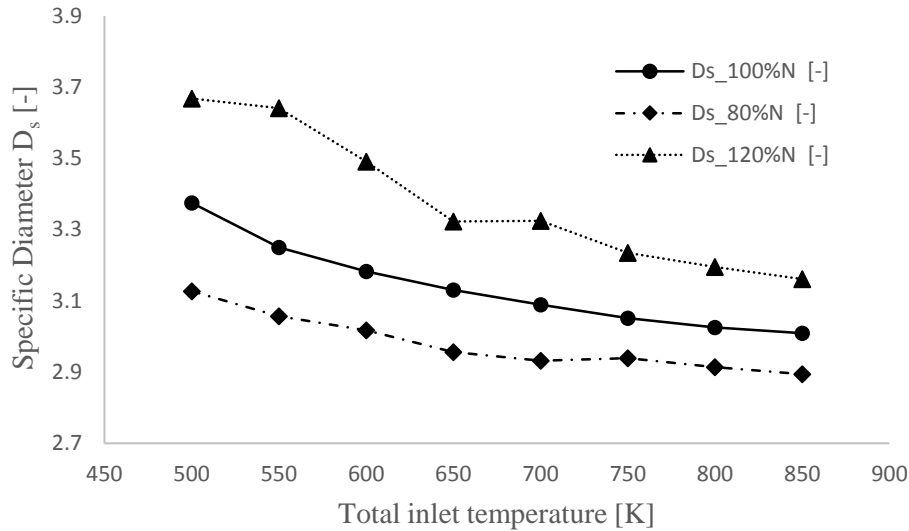


Figure 5.18: The effect of the total inlet temperature on the specific diameter  $D_s$  at different rotational speed  $N$ .

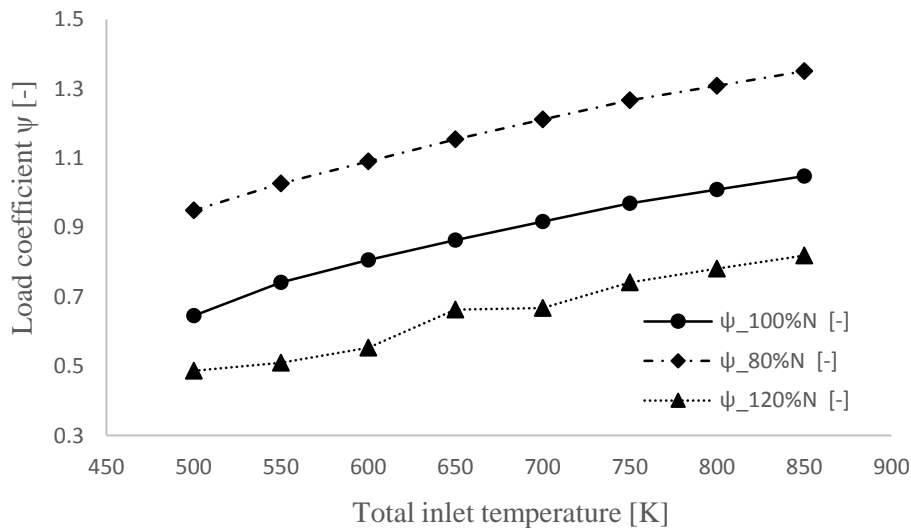


Figure 5.19: The effect of the total inlet temperature on the load coefficient at different rotational speed  $N$ .



As shown in the equation 4.6, the loading coefficient,  $\psi$ , may depend solely on the circumferential velocity at the rotor inlet  $C_{04}$ , and the rotor tip velocity  $U_4$ , since the ratio of the circumferential velocity at the rotor exit to the rotor inlet tip velocity  $U_4$  is negligibly small at the design point. The figure 5.19 shows that the effect on the loading coefficient when the turbine operates at rotational speed different from the nominal one, is more than the effect of the temperature, i.e. the loading coefficient is more sensitive to the change in rotational speed than the inlet temperature change, which complies with the equation 4.6. Where the recommended values of the loading coefficient, as in ROHLIK [85], is in the range of 0.7-0.9.

The flow coefficient,  $\phi$ , as shown in the figure 5.20 below behaves almost similar to the behavior of the load coefficient. However, the variation of the flow coefficient over the tested range of the total inlet velocity at the nominal rotational speed is 0.1507. It is clear for the figure 5.20 below, that the turbine at the nominal speed can handle a wide range of inlet temperature and still within the recommended range of the flow coefficient by ROHLIK [85], which is between 0.15-0.35 at the optimum efficiency, and that means that the sensitivity of the flow coefficient to the inlet total temperature variation is relatively low.

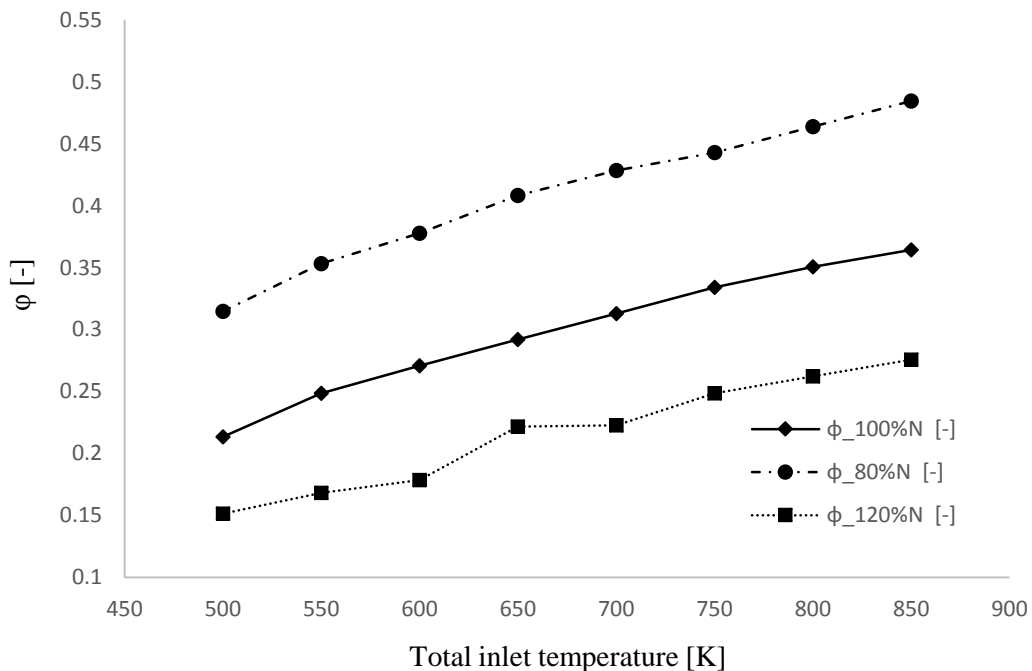


Figure 5.20: The effect of the total inlet temperature on the flow coefficient  $\psi$  at different rotational speed  $N$ .

Zero swirl at the rotor exit is normally assumed at the optimum efficiency i.e. zero degree of the exit flow angle ( $\alpha_5$ ). However, taking into consideration the component downstream the rotor, which is sometimes a simple exhaust diffuser, some swirl value is recommended to enhance the highly energized boundary layer and protect the flow from being separated in this negative pressure-gradient flow component. The sensitivity of the rotor exit flow angle ( $\alpha_5$ ) to the inlet temperature, is more at speed values higher than the nominal speed, 120% in this case, but the sensitivity of the speed lower than the nominal speed is similar to that of the nominal speed, as shown in the figure 5.21 below.

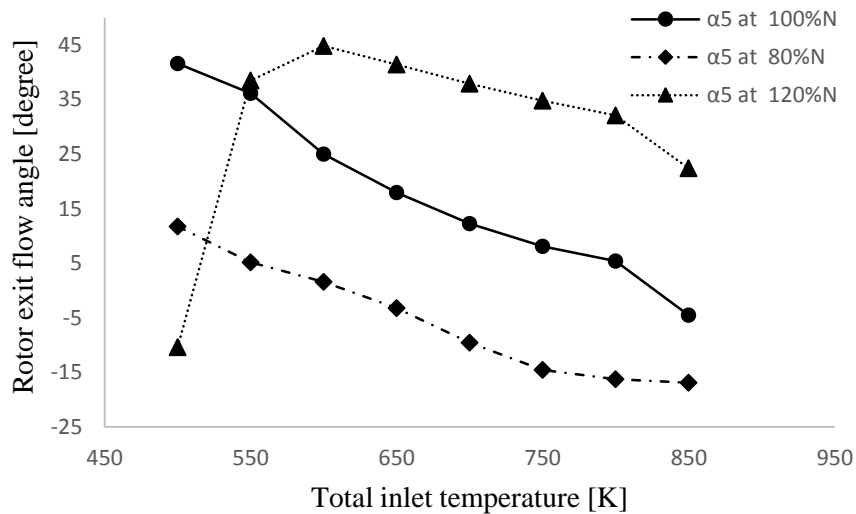


Figure 5.21: The effect of the total inlet temperature on rotor exit flow angle  $\alpha_5$  at different rotational speed  $N$ .

From Euler's equation of turbomachinery, a negative difference velocity at the exit of the turbine rotor is recommended and it increases the specific power produced. WHITFIELD and BAINES [104] made an extensive research for various turbines at different operating conditions, and recommended a value between  $-55^\circ$  to  $-70^\circ$  at the design conditions. The figure 5.22 shows that the values of  $\beta_5$  have low sensitivity to the inlet temperature and can handle a wide range.

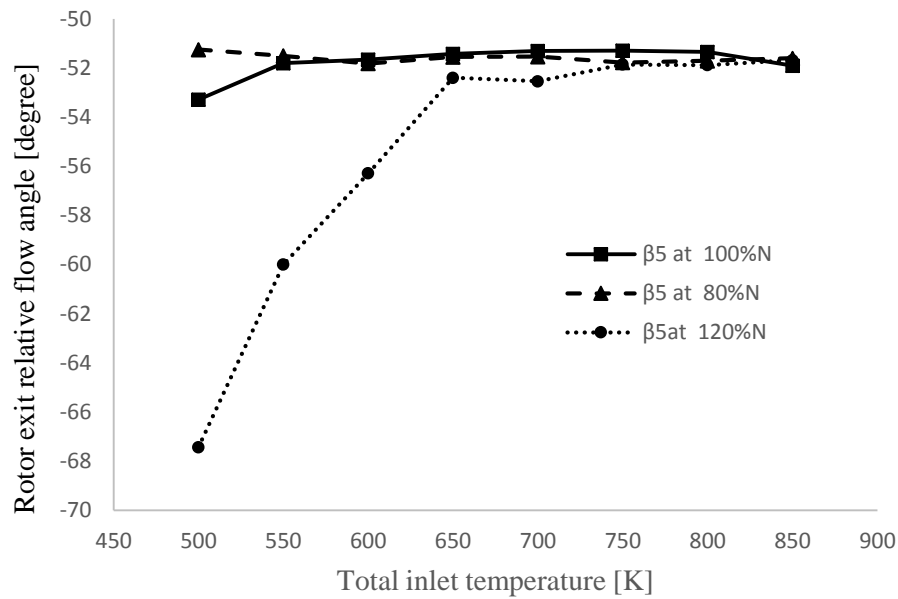


Figure 5.22: The effect of the total inlet temperature on rotor exit relative flow angle  $\beta_5$  at different rotational speeds  $N$ .

The figure 5.23 shows one of the most important design parameter in the radial turbine, which is the rotor relative inlet angle. The recommended value of it, has been reported by many researchers, DIXON [31] may have done the most notable work in this concern, and recommended the range of  $-20^\circ$  to  $-40^\circ$ . It is clear from the figure 5.23 that at the nominal speed the turbine behaves the best among all the operating speeds and its sensitivity is particularly low to the total inlet temperature.

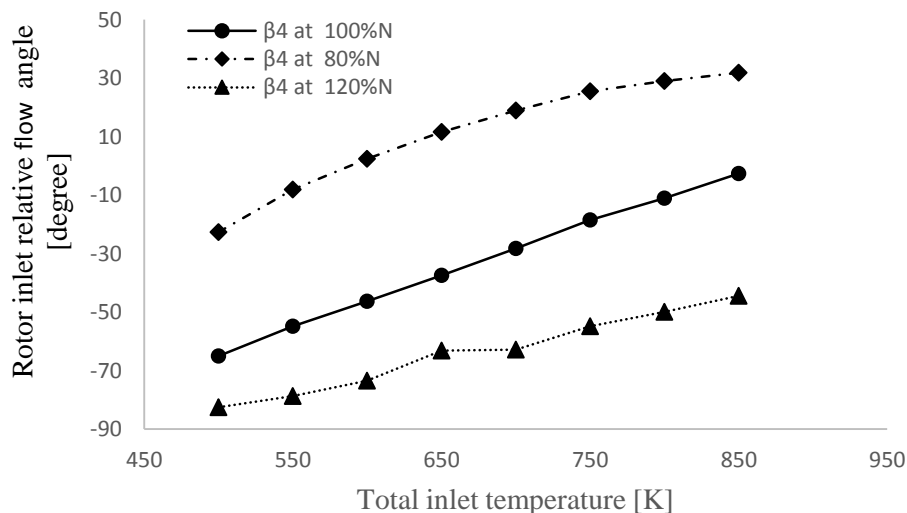


Figure 5.23: The effect of the total inlet temperature on rotor inlet relative flow angle  $\beta_4$  at different rotational speed  $N$ .

The velocity ratio,  $v$ , represented in the figure 5.24 below, shows that this parameter is within the recommended range, for the nominal speed and the lower speed, 80% of the nominal in this case. The recommended range as mentioned in BALJE [15] is between 0.55 and 0.8.

The velocity ratio represents the ratio of the rotor tip velocity to the spouting velocity, which can be also empirically estimated from the equation 4.4, and as mentioned in AUNGIER [8], it has been shown that the velocity ratio depends solely on the specific speed of the radial turbine.

Where the velocity ratio given as follows

$$v = \frac{U_4}{C_o} \quad (5.1)$$

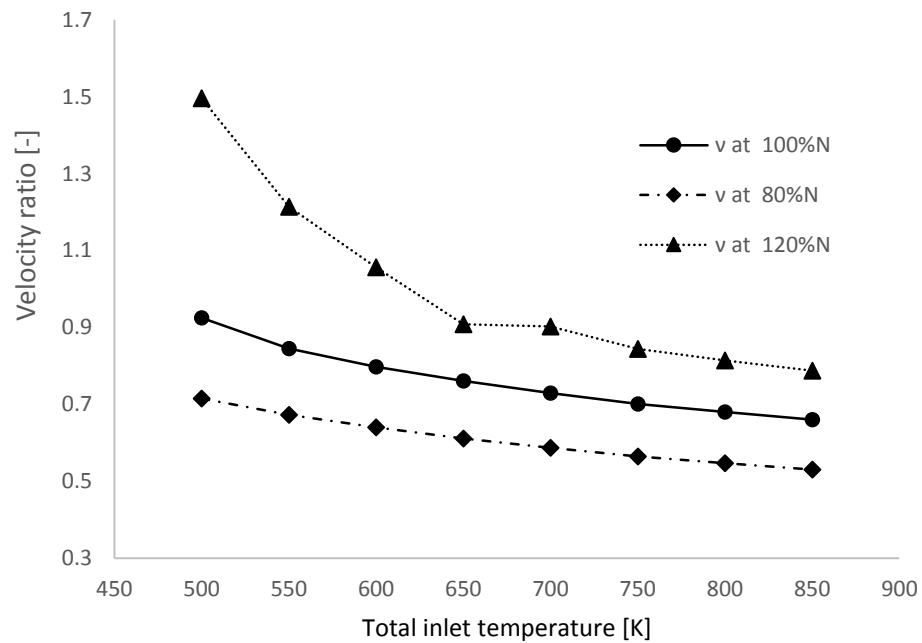


Figure 5.24: The effect of the total inlet temperature on the velocity ratio  $v$  at different rotational speeds  $N$ .

## 5.6 Blade Number Effect

The blade number effect on the radial inflow turbine performance has been studied by many turbomachinery researchers. Correlations have been proposed and examined. Selecting an appropriate number of blades for both, the stator and the rotor, has to take in mind that blade blockage is increased with increasing the number of blades but at the other hand we get a relatively uniform flow and blade loading. Choosing lesser number will lead to less blockage and hence less losses, but the flow will be less uniform. GLOSSMAN has proposed an empirical correlation to determine the minimum number of rotor blades required for calculating the passage losses and the incidence as shown in equation (4.23) above. ROHLIK [85] has also modified equation (4.46) for the optimum number of blades derived from the graph proposed by JAMIESON [52].

The figures 5.25, 5.26 and 5.27 show the static pressure at 25%, mid and 75% rotor span-wide positions, and for different numbers of rotor blades, respectively.

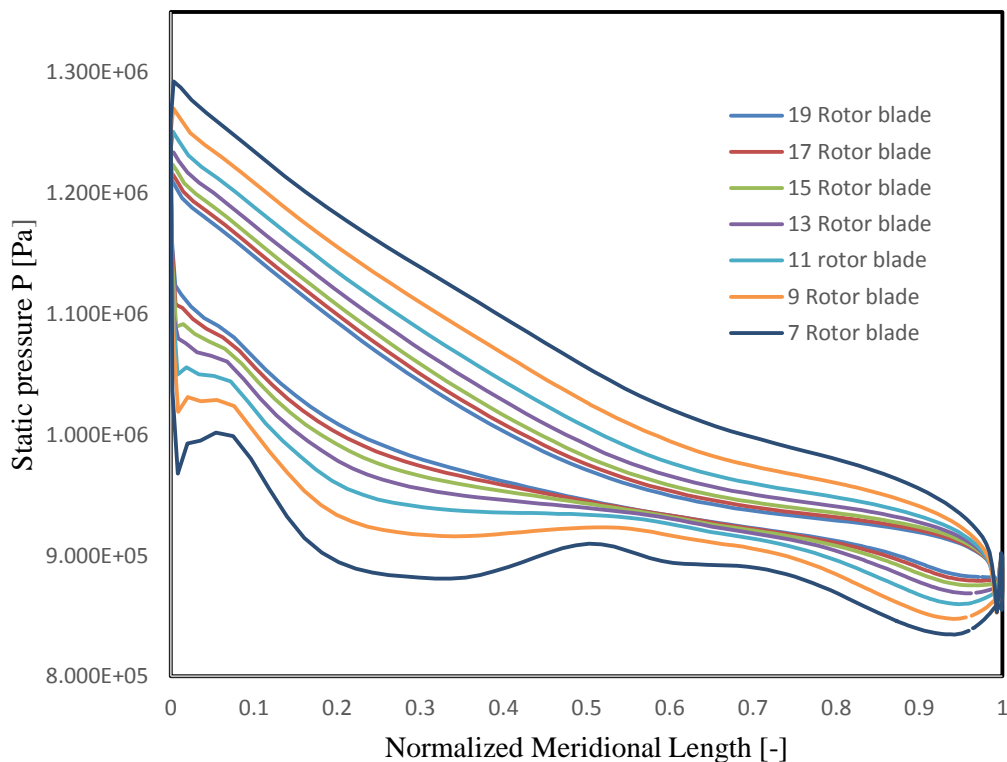


Figure 5.25: The blade loading, Static pressure  $P$  for different numbers of rotor blade at 50% span.

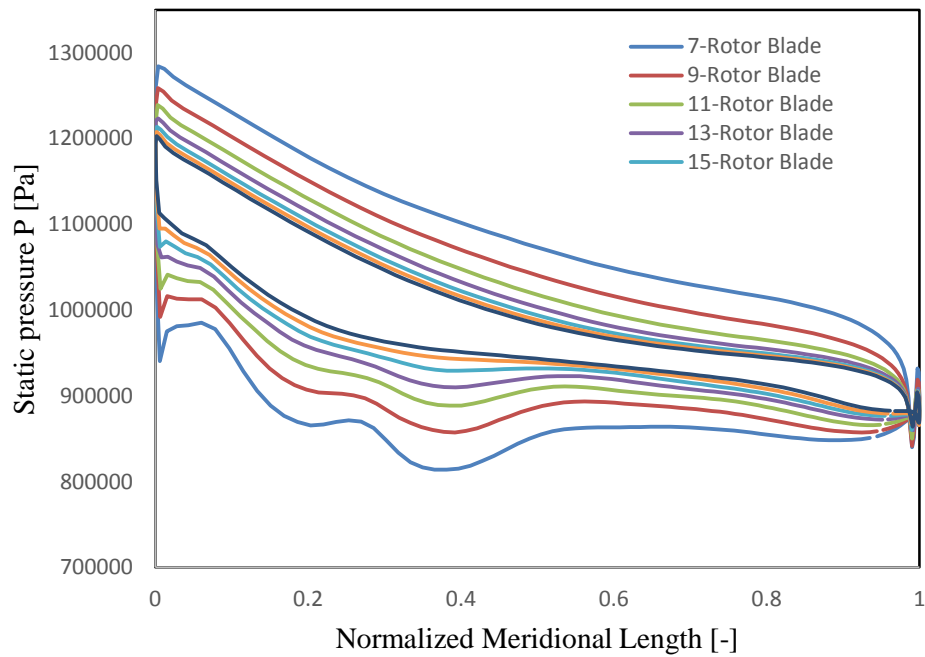


Figure 5.26: The blade loading, Static pressure  $P$  for different numbers of rotor blade at 75% span.

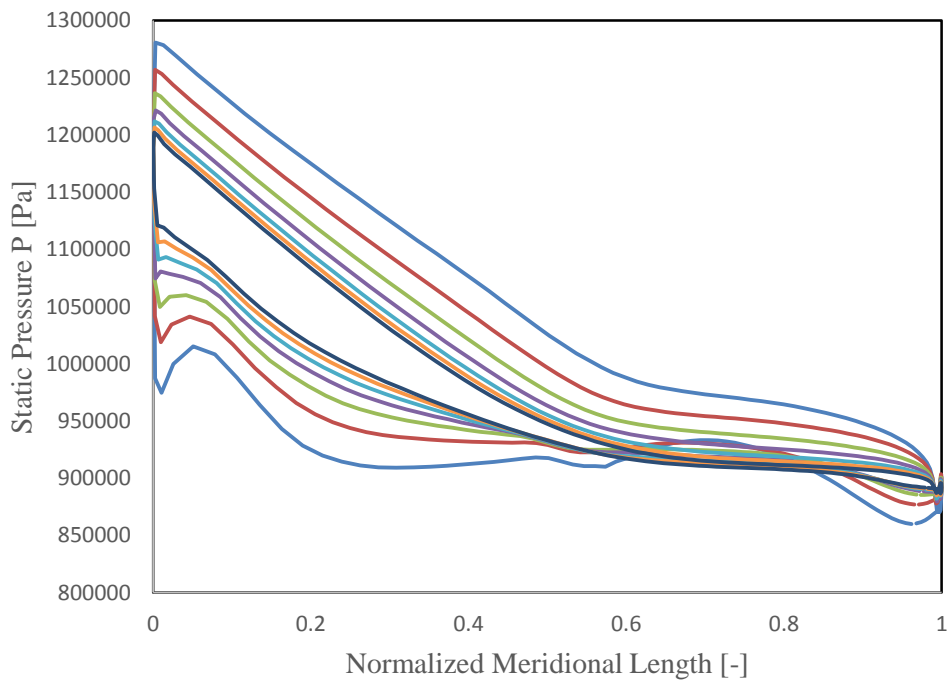


Figure 5.27: The blade loading, Static pressure  $P$  for different numbers of rotor blade at 25% span.

### 5.6.1 Rotor Inlet Width Estimation

Using the equation 4.47, the rotor inlet blade width can be calculated. WHITFIELD and BAINES [104], DIXON [31] and ROHLIK [85] have proposed a dimensionless ratio, which relates the rotor inlet width to the rotor inlet diameter  $b/D_4$ . The recommended value of this ratio is between 0.05 and 0.15. A value within this range offers a good compromise between turbine performance, the blockage and mass flow rate capacity.

We run the simulation for  $b/D_4$  between 0.0714 and 0.19 and keeping the other geometrical parameters and the boundary conditions constants. It is clear from the figures 5.28, 5.29 and 5.30 that the relative and the absolute Mach number increase by increasing the blade inlet width. This increasing can be attributed to the increasing of the mass flow rate.

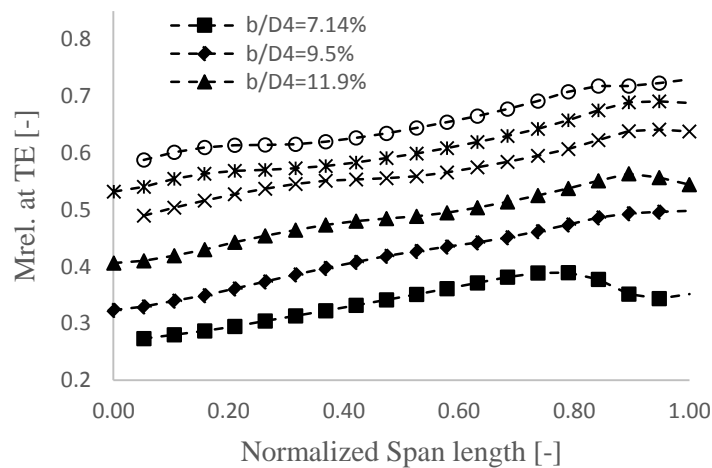


Figure 5.28: Relative Mach number  $M_{rel}$  at the rotor trailing edge vs. normalized span length.

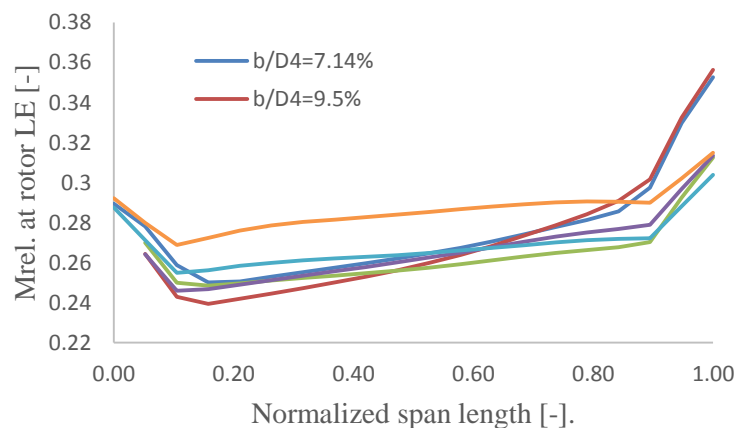


Figure 5.29: Relative Mach number  $M_{rel}$  at the rotor leading edge vs. normalized span length.

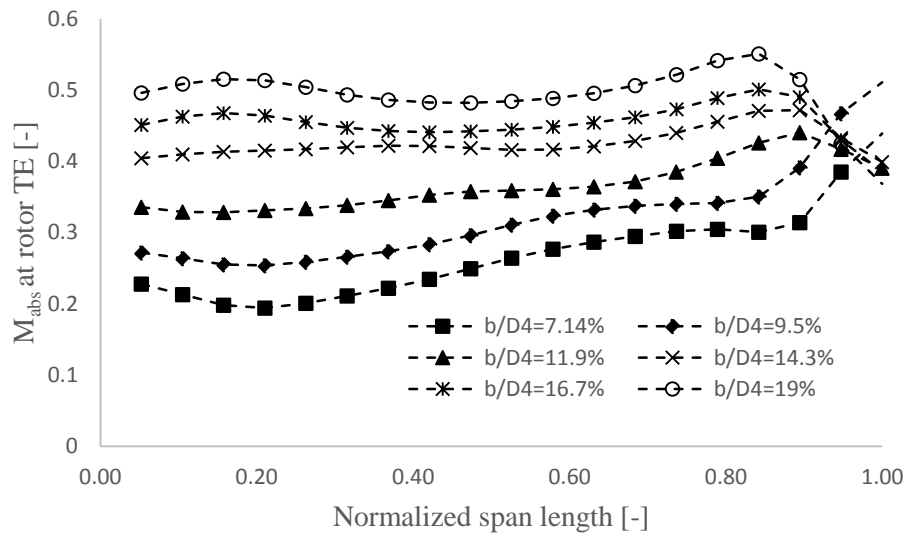


Figure 5.30: Absolute Mach number  $M_{rel}$  at the rotor trailing edge vs. normalized span length.

The relative flow angle at the rotor exit is also plotted for a different values of  $b/D_4$ , as shown in the figure 5.31 below. We can see that the relative angle also increase with increasing the rotor inlet width. For a normalized span-width between 10% and 95%, the relative angle can handle the variation of the blade inlet width and stay within the recommended value of  $\beta_5$ .

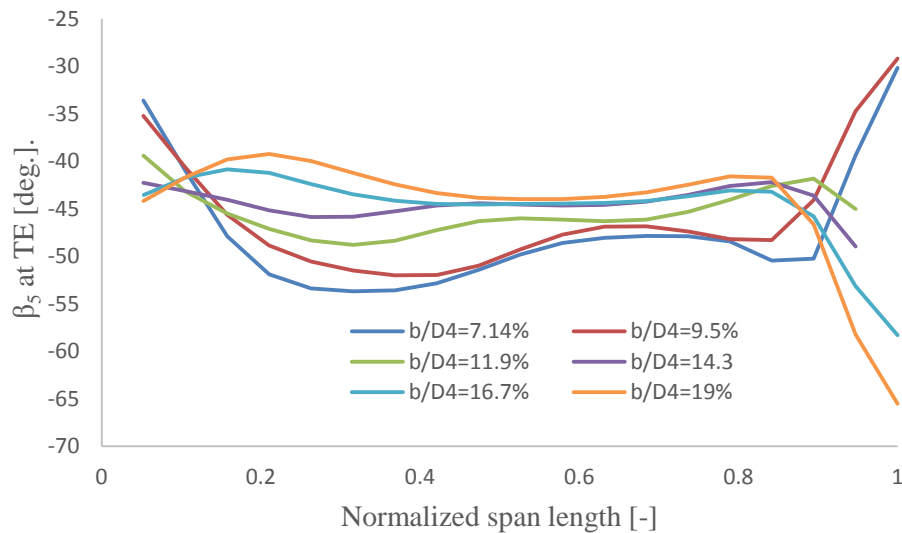


Figure 5.31: Relative flow angle at the rotor trailing edge vs. normalized span length.



The total-to-static efficiency to the reference total-to-static efficiency  $\eta_{ts}/\eta_{ts.ref.}$  has been graphically expressed in the figure 5.32 below, for the same range of the rotor inlet width ratio. It can be seen that the efficiency decreases at blade width different from that of nominal one, which we chose it to be 0.095 in this case.

The figure 5.33, represents the effect of the rotor inlet width on the absolute flow angle at the trailing-edge  $\alpha_5$ , it shows that the value of the angle decreases with increasing the blade width.

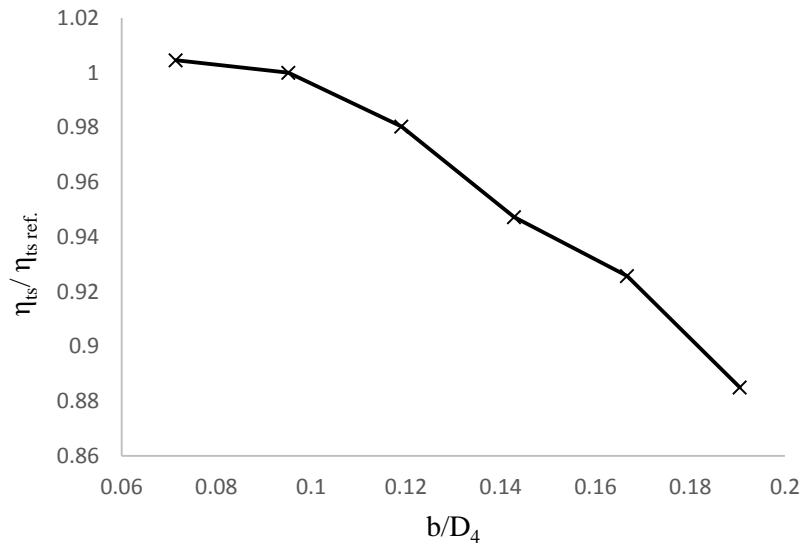


Figure 5.32: Effect of the relative inlet width on the relative total to static efficiency.

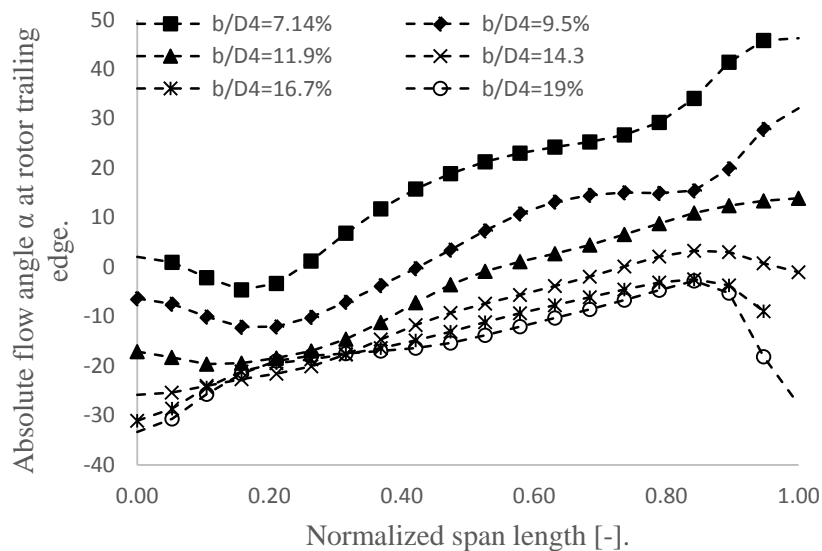


Figure 5.33: Absolute flow angle at the rotor trailing edge vs the normalized blade span length.

The effect of changing the rotor inlet blade width on the blade loading has been also graphically expressed in the figure 5.34 below and for different positions of the normalized span-wise, 25%, 50% and 75% in this case. The blade loading and for the all positions of the span is seemed to be more stable for the values of  $b/D_4$  between 0.0714 and 0.145, which almost agrees with the recommended values by the authors mentioned above.

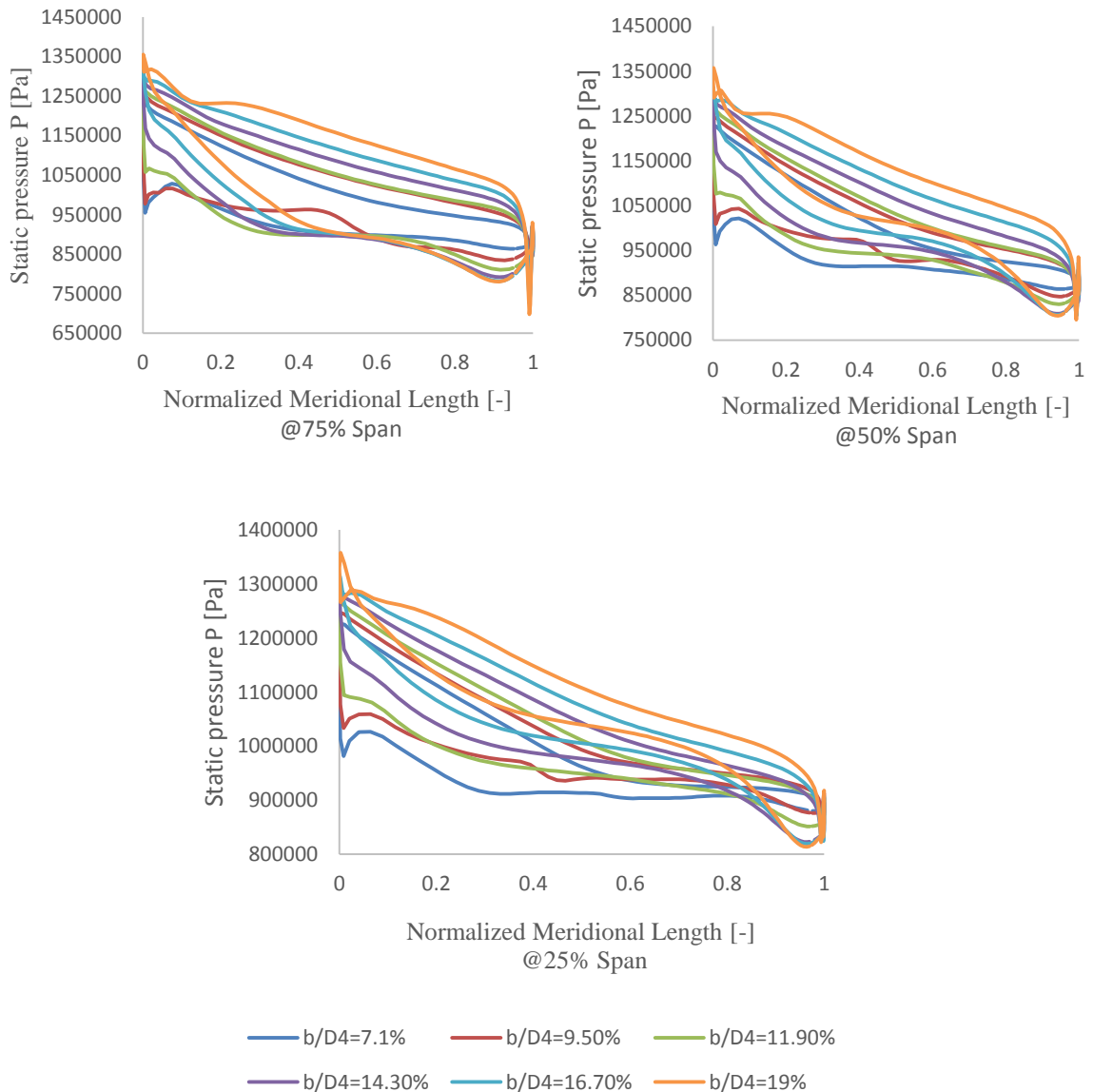


Figure 5.34: Static pressure  $P$  versus normalized meridional length for different span positions with relative blade width  $d/D_4$  as parameter.

### 5.6.2 The Vane Solidity in the Radial Inflow Turbine Stator

As we mentioned in the previous chapter, the nozzle row is needed to accelerate the flow, i.e. increasing the kinetic energy of the flow, and also to deliver the flow to the rotor at specified angle. Generally, the radial inflow turbine doesn't require a complex geometry nozzle, a nozzle without or with a little camber can be sufficient. In the turbochargers, the designers didn't have to use a nozzle row at all, as the direct flow from the exhaust manifold contains energy much more than the energy required to run the compressor, and thus losses area acceptable with saving additional costs of the nozzle row manufacturing.

The number of the nozzle vanes has to be chosen in a way that offers a compromise between the metal blockage and the uniformity of the flow and also not to let the resonance with blade rotor possible. Sometimes it is recommended to have a prime number of the nozzle vanes. Different numbers of the nozzle vanes have been chosen, and the effect of the numbers on different performance parameters has been investigated and the results have been graphically shown. We chose odd numbers from 11 to 21.

The nozzle loss coefficient  $\lambda_N$  is shown in the figure 5.35 below and it is obvious that the loss coefficient increases by increasing the number of the nozzle vanes. This increment is attributed to the increasing wetted area of the nozzle row. BALJI [15] has recommended a range for the nozzle loss coefficient which is between 0.06 and 0.24. The figure 5.35 shows that  $\lambda_N$  is acceptable and within the recommended range until 17 nozzle blades.

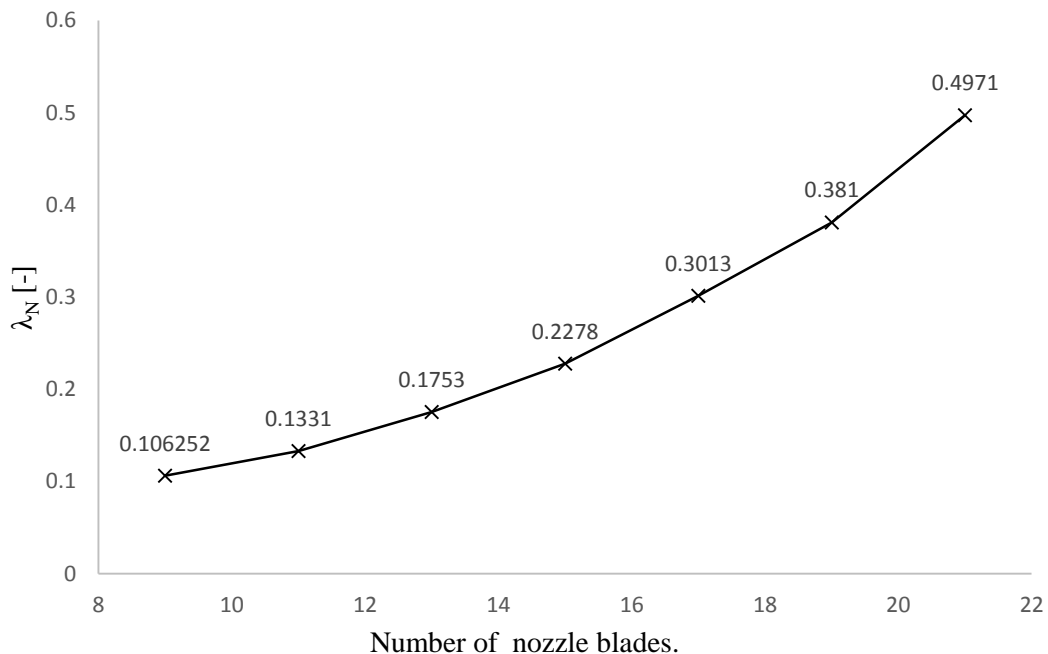
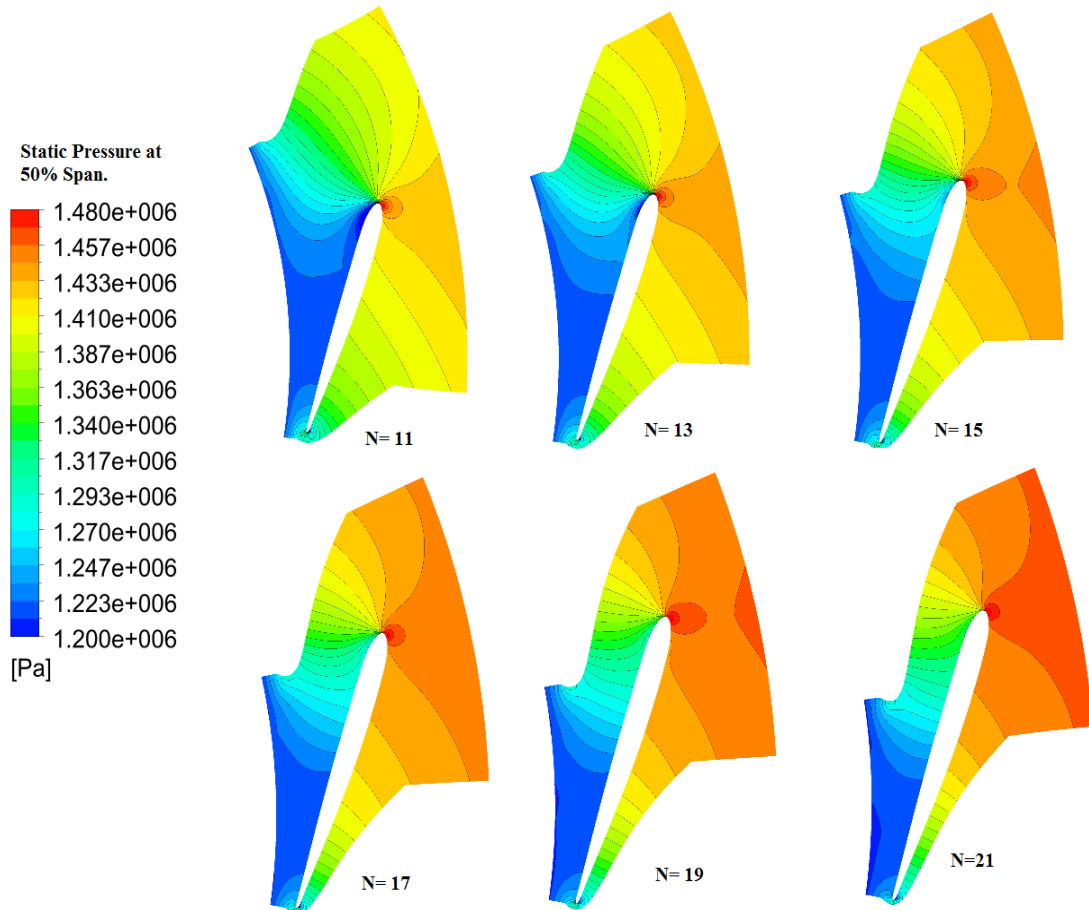


Figure 5.35: The effect of the number of nozzle blades on the nozzle loss coefficient,  $\lambda_N$ .

The figure 3.36 shows the static pressure contour at 50% span-wide. The static pressure distribution from the nozzle leading-edge to the nozzle trailing-edge, at the trailing edge of the nozzle a wake flow can be noticed but it is also obvious that the wake is getting smaller with increasing the number of nozzle vanes.



*Figure 5.36: Iso-colour plots of the pressure distribution at 50% span for different number of nozzle blades.*

The figures 5.37, 5.38 and 5.39 shows the effect of the number of nozzle blades in combination with different number of rotor blades. The relative and absolute Mach number of the trailing and leading edge are plotted versus the normalized spanwise axes.

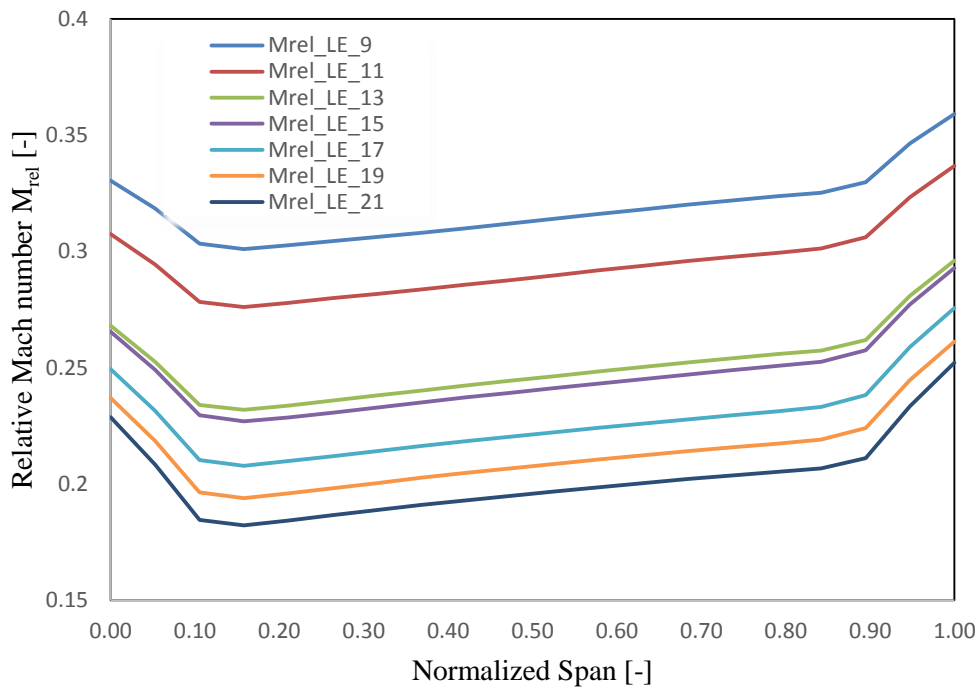


Figure 5.37: Relative Mach number  $M_{rel}$  at the rotor leading edge (LE) for different numbers of nozzle blades.

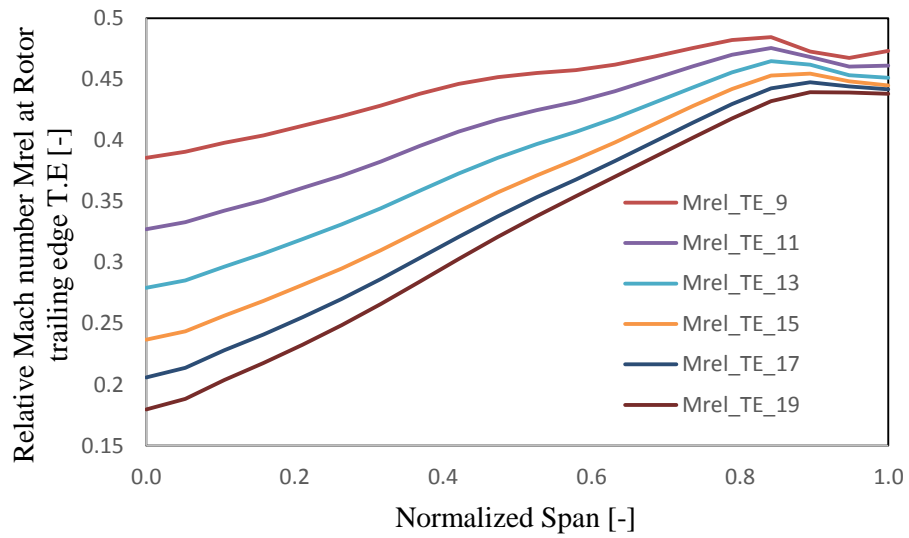


Figure 5.38: Relative Mach number  $M_{rel}$  at the rotor trailing edge (TE) for a different numbers of nozzle blades.

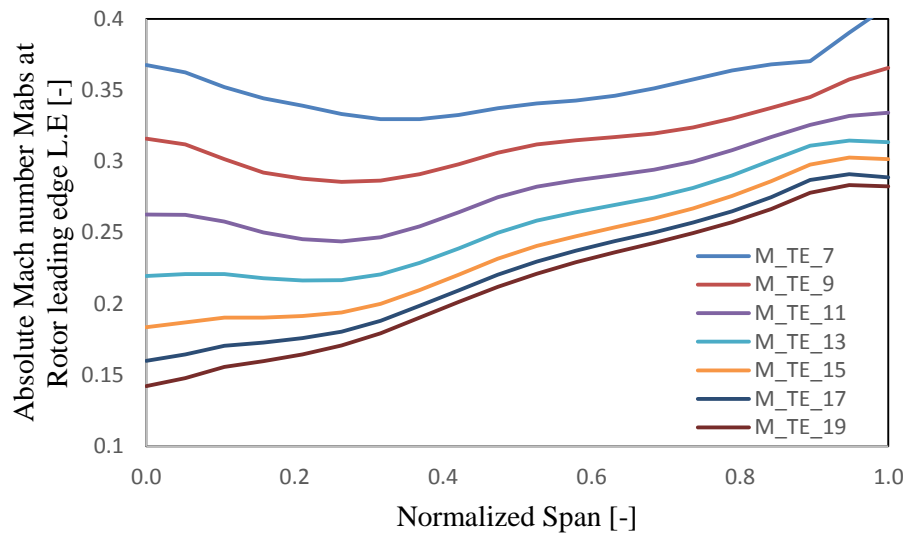


Figure 5.39: Absolute Mach number  $M_{abs}$  at the rotor leading edge LE for a different numbers of nozzle blades.

## 5.7 Estimating the Interspace Distance.

The vaneless space between the nozzle vane trailing edge and the rotor blade leading edge has a significant effect on the aerodynamic performance of the radial inflow turbine. Increasing the vaneless distance leads to a more aerodynamically efficient design and a more circumferentially uniform flow state around the rotor periphery, but on the other hand, the longer vaneless space distance we insert, the more wetted surface area will be and then the more frictional losses the turbine will have due to the long flow path. But with a shorter vaneless distance between the stator vane trailing edge and the rotor blade leading edge, the wakes and jets will not have enough space to mix out to the required extent and hence a higher level of nonuniformity entering the rotor is expected

Additional to the influence of the aerodynamic performance, it has impact on the structural behavior of the rotor introducing an alternate loading pattern as the rotor blade passes through a successive jets and wakes, said SIMPSON [93].

TUNAKOV [100] investigated the effect of the vaneless space and suggested that the optimum clearance should represent the compromise between the frictional losses and the nonuniformity and suggested the following relationship

$$\frac{\Delta r}{b \sin \alpha_4} \quad (5.2)$$

Where  $\Delta r$  is the vaneless radial distance,  $b$  is the rotor blade width and  $\alpha_4$  is the rotor inlet flow angle. RODGERS [84] mentioned that the interspace can have a significant impact on the turbine performance. WATANABE suggested also a relationship for estimating the ratio of the nozzle trailing edge to the rotor blade leading edge which has been chosen as a parameter ( $r_3/r_4$ )

$$\frac{r_3}{r_4} = 1 + 2b \sin\alpha_4/r_4 \quad (5.3)$$

We have tested a four different vane space i.e. a different  $r_3/r_4$  ratio and compared to the baseline preliminary model which has ( $r_3/r_4 = 1.095$ ).

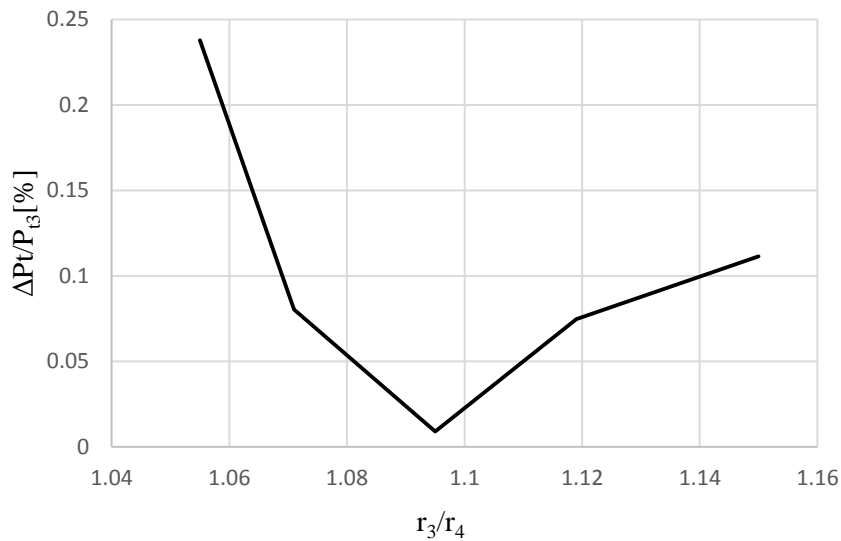


*Figure 5.40: Normalized total pressure losses  $\Delta Pt/P_{13}$  versus the radius ratio of the nozzle trailing edge radius  $r_3$  and the ratio inlet radius  $r_4$ .*

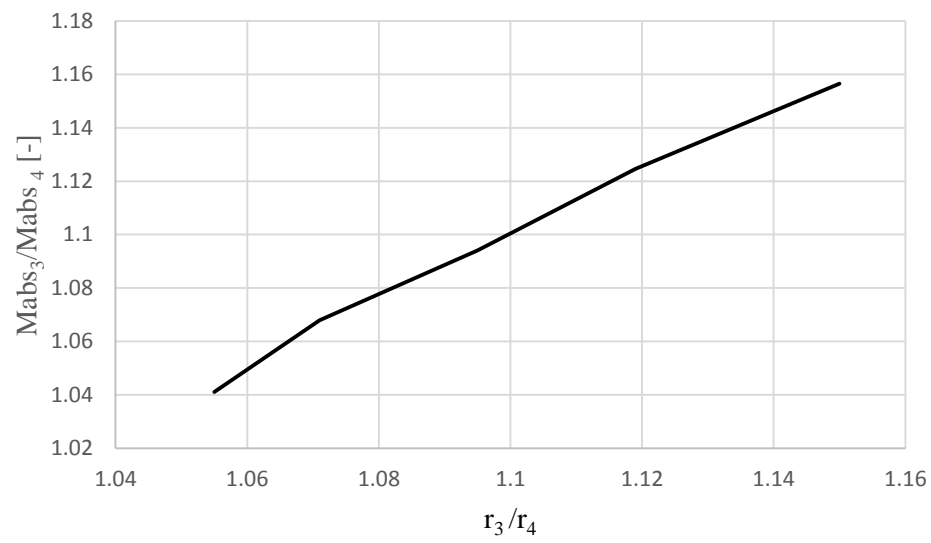


*Figure 5.41: Ratio of the absolute Mach number of the nozzle outlet  $M_{abs\ 3}$  and the absolute Mach number at the rotor inlet  $M_{abs\ 4}$  versus the radius ratio  $r_3/r_4$ .*



## 6 Optimization a Radial Inflow Turbine

The optimization process of any application is the mathematical process through which the set of conditions that produces the optimum of a specified function is obtained.

Generally, any optimization problem consists of a set of design variables, objective function (or fitness function in the genetic algorithm) and constraints. In the course of obtaining the optimum solution the numerical values of the design variables are determined. The objective function is a mathematical expression that embodies the design variables that need to be maximized or minimized locally or globally, and the constraints are the conditions that have to be satisfied to achieve the optimization.

Several optimization methods have been developed over the past. However, the optimization methods can be globally distinguished as deterministic or stochastic algorithms. The deterministic algorithms behave predictably and give the same output for a particular input, whether the stochastic algorithms don't, and give different optimum output depend on the initial value and other parameters. The deterministic method can be further subdivided in gradient based and derivative free algorithms, while the stochastic can be divided into simulated annealing and evolutionary algorithms such as the genetic algorithm GA optimization method.

The DesignXploration DX is an optimization tool in Ansys Workbench, which consists of the response surface optimization, parameters correlation and the six sigma analysis SSA tools to explore the design space through exploring and understand the performance at other design or operating conditions. Finding the conditions which give the best performance, determine the key parameters influencing the design and explore the robustness of the design is also achieved.

In this chapter we will perform the optimization using two methods which are classified under the Goal Driven Optimization GDO, and they are the Multi-Objective Genetic Algorithm method MOGA and the Non-Linear Programming by Quadratic Lagrangian NLPQL, then we choose the candidate point from these methods as optimum design points.

## 6.1 Design of Experiments DOE method

DX uses a DOE to determine the location of sampling points and to select design points with parameter combinations intended to explore the solution space efficiently. The design of experiments method works best for fewer than 20 input parameters [6].

There are many types of DOE, such as Central Composite Design CCD, Optimal Space-Filling Design OSF, Box-Behnken Design, Sparse Grid Initialization and Latin Hypercube Sampling Design LHS.

In our sampling we chose the CCD, and the design type used is the auto defined which switches between the G-Optimal and the VIF-optimal, depends on the number of input variables. Rotatable (spherical) design is preferred if the above option doesn't provide a reasonable values of the goodness of fits from the response surface plotter. However, there are other criteria to consider for an optimal design setup [6]. In the table 6.1 below, the design points are listed based on the above criteria.

*Table 6.1: sample of the design Points in the Design of Experiments*

Name	Omega [radian s <sup>-1</sup> ]	Pt in [Pa]	Tt in [K]	Shaft Power [W]	$\eta$ t-s	$\beta$ 5	$\alpha$ 5	WR=W5/W4	CmR=Cm5/Cm4	$\beta$ 5
1	-13100	1475000	650	21613.4	0.866885	-28.6473	16.6126	1.45381	1.23673	-45.644
2	-14410	1475000	650	18050.9	0.85331	-50.3038	31.8576	1.04161	1.17329	44.7047
3	-11790	1475000	650	22856.7	0.852207	-8.46201	5.47714	1.63988	1.23114	45.5712
4	-13100	1350000	650	11625.5	0.821266	-55.1681	36.1564	0.955653	1.21943	42.1023
5	-13100	1600000	650	30658.4	0.859804	-9.32449	6.41589	1.6182	1.21796	45.6461
6	-13100	1475000	585	19493.1	0.870865	-39.8465	27.1199	1.22175	1.20433	45.2534
7	-13100	1475000	715	23853	0.860586	-17.706	9.73373	1.59139	1.23399	45.6914
8	-14165.1	1373371	597.1528	8980.6	0.760248	-68.8024	50.3505	0.636792	1.09899	46.0248
9	-12034.9	1373371	597.1528	14429.1	0.865008	-40.6747	26.589	1.22314	1.22199	45.3532
10	-14165.1	1576629	597.1528	25284.6	0.871694	-37.6343	24.7598	1.27671	1.21219	45.4862
11	-12034.9	1576629	597.1528	27904.4	0.856988	-6.07413	4.57819	1.65563	1.23657	-45.709
12	-14165.1	1373371	702.8472	12787.3	0.813664	-56.7838	37.007	0.934468	1.22332	41.4902
13	-12034.9	1373371	702.8472	17368	0.862899	-21.6128	12.1715	1.54933	1.23525	45.6974
14	-14165.1	1576629	702.8472	29690.9	0.861797	-19.6792	10.7911	1.57698	1.23695	45.7841
15	-12034.9	1576629	702.8472	30749.8	0.833781	11.4937	-1.23323	1.60414	1.21255	45.8769

In the DX optimization we used seven output parameter and three input parameters as we can see in the table above. For the sake of clarity we used a parameter key names to represent them in the various analysis and optimization processes, as shown in the table 6.2 below.

Table 6.2: The keys of the parameters used in the DX optimization.

Parameter	P2	P6	P9	P10	P11	P12	P13	P14	P15	P16
Property	Shaft Power [W]	$\eta_{t-s}$ [-]	$\beta_4$ [degree]	$\alpha_5$ [degree]	WR [-]	CmR [-]	$\beta_5$ [degree]	$\omega$ radian s <sup>-1</sup>	P <sub>t in</sub> [Pa]	T <sub>t in</sub> [K]

The design points are then plotted and graphically displayed as a DOE matrix representation of the generated design parameters, as shown in the figure 6.1 below. The parallel Y axes represent each parameter value.

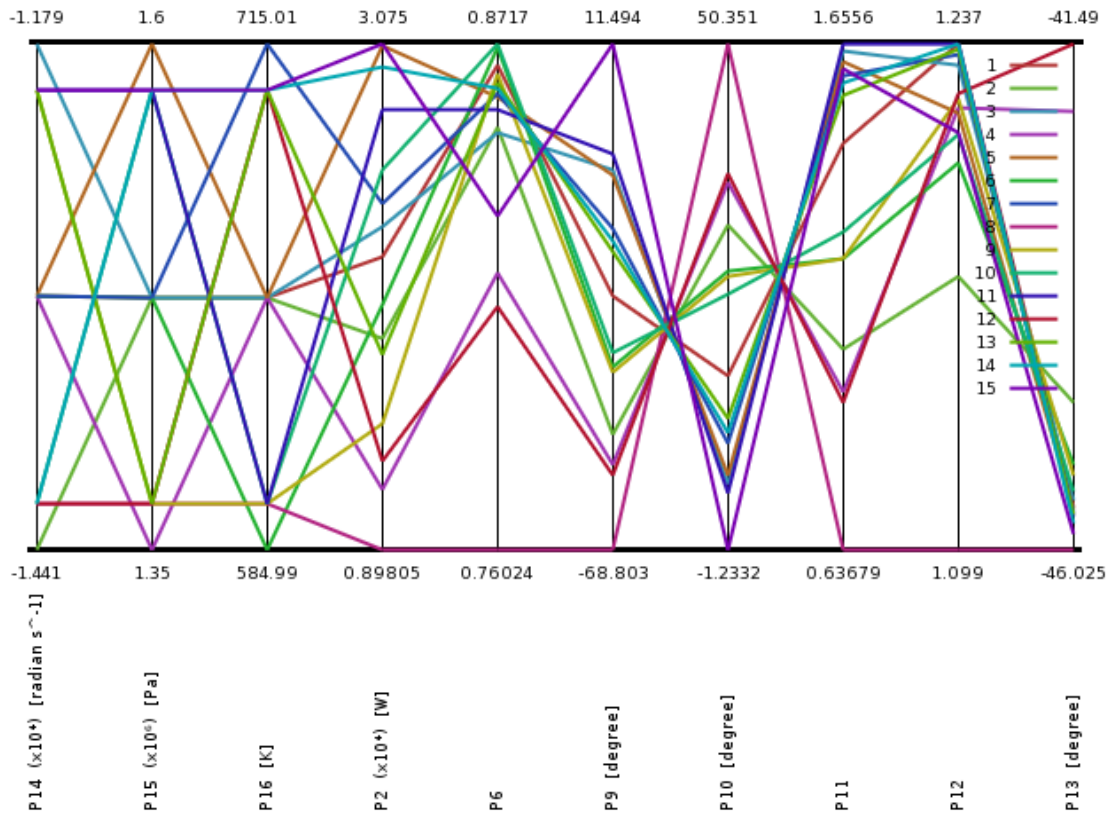


Figure 6.1: Parameters parallel chart.

The Goodness of Fit of the output parameters shown in the figure 6.2 below. The Goodness of Fit related closely to the meta-model used in the response surface. It is clear that the shaft power prediction from the design points is very close to those predicted from the response surface, but the total-to-static efficiency diviates a little bit more also the other parameters can be observed in the figure below.

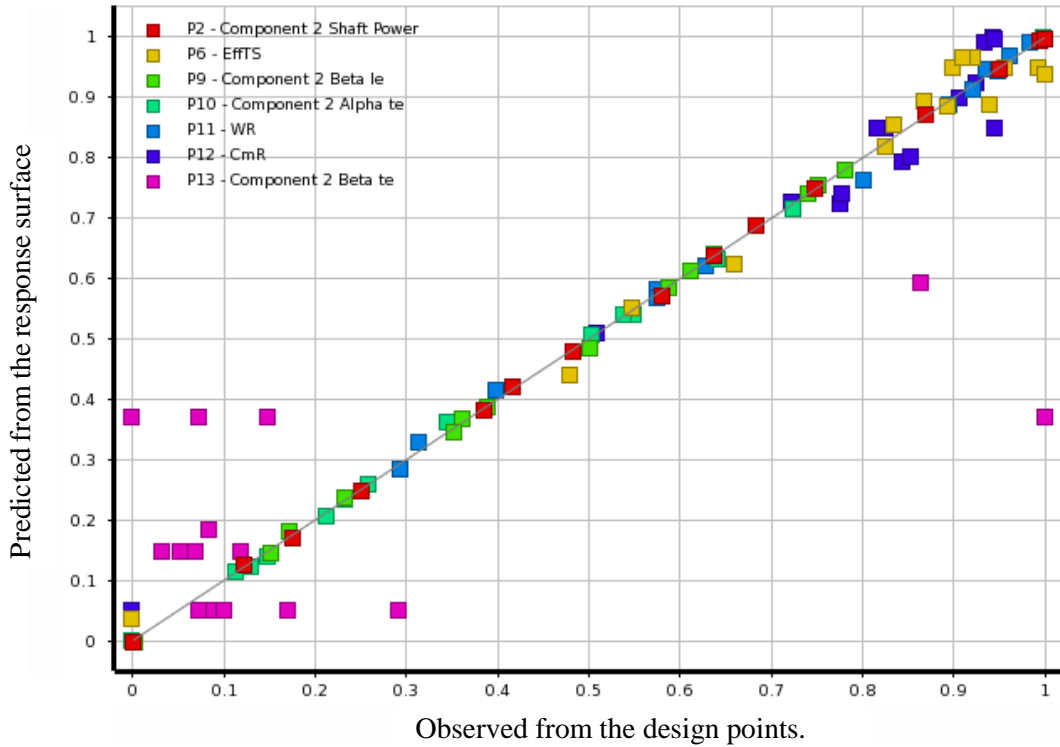


Figure 6.2: Goodness of Fit predicted from the Response Surface versus the goodness observed from the design points.

### 6.1.1 Response Surface

Creating a response surface is generally done by solving the the output parameters for all design points as defines by th DOS and the then fitting the output parameters as a function of the input parameters using regression analysis techniques. There are several modelling algorithm to create the response surface, such as the Full 2<sup>nd</sup> order polynomial, Kriging, non-parametric regression and neural network, as explained in [6].

The impact of each parameter on one another is shown in the 3-D response surface charts shown in the figure 6.3 below. From the graphs we can analyse and find the value of the parameter that maximizes or minimizes the output parameter. In this figure the impact of the total inlet pressure and temperature on the total-to-static efficiency and the ratio of the relative velocity WR at the leadign and at the trailing edge of the rotor is shown. Also the

effect of the rotational speed on the efficiency is drawn, and so on we can analyse the other input and output parameters.

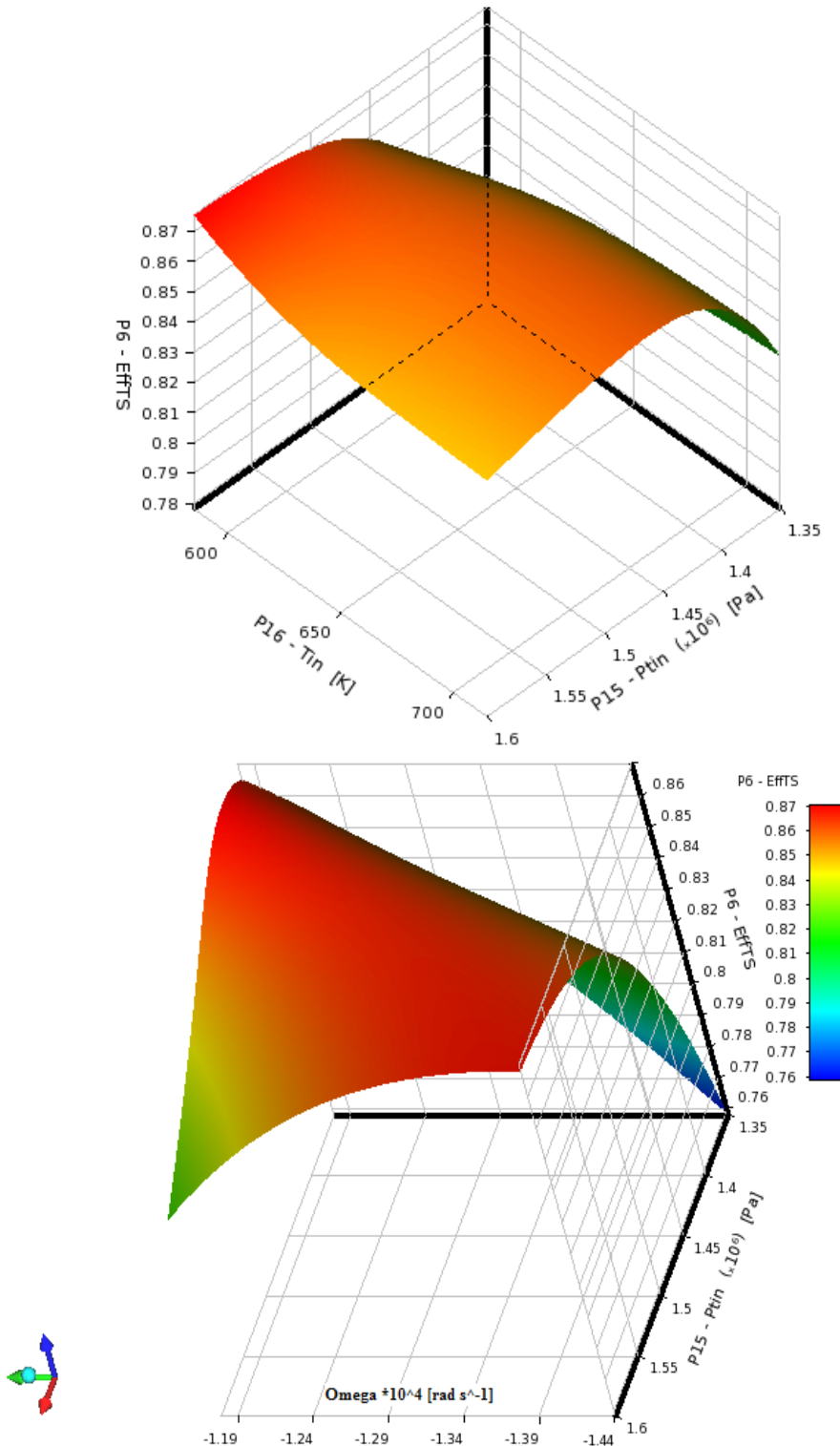


Figure 6.3: 3D response chart for the  $\eta_{t-s}$  vs. the total inlet pressure and temperature and  $\omega$ . Also  $\eta_{t-s}$  vs. total inlet pressure and temperature.

A 2-D response surface for the rotational speed  $\omega$ , and the total inlet pressure is also shown in the figure 6.4 and figure 6.5 below. In the figure 6.5 the design points from the DOE are also shown together with the response surface and the difference can be noticed. The maximum achievable total-to-static efficiency  $\eta_{t-s}$ , related to the input parameters  $P_{t \text{ in}}$  and rotational speed can then be easily assessed.

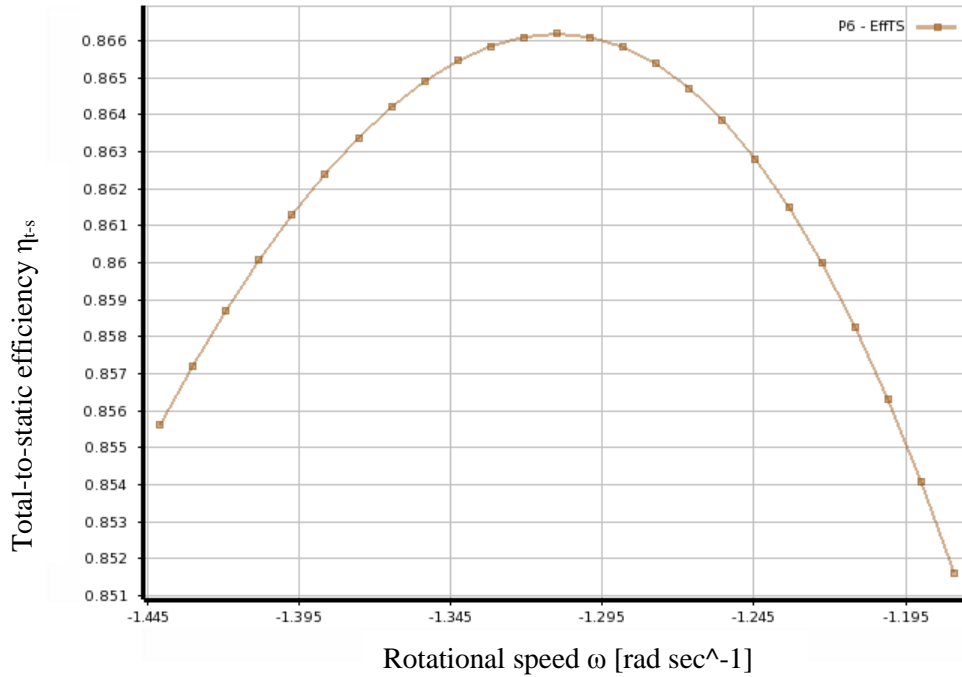


Figure 6.4: 2D response surface of the  $\eta_{t-s}$  vs.  $\omega$ .

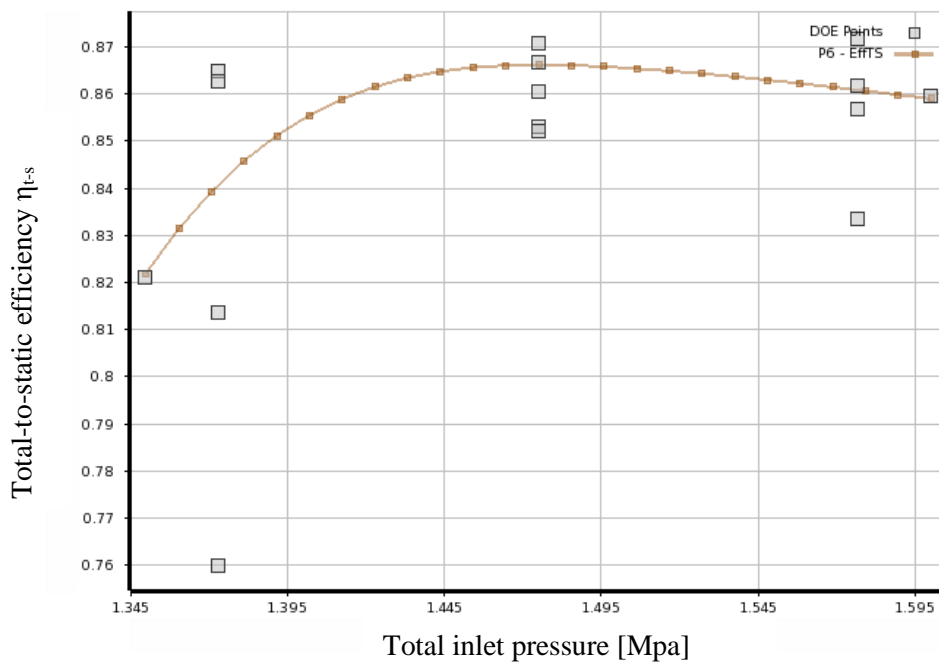


Figure 6.5: 2D response surface of the  $\eta_{t-s}$  vs  $P_{t \text{ in}}$ , with the DOE points.

Different types of algorithm can be employed to produce the response surface. The full 2<sup>nd</sup> Order Polynomial and the Neural Network are very close in producing the response surface as we can see in the figures 6.6 and 6.7. Other types are also plotted such as the Kriging and the Non-Parametric Regression.

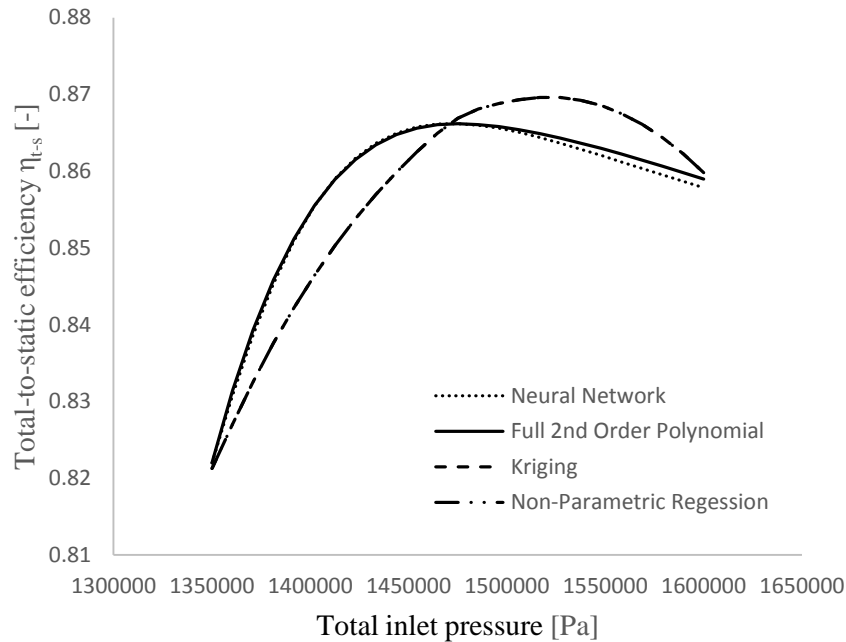


Figure 6.6: The Response Surface of the total-to-static efficiency  $\eta_{t-s}$  versus the  $P_t$  in for different algorithm types.

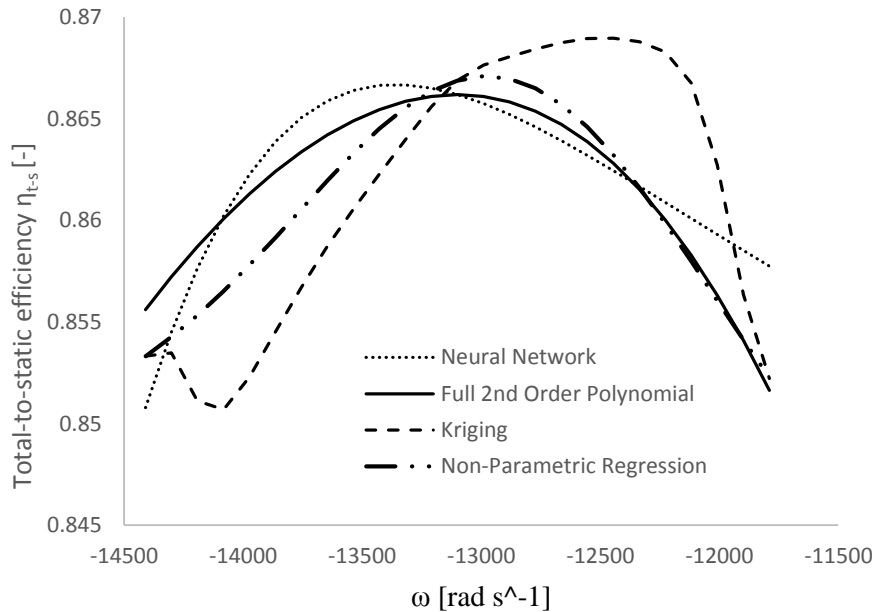
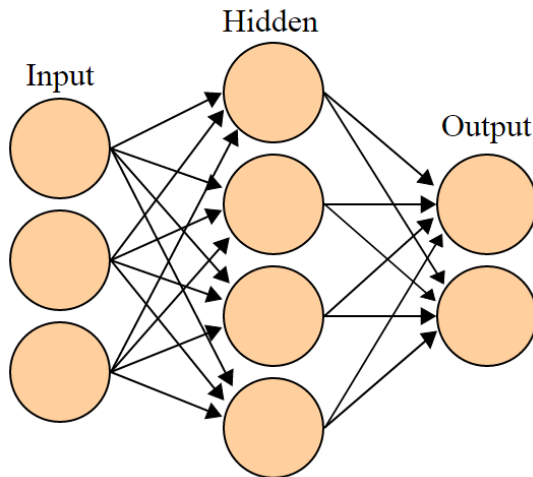


Figure 6.7: Response Surface of the  $\eta_{t-s}$  to the  $P_{t in}$  by different algorithm types (The  $-ve$  sign refers to the direction of the rotation).

### 6.1.2 The Artificial Neural Network

The Artificial Neural Network ANN used here is a mathematical technique based on the neural network in the human brain, and it is a statistical learning model used to estimate or approximate function. The ANN is an interconnected group of nodes akin the neurons in the brain as shown in the figure below.



It, generally, consists of many layers. The first layer has the input neurons which send data via synapses to the second layer of neurons, and then via synapses to the third layer which contains the output neurons. More layers may be needed for more complex systems. The synapses store parameters called “weight” which manipulate the data in the calculations [106]. The ANN is defined by three parameters, which are the interconnection pattern between the different layers of

Figure 6.8: A schematic graph of the ANN.

neurons, the learning process of updating the weight of interconnections and the third is the activation function that converts the neurons weighted input to its output activation. It has three levels the input, the hidden and the output level. The solution of it is given as in the following equation

$$f_k(x_i) = K \left( \sum W_{jk} g_j(x_i) \right) \quad 6.1$$

where  $x_i$  is the inputs, the hidden contains the  $g_j(x_i)$ ,  $K$  is predefined function.  $W_{jk}$  is the weight function and issued from the algorithm which minimizes the distance between the interpolation and the known values (design points) [6].



### 6.1.3 Parameter Local and Global Sensitivity

Also the impact of the input parameters on the output parameters can be seen in the figure 6.9 below. The local sensitivity of each parameter is represented graphically. The sensitivity charts are single parameter sensitivities, which means that the DOE calculates the change of the output based on each input independently at the current value of each input parameter value.

The large the change of the output the more significant and effective the input parameter is, as we can see the sensitivity of the input pressure by the shaft power and the exit flow angle at the rotor trailing edge.

The figure 6.10 represents statistical sensitivity, which is a global sensitivity, as we can see in the GD Optimization. This sensitivity based on correlation analysis using generated sample points. It doesn't depend on the setting of the input parameters because all possible values for the input parameters are already taken into consideration in the sensitivity determination step.

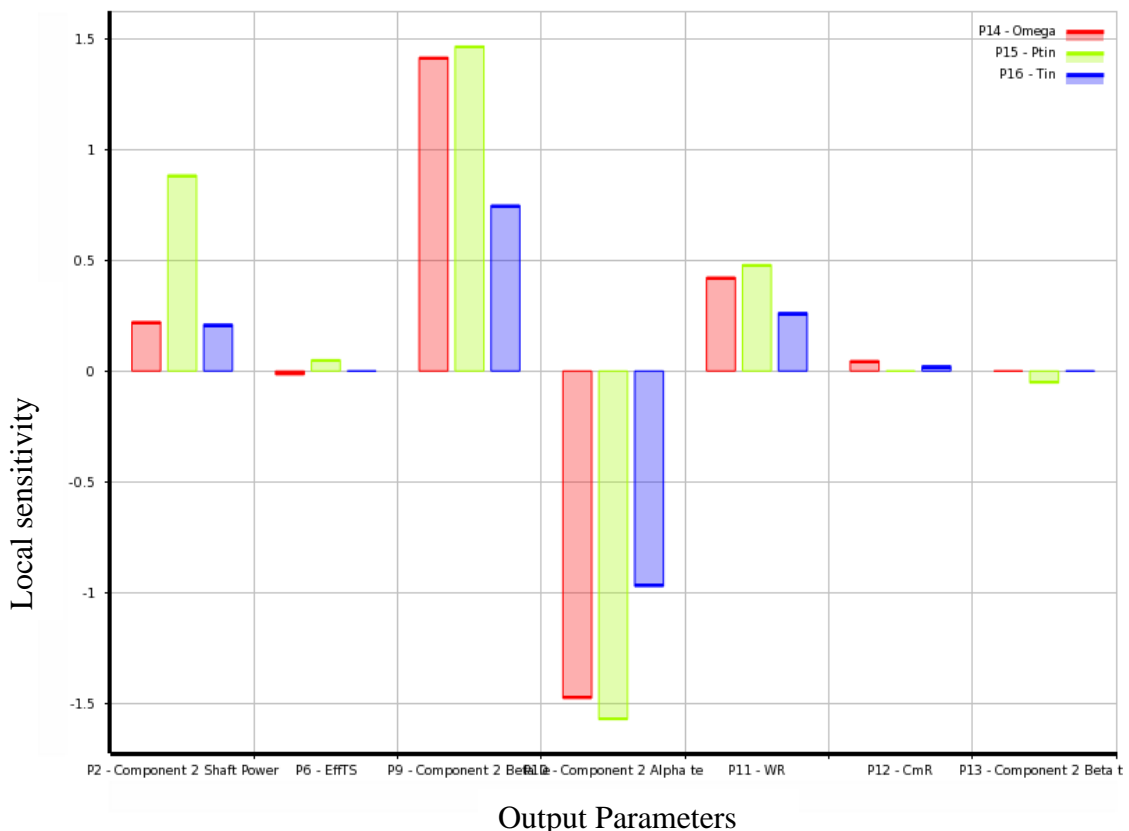
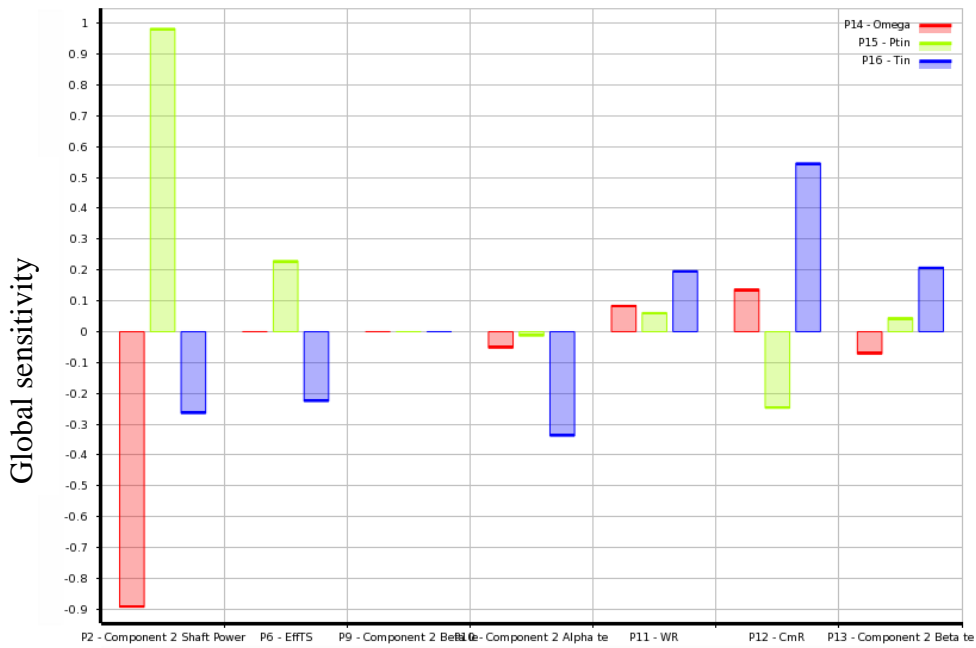


Figure 6.9: Local sensitivity of Parameters.



Output Parameters

Figure 6.10: Global sensitivity depending on output parameters

The candidate design points can be shown in the figure 6.11 below. A suggested combination of the parameters have been proposed and tradeoff can be made to select a new design point

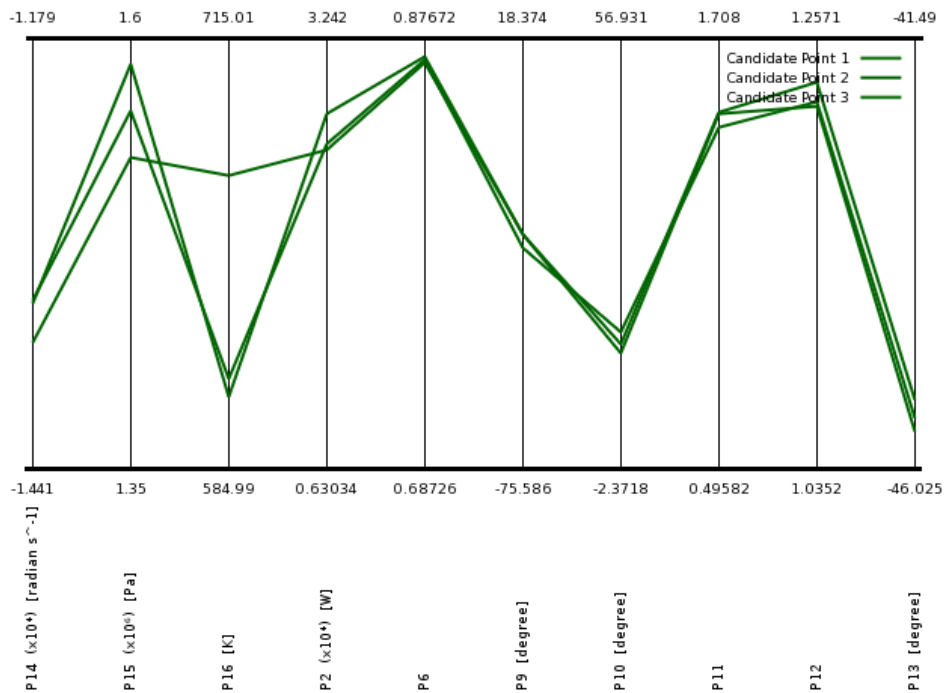


Figure 6.11: Cadidate design points

## 6.2 Genetic algorithm optimization

After performing the Multi-Objective Genetic Algorithm optimization which is a Non-dominated Sorted Genetic Algorithm-II, NSGA-II. We set our objectives, constraints, the output and input parameters. It is worth saying here that this method is limited to the continuous input parameters and it aims at finding a global optimization point.

It suggested a list of candidates and as follows:

*Table 6.3: List of candidate points*

Parameter	Candidate point 1	Candidate point 2	Candidate point 3	Candidate point 4	Candidate point 5
$\omega$ (radian s <sup>-1</sup> )	13300.86667	12895.23782	12916.6	12916.6	13241.43315
$P_{tin}$ (Pa)	1596927.083	1548098.958	1523496.881	1523496.881	1540286.458
$T_{in}$ (K)	593.4580247	589.8510232	609.2820406	609.2820406	650.5792537
Shaft Power (W)	26407.87864	25455.05132	24183.29074	24183.29074	25233.01448
$\eta_{t-s}$ [-]	0.872081718	0.873357663	0.867987306	0.867987306	0.864709672
Beta le (degree)	23.14573929	-24.62340086	-25.9521606	-25.9521606	-20.84372209
$\alpha_5$ (degree)	14.70271838	15.69298092	15.74800074	15.74800074	12.0239813
WR	1.519560602	1.499730466	1.477745631	1.477745631	1.537104898
CmR	1.246787815	1.232020532	1.223683355	1.223683355	1.2223689
$\beta_4$ (degree)	45.20801857	-45.53209879	-45.66009314	-45.66009314	-45.57593907

## 6.3 Optimization methods results

The candidate points of the optimization process have been applied as a boundary. The performance of the turbine has experienced additional improvements over the results of the parameter study and the preliminary design.

The recovered energy as a percentage of the output power of the automobile for the five candidate points are as follow

*Table 6.4: Percentage of the recovered energy.*

The candidate point number	1	2	3	4	5
Percentage of the recovered energy %	16.119	15.553	14.761	14.76	15.402

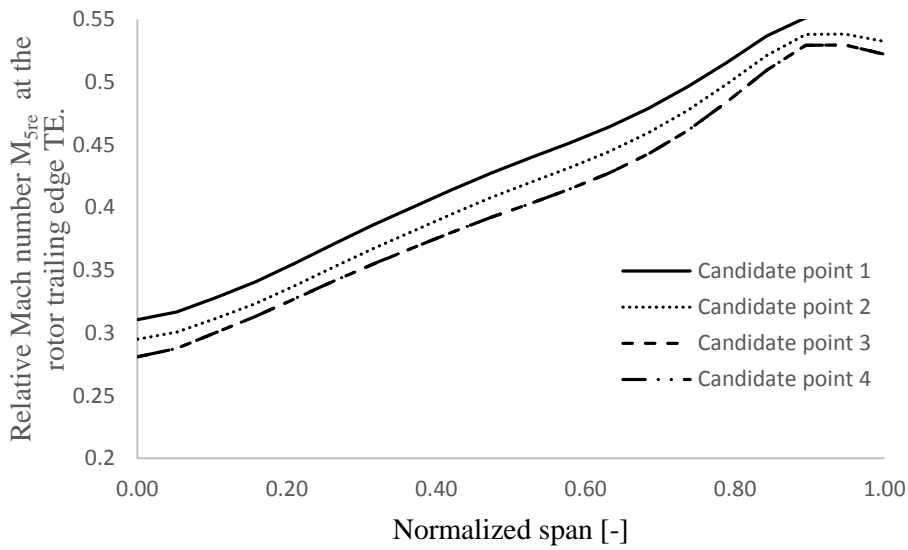


Figure 6.12: Relative Mach number  $M_{5re}$  at the rotor trailing edge TE versus the normalized span width for the optimization candidate points.

The figure 6.12 and the figure 6.13, represents the relative and the absolute Mach number at the trailing edge of the rotor blade. It is clear that the behavior of the Mach numbers are similar and the curves are almost concentrated.

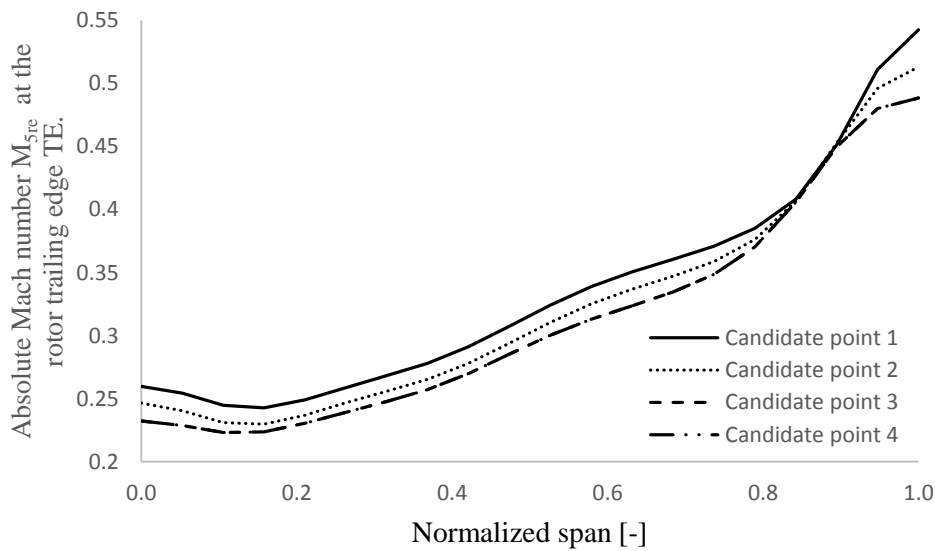


Figure 6.13: Absolute Mach number  $M_{5re}$  at the rotor trailing edge TE versus the normalized span width for the optimization candidate points.



## 7 Conclusions

The work of this thesis aims at presenting and optimized a compact design of a radial inflow turbine to be employed in the energy recovery applications of the automobiles and to operate efficiently with high rotational speed with different operating conditions. An appropriate working fluid has also been introduced.

However, around two-third the energy supplied to the ICEs is wasted and dumped to the environment. The exhaust gas and the cooling system through which this energy is wasted the most. Therefore, harnessing as much energy as possible and recovering it, is an inevitable duty for the designers and the academic researchers. An energy recovery closed cycle has been adopted, which allows the wasted energy to be transferred to its organic working fluid and eventually producing energy. In this study we introduced and successfully designed and optimized a radial inflow turbine for this recovery cycle. This radial turbine plays the main role in the energy recovery cycle and it is the most important and complex part in the design process. The miniature and the high speed effect of the turbine have been carefully studied. The Ethanol with chemical composition  $C_2H_5OH$  has been chosen to be the working fluid. As this working fluid has a relatively low boiling temperature, and as we expected, the fluid flow throughout the turbine is in the superheated region or even above the critical point. It is very important to have a super dry fluid in the turbine, to avoid some mechanical problems such as corrosion or even more turbulence level if we have liquid particles.

To have an accurate numerical simulation, a mesh-independent analysis has been performed to have a sufficiently refined grid in a way that more refinement in the mesh doesn't affect the simulation results. A finite volume FV model has been employed for the numerical simulation of the fluid flow through the radial inflow turbine. In this model we made use of the turbulence models mainly the *SST- $k-\omega$* . This turbulence model has been validated over many cases, and it is recommended as a good choice that offers a compromise between the calculation cost and the accuracy. We made also a comparison between the *SST- $k-\omega$*  and the standard  *$k-\epsilon$*  models and we found that the *SST- $k-\omega$*  gives better results, especially in the regions close to the walls. Choosing an appropriate turbulence model is of great importance, as a lot of transitions have to be investigated, such as wake/ jet effect, shock and flow separation.

The preliminary geometry of the turbine has been created using recommended values of dimensionless parameters, such as the specific speed, the specific diameter, Mach number, velocity ratio and other geometrical correlations. The geometry is further adjusted in the performance analysis and the optimization procedures. The performance of the turbine at the design point has been compared to the results of Vista RTD, as it is validated over many experimental results, and it shows a very good agreement. The performance of the turbine has been further analyzed for different boundary conditions, at the design point and at off-design points. That gave us an excellent insight about the

effect of miniature, the effect of high density working fluid and also the effect of high rotational speed on the turbine performance. The latter properties are the main requirements of our application.

An optimization procedures have been performed to find the optimum performance of the radial inflow turbine under various operating conditions, and also find the effect of each parameter on the design configuration. The Design Exploration tools has been used, employs various optimization algorithms and techniques. We used first the Design of Experiments method DOE, and used the Central Composite Design CCD type of DOE, to get the list of design points. The output parameters have been calculated depending on the design points produced previously, and then graphically represented. The response surface analysis has also been performed using artificial neural network ANN and also using the full 2<sup>nd</sup> Order polynomial. The Goal Driven Optimization GOD is then performed using the Multi-Objective Genetic Algorithm Method MOGA which aims at finding the global optimum. This optimization has constraints based on the parameter correlations given in previous works such as in ROHLIK [85] and BALJI [15]. A list of optimum design-points candidates are then evaluated. The performance of the turbine has then been checked for these optimum points, and improvement in the performance is obvious.

## 7.1 Outlook

This work has presented many observations and intensively investigated and optimized the design performance the proposed turbomachine. Some of these observations have been covered and some still need further investigations. Developing a turbulence model that deals with fluids above the critical points and fluids with high density is an important work to perform. Also the structural analysis and the effect of high speed on the life time of the turbine is a valuable work, addition to that, choosing an appropriate material that withstand all the mechanical and thermal stresses is a crucial topic that still needs to deal with. However, the bearings of the turbine need also to be tested, we suggest a magnetic bearings to be first chosen and further investigated.

A full cycle with thermodynamic and structural optimization and by applying different optimization methods to find the interaction between the various parameters can be also performed.





## 8 Appendix A

### 8.1 Minimum inlet Mach number

Optimizing the inlet flow to the rotor has been shown by WHITFIELD [104], and it is done by choosing the absolute and the relative flow angles that give the smallest inlet Mach number for a given power ratio. High inlet Mach number and possibility of choking are happened at improper flow angles. Following the development of Whitfield the tangential velocity is first written as follows:

$$C_{\theta 2} = U_2 + W_{\theta 2} = U_2 + C_{\theta 2} \frac{\tan \beta_2}{\tan \alpha_2} \quad (1)$$

In which the last term has been derived by sing

$$C_{\theta 2} = C_{m2} \tan \alpha_2 \quad W_{\theta 2} = W_{m2} \tan \beta_2 \quad (2)$$

Taking into consideration  $C_{m2} = W_{m2}$ . Multiplying through by  $C_{\theta 2}$  and rearranging gives

$$C_{\theta 2}^2 \left(1 - \frac{\tan \beta_2}{\tan \alpha_2}\right) = U_2 C_{\theta 2} \quad (3)$$

Following the Euler equation of turbomachinery, the right hand side is the work delivered, and since it is related to the power ratio, it will be taken to be fixed quantity. Dividing both by  $C_2^2$  leads to

$$\sin^2_{\alpha_2} \left(1 - \frac{\tan \beta_2}{\tan \alpha_2}\right) = y \quad (4)$$

In which

$$y = \frac{U_2 C_{\theta 2}}{C_2^2} = \frac{U_2 C_{\theta 2}}{C_{o2}^2} \frac{C_{o2}^2}{C_2^2} \quad (5)$$

Or

$$y = \frac{S_w}{(\gamma - 1) M_{o2}^2} = \frac{s}{m} \quad (6)$$

Where the following notation has been introduced:

$$s = \frac{S_w}{(\gamma - 1)} \quad m = M_{o2}^2 \quad (7)$$

The inlet stagnation Mach number has been defined as follows:

$$M_{o2}^2 = \frac{a_2}{\sqrt{\gamma R T_{o2}}} \quad (8)$$

Which can be also written as follows:

$$M_{o2}^2 = \frac{V_2^2}{a_{o2}^2} = \frac{V_2^2}{a_2^2} \frac{a_2^2}{a_{o2}^2} = M_{o2}^2 \frac{T_2}{T_{o2}} \quad (9)$$

So that

$$M_{o2}^2 = \frac{M_2^2}{1 + \frac{\gamma - 1}{2} M_2^2} \quad (10)$$

Dividing the equation (4) by  $\cos^2 \alpha_2$ , and noting that  $\frac{1}{\cos^2 \alpha_2} = \tan^2 \alpha_2 + 1$ , gives the following:

$$(1 - y) \tan^2 \alpha_2 - \tan \beta_2 \tan \alpha_2 - y = 0 \quad (11)$$

Or

$$(m - s) \tan^2 \alpha_2 - m \tan \beta_2 \tan \alpha_2 - u = 0 \quad (12)$$

For a given value of power ratio, Mach number and relative flow angle, this equation can be solved for  $\tan \alpha_2$ . The solution is found with the power ratio and the relative flow angle as parameters.

The minimum of each curve is sought for each the minimum of each value of  $S_w$ ,  $\beta_2$ .

To find it, let  $a = \tan \alpha_2$  and  $b = \tan \beta_2$ , and that puts the equation in the below form

$$(m - s)a^2 - mba - s = 0 \quad m = \frac{s(1 + a^2)}{a(a - b)} \quad (13)$$

And by setting the derivative of the above equation equal to zero, the minimum of m at fixed values of s and b can be obtained.

$$\frac{dm}{da} = \frac{2s(a - b)a^2 - s(2a - b)(1 + a^2)}{a^2(b - a)^2} \quad (14)$$

And this reduced to

$$ba^2 + 2a - b = 0 \quad (15)$$

Solving the quadratic equation gives

$$a = \frac{-1 \mp \sqrt{1 + b^2}}{b} \quad (16)$$

Substituting this value of a into equation (13) gives

$$m = \frac{2s}{1 \mp \sqrt{1 + b^2}} \quad (17)$$

For the minimum of m as a function of s and  $\beta_2$ . Since

$$\sqrt{1 + b^2} = \sqrt{1 + \tan^2 \beta_2} = \frac{1}{\cos \beta_2} \quad (18)$$

So the equation (16) becomes

$$\tan \alpha_2 = \frac{-\cos \beta_2 \mp 1}{\sin \beta_2} \quad (19)$$

Having the identity

$$\cos \beta_2 = \cos^2 \frac{\beta_2}{2} - \sin^2 \frac{\beta_2}{2} \quad (20)$$

$$\sin \beta_2 = 2 \sin \frac{\beta_2}{2} \cos \frac{\beta_2}{2} \quad (21)$$

The equation (19) leads to

$$\tan \alpha_2 = \frac{-\cos^2 \frac{\beta_2}{2} + \sin^2 \frac{\beta_2}{2} \mp 1}{2 \sin \frac{\beta_2}{2} \cos \frac{\beta_2}{2}} \quad (22)$$

The positive sign gives

$$\tan \alpha_2 = \tan \frac{\beta_2}{2} \quad (23)$$

It has been shown that the value of  $\alpha_2 > 0$  and  $\beta_2 < 0$ . The negative sign gives

$$\tan \alpha_2 = -\cot \frac{\beta_2}{2} \quad \text{or} \quad \tan \alpha_2 = \tan\left(\frac{\pi}{2} + \frac{\beta_2}{2}\right) \quad (24)$$

Hence

$$\alpha_2 = \frac{\pi}{2} + \frac{\beta_2}{2} \quad (25)$$

Substituting this into equation (17) when the value of m is minimum, this gives

$$m = \frac{2s \cos \beta_2}{\cos \beta_2 \mp 1} \quad (26)$$

The positive sign is chosen since the minus sign gives a negative m value, and this gives

$$M_{o2 \min}^2 = \frac{2s \cos \beta_2}{1 + \cos \beta_2} \quad (27)$$

As we've seen in the equation (10)

$$M_2^2 = \frac{M_{o2}^2}{1 - \frac{\gamma - 1}{2} M_{o2}^2} \quad (28)$$

By substituting the value of  $M_{o2 \min}^2$  from equation (27) into the above equation gives

$$M_2^2 = \left[ \left( \frac{2S_w}{\gamma - 1} \right) \frac{\cos \beta_2}{1 + (1 - S_w) \cos \beta_2} \right]^{1/2} \quad (29)$$

The minimum of the curve is seen from that the at nozzle angels in their usual range between  $60^\circ < \alpha_2 < 80^\circ$ . There may be two angles satisfy the equation (13). The smaller angle is to be chosen. The larger angles put the limit of how large the Mach number can be.

## 9 Bibliography

- [1] ALJANABY U. M., "Design and Optimization a Radial Inflow Turbine for Automobile Energy Recovery Usage.," *Report*, Bonn- Germany, 2011.
- [2] ANDERSON J. and et al., *Computational Fluid Dynamics, An Introduction*, Springer, 2009.
- [3] ANDERSON J., *Fundamental of Aerodynamics*, Fifth Edition, McGraw Hill, 2010.
- [4] ANSYS Inc., "ANSYS CFX-Solver Theory Guide," Canonsburg, PA, USA, 2013.
- [5] ANSYS, "ANSYS CFX-Solver Theory Guide," 2014: <http://www.ansys.com/>.
- [6] ANSYS, "Design Exploration User Guide," 2012.
- [7] AUNGIER R. H., "A Fast, Accurate Real Gas Equation of State for Fluid Dynamic Analysis Applications," *Trans. ASME Journal of Fluids Engineering*, pp. 277-281, 1995.
- [8] AUNGIER R. H., *Turbine Aerodynamics: Axial-Flow And Radial-Inflow Turbine Design And Analysis*, New York: ASME Press, 2006.
- [9] B. Turbosteamer.: <https://en.wikipedia.org/wiki/Turbosteamer>.
- [10] BAINES N. C. and A. WHITFIELD, *Design of Radial Turbomachines*, Essex, UK: Longman Scientific and Technical, 1990.
- [11] BAINES N. C. and H. Chen, "Performance parameters and assessment," *VKI, Radial Turbines*, 1992.
- [12] BAINES N. C., "A meanline prediction method for radial turbine efficiency.," in *International Turbocharging and Air Management Systems, IMECHE Conference Transactions*, 1998.

- [13] BAINES N. C., "Radial turbines: an integrated design approach," in *Concepts NREC*, North Chipping, UK.
- [14] BALDWIN B. S. and H. LOMAX, "Thin Layer Approximation and Algebraic Model for Separated Turbulent Flows," *AIAA*, 1978.
- [15] BALJE O. E., *Turbomachines: A Guide to Design, Selection and Theory*, New York: John Wiley & Sons Inc., 1981.
- [16] BENSON R. S. and et al., "An analysis of the losses in the rotor of a radial flow gas turbine at zero incidence," in *Proceedings of the Institution of Mechanical Engineers*, 1967.
- [17] BENSON R. S., "An analysis of the losses in a radial gas turbine," in *Proceedings of the Institution of Mechanical Engineers*, 1965.
- [18] BLAZEK J., *COMPUTATIONAL FLUID DYNAMICS: PRINCIPLES AND APPLICATIONS*, Oxford, UK: ELEVIER, 2001.
- [19] BONCINELLI P. and et al., "Real Gas Effects in Turbomachinery Flows: A Computational Fluid Dynamics Model for Fast Computations," *ASME J. Turbomachinery*, vol. 126, no. 2, pp. 268-276, 2004.
- [20] BOYS P. and MAHARWAN, *Gas Turbine Engineering*, 2002.
- [21] CHAKRAVARTHY S. R. and S. OSHER, "High resolution applications of the OSHER upwind scheme for the Euler equations," *AIAA*, San Diego, California, USA, 1983.
- [22] CHAPMAN D. R. and G. D. KUHN, "The limiting behaviour of turbulence near a wall," *Journal of Fluid Mechanics*, vol. 170, pp. 265-292, 1986.
- [23] CHEN H. and N. C. BAINES, "The aerodynamic loading of radial and mixed-flow turbines," *International Journal of Mechanical Sciences*, vol. 36, no. 1, pp. 63 - 79, 1994.
- [24] CHO S.-Y. and et al., "A study of the optimal operating conditions in the organic Rankine cycle using a turbo-expander for fluctuations of the available thermal energy," *Elsevier, Energy*, vol. 64, pp. 900-911, 2014.

- [25] CINNELLA P. and P. CONGEDO, "numerical solver for dense gas flows.," *AIAA*, pp. 1-12, 2004.
- [26] CORDIER O., "Similarity Consideration in Turbomachines," VDI, 1955.
- [27] CRANK J. and P. NICOLSON, "A practical method for numerical evaluation of solutions of partial differential equations of the heat conduction type," *Proc. Camb. Phil. Soc.*, pp. 50-67, 1947.
- [28] DAW C. S., R. L. GRAVES, R. M. WAGNER and J. A. CATON, "Report on the Transportation Combustion Engines Efficiency Colloquium Held at USCAR," U. S. Department of Energy, Tennessee, 2010.
- [29] DEAN EDWARDS K. and et al., "Defining Engine Efficiency," in *17 th. DEER Conference*, Detroit, MI, USA, 2011.
- [30] DEMIRDZIC I., Z. LILEK and M. PERIC, "A collocated finite volume method for predicting flows at all speeds," *International Journal of Numerical Methods in Fluids*, vol. 16, pp. 1029-1050, 1993.
- [31] DIXON S. L., *Fluid Mechanics and Thermodynamics of Turbomachinery*, Seventh edition, Butterworth Heinemann, 2013.
- [32] EARL LOGAN J., *Turbomachinery: Basic Theory and Application*, Second Edition, CRC Press, 1993.
- [33] FAVRE A., "Equations des Gaz Turbulents Compressibles, part 1: formes generales.," *Journal de Mecanique*, pp. 361-390., 1965.
- [34] FAVRE A., "Equations des gaz turbulents compressibles, part 2 methode des vitesses moyennes; methode des vitesses moyennes pondrees par la masse volumique.," *Journal de Mecanique.*, pp. 391-421., 1965.
- [35] FERZIGER J. H. and M. PERIC, *Computational Methods for Fluid Dynamics*, 2002.
- [36] FYFFE J., "The Reports of My Death Have Been Greatly Exaggerated," *An Internal Combustion Engine's Story, Stanford Energy Journal*, April 2014.



- [37] GASKELL P. H. and A. K. C. LAU, "Curvature-compensated convective transport: SMART, a new boundedness-preserving transport algorithm," *International Journal of Numerical Methods in Fluids*, vol. 8, no. 6, p. 617{641, 1988.
- [38] GERASIMOV A., "Modelling Turbulence Flows with Fluent," ANSYS Inc., 2006.
- [39] GEWALD D., Waste heat recovery of stationary internal combustion engines for power generation, PhD Dissertation, Munich, Germany: Technische Universität München, 2013.
- [40] GLEISER C. and RODGERS, "Performance of a high-efficiency radial/axial turbine," *ASME Journal of Turbomachinery*, pp. 151-154, 1987.
- [41] GLOSSMAN A. J., "Computer Program for Design and Analysis of Radial Inflow Turbine," NASA, Washington DC, USA, 1976.
- [42] GOPAL K., R. SUBBARAU and e. al., "Thermodynamic analysis of a diesel engine integrated with a PCM based energy storage system," *International Journal of Thermodynamics*, pp. 15-21, 13 January 2010.
- [43] Green Car Congress: <http://www.greencarcongress.com/2008/04/study-steam-hyb.html>.
- [44] HARTEN A., "High resolution schemes for hyperbolic conservation laws," *Journal of Computational Physics*, vol. 49, no. 3, p. 357{393, 1983.
- [45] HERBINE R. and et al., Finite Volume Methods, This manuscript is an update of the preprint n0 97-19 du LATP, UMR 6632, Marseille, September 1997 which appeared in Handbook of Numerical Analysis, P.G. Ciarlet, J.L. Lions eds, vol 7, pp 713-1020, 2003.
- [46] HIETT G. F. and I. H. JOHNSON, "Experiments Concerning the Aerodynamic Performance of Inward Flow Radial Turbines," in *Proceedings of the Institution of Mechanical Engineers IME*, 1963.
- [47] HOFFERN J., "Adaption of FINFLO for real gases.," Helsinki University of Technology, Laboratory of Applied Thermodynamics, Helsinki, Finland, 1997.

- [48] HORSTMAN J. R. and C. C. VIEGAS, "Comparision of Multiequation Turbulence Models for Several Shock Separated Boundary-Layer Interaction Flows.," *AIAA Journal*, 1979.
- [49] International Energy Agency, "Oil Information, [http://wds.iea.org/wds/pdf/documentation\\_oil\\_2010.pdf](http://wds.iea.org/wds/pdf/documentation_oil_2010.pdf)," Paris, 2010.
- [50] ISSA R. I., "Solution of implicity discritized fluid flow equations by operator-splitting," *Journal of Computational Physics*, vol. 62, pp. 40-65, 1986.
- [51] JADHAO J. S. and D. G. THOMBARE, "Review on Exhaust Gas Heat Recovery for I.C. Engine," *International Journal of Engineering and Innovative Technology (IJEIT)*, Volume 2, Issue 12, June 2013.
- [52] JAMIESON A. H., *Gas Turbine Principle and Practice*, London: George Newnes, 1955.
- [53] JINYUAN T. and et al., *Computational Fluid Dynamics: A Practical Approach.*, Butterworth-Heinemann., 2007.
- [54] JIYAN P. and et al, *Computational Fluid Dynamics, A practical approach*, Oxford, UK: Elsevier Inc., 2008.
- [55] JOHNSON W. and RICHARD, *Handbook of Fluid Dynamics*, Crc Pr Inc, 1998.
- [56] KNIGHT D. D., "Nunmerical Simulation of compressible Turbulent Flows Using the Reynolds-averaged Navier-Stocks Equation: Turbulence in compressible Fluids.," AGARD Report, 1997.
- [57] KORPELA A. and SEPO, *Principles of Turbomachinerry*, New Jersy, US: John Wiley & Sons, Inc., 2011.
- [58] KRÄHENÜHL D., C. ZWYSSIG, H. WESSER and J. W. KOLAR, "Theoretical and experimental results of a mesoscale electronic power generation system from pressurized gas flow," *Journal of Micromechanics and Microengineering*, 16 August 2009.
- [59] LAW C., "Supersonic Turbulent Boundary-Layer Separation," *AIAA Journal*, 1974.

- [60] LEONARD B. P., "The numerical computation of turbulent," *Computer Methods in applied mechanics and engineering*, vol. 3, p. 269{289, 1974.
- [61] LILEK Z. and et al., "An implicit finite-volume method using nonmatching blocks of structured grid," *Numerical Heat Transfer*, vol. 32, pp. 385-401, 1997.
- [62] LINHARD H. D., "Crayogenic Turboexpanders," *LNG/ Cryogenics*, pp. 7-15, 1973.
- [63] MAGNOLI M. V., *Numerical simulation of pressure oscillations in large Francis turbines at partial and full load operating conditions and their effect on the runner structural behaviour and fatigue life*, PhD thesis, Technical University of Munich, 2014.
- [64] MAJUMDAR S., "Role of Underrelaxation in Momentum Interpolation for calculation of Flow with Nonstaggered Grid," *Numerical Heat Transfer*, pp. 125-132, 1988.
- [65] MALALASEKERA W. and H. K. VERSTEAG, *An Introduction to Computational Fluid Dynamics, The Finite Volume Method*, second edition, 2007.
- [66] MENTER F. R., "Two-Equation Eddy-Viscosity Turbulence Models for Engineering Applications," *AIAA Journal*, vol. 32, no. 8, pp. 1598-1605, 1994.
- [67] MENTER F. R., "Zonal Two-Equation  $k-\omega$  Turbulence Models for Aerodynamic Flows," *AIAA Journal*, 1993.
- [68] MORKOVIN M. V., "Effects of Compressibility on Turbulent Flow.," *The Mechanics of turbulence*, Favre, A. (ed.), Gordon & Breach, New York,, pp. 367-380, 1964.
- [69] MOUSTAPHY H. and et al., *Axial and Radial Turbines*, Concepts ETI, Inc., 2003.
- [70] NELSON L. C. and E. F. ROBERT, "Generalized pvT Properties of Gases," *Trans. ASME*, pp. 1057-1066, 1954.

- [71] PASQUALE D. and et al., "Shape Optimizazion of an Organic Rankin Cycle radial Turbine Nozzle," *ASME J Eng Gas Turbine Power*, 2013.
- [72] PATAKAR S. V., Numerical Heat Transfer and Fluid Flow, Hemisphere Publishing Corp., 1980.
- [73] PCA Engineers Limited: <http://www.pcaeng.co.uk/>.
- [74] PENG H., LIUS and X. ZHANG, "Review of transportation and energy consumption related research," *Journal of Transportation Systems Engineering and Information Technology*, pp. 6-16, 2009.
- [75] PILTZER K. S. and et al., "The Volumetric and Thermodynamic Properties of Fluid. II. Compressibility Factor , Vapor Pressure and Entropy of Vaporization," *American Chemical Socitey*, pp. 3427-3440, 1955.
- [76] PIOMELLI U., "Large-Eddy Simulation: Present State and Future Perspectives.," *AIAA*, 1998.
- [77] REDA D. and J. MURPHY, "ShockWave Turbulent Boundary Layer Interactions in Rectangular," *AIAA Journal*, 1973.
- [78] REDLICH O. and J. KWONG, "On The Thermodynamics Solutution. V. an Equation of State Fugacities of Gaseous Solution," *Chemical Review*, pp. 233-244, 1949.
- [79] REGAL A., "Numerical analysis of three-time-level finite difference schemes for unsteady diffusion–convection problems," *International Journal for Numerical Methods in Engineering*, vol. 30, no. 2, pp. 307-330, 1990.
- [80] REYNOLDS O., "On the Dynamical Theory of Incompressible Viscous Fluids and the Determnation of the Criterion.," *Philosophical Transactions of the Royal Society of London*, 186 (1895), 123..
- [81] RHIE C. M. and W. L. CHOW, "A Numerical Study of the Turbulent Flow Past an Isolated Airofoil with Trailing Edge Separation," *AIAA*, 1982.
- [82] RIBAUD Y. and C. MICHEL, "Study and Experiments of a Small Radial Turbine for Auxiliary Power Units," in *ASME 1986 International Gas Turbine Conference and Exhibit*, Dusseldorf, West Germany, 1986.

- [83] RIEDEL N., *Rotor-Stator Wechselwirkung in hydraulischen Maschinen. PhD thesis, Technische Universität München, Lehrstuhl für Hydraulische Maschinen und Anlagen, 1997.*
- [84] RODGERS C., "Meanline Performance Prediction for Radial Inflow Turbines.," Kaman Institute, Rhode-St-Genève, Brussels, Belgium, 1987.
- [85] ROHLIK H., "Analytical determination of radial inflow turbine design geometry for maximum efficiency," NASA Lewis Research Center, Cleveland, OH, United States, 1968.
- [86] ROHLIK H., "Radial-inflow turbines, in Turbine Design and Applications," A. J. Glassman, ed., SP290, NASA, 1975.
- [87] SAIDUR R. A., "review on electrical motors energy use and energy savings," *Renewable and Sustainable Energy Reviews*, 2010.
- [88] SALIM S. M. and et al., "Y Plus Approach for Dealing with Turbulent Flow over a Surface Mounted Cube: Part 1 Low Reynolds Number," in *Seventh International Conference on CFD in the Minerals and Process Industries*, Melbourne, Australia, 2009.
- [89] SAMIP S. and et al., "Effect of Flow Coefficient and Loading Coefficient on the Radial Inflow Turbine Impeller Geometry," *International Journal of Research in Engineering and Technology*, vol. 2, no. 2, pp. 98-104, 2013.
- [90] SAURET E. and G. YUANTONG, "Three-dimensional off-design numerical analysis of an organic Rankine Cycle Radial-Inflow Turbine," *Elsevier, Applied Energy*, vol. 135, pp. 202-211, 2013.
- [91] SCHLICHTING H. T., *Boundary-Layer Theory*, Berlin: Springer, 2000.
- [92] SCHMITT F. G., "About Boussinesq's turbulent viscosity hypothesis: historical remarks and a direct evaluation of its validity," *Comptes Rendus Mécanique, Elsevier*, pp. 617-627, 2007.
- [93] SIMPSON A. T., S. W. T. SPENCE and J. K. WATTERSON, "Numerical and Experimental Study of the Performance Effects of Varying Vaneless Space and Vane Solidity in Radial Turbine Stators," *ASME Journal of Turbomachinery*, vol. 135, no. 3, 2013.

- [94] SKODA R., *Numerische Simulation abgeloester und transitionaler Stroemungen in Turbomaschinen, PhD thesis, Technische Universitaet Muenchen, Lehrstuhl fuer Hydraulische Maschinen und Anlagen, Muenchen, 2003.*
- [95] SMITH A. M. O. and T. CEBECI, "Numerical solution of the turbulent boundary layer equations," Douglas aircraft division report, 1967.
- [96] SOAVE G., "Equilibrium Constants from a Modified Redlich-Kwong Equation of State," *Chemical Engineering Science*, pp. 1197-1203, 1972.
- [97] SPALDING D. A., "A Novel Finite-difference Formulation for Differential Expressions Involving both First and Second Derivatives," *Int. J. Numer. Methods Engineering*, vol. 4, 1972.
- [98] TAN P.: <http://paultan.org/2005/12/11/bmw-turbosteamer/>.
- [99] TSUEI H.-H. and et al., "Advanced Turbulence Model for Transitional and Rotational Flows in Turbomachinery," *AIAA*, 2000.
- [100] TUNAKOV A. P., "Effect of Radial Clearance on the Operation of a Centripetal Gas Turbine," *Zavedeniy Aviatsionnaya Technika*, pp. 83-92, 1960.
- [101] VAN DOORMAL J. P. and G. D. RAITHBY, "Enhancement of SIMPLE method for predicting incompressible fluid flows," *Numerical Heat Transfer*, vol. 7, pp. 147-163, 1984.
- [102] VIESER W., T. ESCH and MENTER, "Heat transfer prediction using advanced two- equations turbulence models, Tech. Rep. CFX Technical Memorandum CFX- VAL 1/ 0602," ANSYS, Inc., 2002.
- [103] WATANABE and et al., "Effect of Dimensional Parameters of Impellers on Performance Characteristics of Radial Inflow Turbine," *trans. ASME Journal of Engineering for Power*, pp. 81-102, 1971.
- [104] WHITFIELD A., "The preliminary design of radial inflow turbines," *Journal of Turbomachinery*, 1990.
- [105] Wikipedia: [https://en.wikipedia.org/wiki/Artificial\\_neural\\_network](https://en.wikipedia.org/wiki/Artificial_neural_network).

- [106] WILCOX D. C., *Turbulence Modeling for Cfd*, 3rd ed., David C. Wilcox: DCW Industries, Inc., 2006.
- [107] WILSON D. G., *The design and performance analysis of radial inflow turbines*, 1964.
- [108] WILSON G. M., "Calcuaion of Enthalpy Data from Moified Redlich-Kwong Equation of State," *Adanced Cryogenic Engineering*, 1966.
- [109] WISLICENSUS G. F., *Fluid Mechanics of Turbomachinery*, Dover Publications, 1965.
- [110] WOOD H. J., "Current Technology of Radial-Inflow-Turbines for compresible fluids," *Trans. ASME, Journal of Engineering for power*, pp. 72-83, 1963.
- [111] WRIGHT T., *Fluid Machinery: Performance, Analysis and Design*, CRC Press, 1999.
- [112] YOUNG A. D. YOUNG, *Boundary Layers*, Oxford, UK: Blackwell Scientific Publication Ltd, 1989..